# ADVANCED SINGLE-CHIP TEMPERATURE STABILIZATION SYSTEM FOR SILICON MEMS RESONATORS AND GYROSCOPES

A Dissertation
Presented to
The Academic Faculty

by

Chang-Shun Liu

In Partial Fulfillment
of the Requirements for the Degree
Doctor of Philosophy in the
School of Electrical and Computer Engineering

Georgia Institute of Technology

May 2019

Copyright © 2019 by Chang-Shun Liu

# ADVANCED SINGLE-CHIP TEMPERATURE STABILIZATION SYSTEM FOR SILICON MEMS RESONATORS AND GYROSCOPES

Approved by:


Prof. Farrokh Ayazi, Advisor
School of Electrical and Computer Engineering
*Georgia Institute of Technology*

Prof. Arijit Raychowdhury
School of Electrical and Computer Engineering
*Georgia Institute of Technology*

Prof. Hua Wang
School of Electrical and Computer Engineering
*Georgia Institute of Technology*

Prof. John D. Cressler
School of Electrical and Computer Engineering
*Georgia Institute of Technology*

Prof. Peter J. Hesketh
School of Mechanical Engineering
*Georgia Institute of Technology*


Date Approved: March 25, 2019

*To my loving family*

# ACKNOWLEDGEMENTS

First, I would like to express my sincere gratitude to my advisor and mentor, Professor Farrokh Ayazi for his insightful guidance, support, and encouragement, for believing in my ability to succeed and for guiding me towards success.

I would like to thank my proposal exam committee member, Professor Maysam Ghovanloo and my dissertation committee members, Professor Arijit Raychowdhury, Professor Hua Wang, Professor John D. Cressler and Professor Peter J. Hesketh for their interest in my research and for spending their precious time reviewing this dissertation and providing valuable feedback.

It has been a great pleasure and honor to work with and become friends with many former and current members of the IMEMS group. I would like to thank Dr. Mauricio Pardo Gonzalez, Dr. Milap Dalal, Dr. Wang-Kyung Sung, Dr. Diego Serrano, Dr. Logan Sorenson, Dr. Peng Shao, Dr. Chong Li, Dr. Vahid Tavassoli, Dr. Giorgio Casinovi, and Dr. Benoit Hamelin for all the invaluable discussions and suggestions. I thank Anosh Daruwalla, Ryan Lei, Sam Wisher, Jaehoo Choi, Pranav Gupta, Seung-Yong Shin, Jeremy Yang, Minxiang Gong and Hua Chen for their collaborative help. I give my special thanks to Dr. Arashk Shirazi and Dr. Yaesuk Jeong for their tremendous help on circuit design. Also, special thanks go to Dr. Roozbeh Tabrizian, Dr. Jenna Fu, Anosh Daruwalla, and Dr. Haoran Wen for providing me with awesome devices and insightful discussion. In addition, I have appreciated all the helps provided by Albert Lu and other friends at the Georgia Institute of Technology, which made this work possible.

I want to express my deepest gratitude to my parents, for their unconditional love and support, which has given me the courage and confidence to chase my dreams.

# TABLE OF CONTENTS

ACKNOWLEDGEMENTS ........ iv

LIST OF TABLES ........ viii

LIST OF FIGURES ........ ix

SUMMARY ........ xvii

CHAPTER 1: INTRODUCTION ........ 1

1.1 A Brief History of Timing References – From Quartz to MEMS ........ 1

1.2 Performance Requirements and Specifications ........ 5

1.3 Origin of the Problem – Temperature-Induced Frequency Drift ........ 6

1.4 Motivation ........ 10

CHAPTER 2: MEMS RESONATOR AND OSCILLATOR BASICS ........ 11

2.1 MEMS Resonator Basics ........ 10

2.2 MEMS Oscillator Basics ........ 16

2.2.1 Transimpedance Amplifier (TIA) ........ 19

2.2.2 Variable Gain Amplifier (VGA) ........ 24

2.2.3 Amplitude Detector ........ 28

2.2.4 Phase Shifter ........ 29

CHAPTER 3: A MEMS OCXO USING STRUCTURAL RESISTANCE-BASED TEMPERATURE SENSING ........ 32

3.1 Silicon MEMS OCXO System ........ 33

3.2 Silicon MEMS Resonator Design ........ 34

3.3 Oscillator Circuit Design ..... 38
3.4 Measurement Results ..... 44
3.5 Conclusion and Discussion ..... 50
CHAPTER 4: MEMS CORIOLIS RESONANT GYROSCOPES ..... 52
4.1 MEMS Coriolis Vibratory Gyroscopes (CVG) ..... 52
4.1.1 Principle of Operation ..... 53
4.1.2 Mode-Matching in MEMS Coriolis Gyroscopes ..... 55
4.2 Gyroscope Performance Specifications ..... 57
4.2.1 Scale Factor ..... 57
4.2.2 Bandwidth ..... 58
4.2.3 Resolution ..... 59
4.2.4 Zero-Rate Output and Bias Drift ..... 60
4.2.5 Allan Variance ..... 60
4.2.6 Determining Minimum Detectable Rotation Rate ..... 64
4.2.7 Scale Factor Instability and Drift Mechanisms ..... 66
CHAPTER 5: INTERFACE SYSTEM FOR OVENIZED MEMS GYROSCOPES ..... 67
5.1 The Single Chip Silicon MEMS TIMU ..... 67
5.1.1 Three-Axis Gyroscopes ..... 68
5.1.2 Three-Axis Accelerometers ..... 68
5.1.3 Timing Resonator ..... 69
5.2 Interface Circuits for the 6-DoF MEMS IMU ..... 69
5.2.1 Transimpedance Amplifier (TIA) Design ..... 70
5.2.2 Feedthrough Cancellation ..... 75

5.2.3 Drive Loop ..... 79

5.2.4 Sense Channel and Demodulator ..... 80

5.2.5 Oven Control Loop ..... 81

5.2.6 PCB Layout Floor Plan ..... 83

5.3 Gyroscopes Measurement Result ..... 85

5.3.1 Scale Factor and Allan Deviation ..... 85

5.3.2 Cross-Axis Sensitivity ..... 87

5.3.3 Ovenization on Gyroscopes ..... 89

5.3.4 The TCR Measurement ..... 94

CHAPTER 6: AC HEATING SCHEME FOR LOWER POWER $R_{Struc}$-BASED TEMPERATURE SENSING MEMS OCXO ..... 96

6.1 The Power Consumption of MEMS OCXO ..... 96

6.2 AC Heating Scheme ..... 97

CHAPTER 7: CONCLUSION AND FUTURE WORK ..... 103

7.1 Contributions ..... 103

7.2 Future Work ..... 105

APPENDIX A ..... 110

APPENDIX B ..... 112

APPENDIX C ..... 116

REFERENCES ..... 118

# LIST OF TABLES

Table 1-1: Frequency reference temperature stability for different applications [6] .......... 5

Table 1-2: Quartz OCXOs commercial products with single-digit ppb frequency stability ........................................................................................................... 6

Table 2-1: RLC parameters for the equivalent model of electrostatic MEMS resonator... 15

Table 2-2: The performance parameters of the common gate TIA .................................. 21

Table 2-3: The performance parameters of the resistive feedback TIA ........................... 22

Table 2-4: The performance parameters of the capacitive feedback TIA [18] .................. 24

Table 3-1: MEMS OCXO Performance Summary and Comparison ............................... 51

Table 4-1: Performance grades of gyroscopes [33] .......................................................... 53

Table 5-1: Comparison of the Single-Stage and Two-Stage TIAs .................................. 73

Table 5-2: Performance Summary of All 3 Axes Gyroscopes ......................................... 87

Table 5-3: Measured Cross-Axis Sensitivity of All Three Axes Gyroscopes .................. 89

# LIST OF FIGURES

Figure 1.1: Temperature characteristics of extensional mode resonators aligned in the different crystallographic direction of silicon and for different doping concentrations [9] ........ 8

Figure 1.2: (left) Geometry-engineered concave SiBAR (CBAR) (right) device shows a TCF of -6 ppm/°C at 105MHz with a *Q* of 100 [13] ........ 9

Figure 1.3: Silicon piezoelectric resonators with (a) surface oxide compensation, (b) bulk oxide compensation, and (c) measured temperature characteristic of three different resonance modes [14] ........ 10

Figure 2.1: A MEMS clamped-clamped silicon beam resonator with symmetric capacitive transducers ........ 12

Figure 2.2: Summary of the beam resonator transfer function ........ 14

Figure 2.3: Equivalent RLC model of electrostatic (capacitive) and piezoelectric MEMS resonators ........ 15

Figure 2.4: Illustration of Barkhausen Criterion for oscillation ........ 17

Figure 2.5: General implementation for an electrostatic MEMS oscillator ........ 18

Figure 2.6: (a) The basic common gate TIA, and (b) the common gate TIA with gm boosting ........ 20

Figure 2.7: The resistive feedback TIA topology ........ 21

Figure 2.8: The capacitive feedback TIA topology [18] ........ 23

Figure 2.9: Three examples of variable-resistor based VGAs ........ 25

Figure 2.10: (a) The pseudo exponential gain control VGA [19], and (b) the gain tuning curve ..... 26

Figure 2.11: Gilbert cell based variable gain amplifier ..... 27

Figure 2.12: The 2GHz bandwidth, folded Gilbert cell VGA in [20] ..... 27

Figure 2.13: (a) Typical diode-based amplitude detectors; (b) The input and output waveform of a diode-based amplitude detector ..... 28

Figure 2.14: (a) Typical passive phase shifter and its transfer function; (b) The simulated gain and phase frequency response. The phase shift at the frequency $\omega = 1/(RC)$ equals to -90° ..... 30

Figure 2.15: (Left) Type-1 active phase shifter, and (right) Type-2 active phase shifter... 31

Figure 3.1: System block diagram of the silicon MEMS OCXO (left); and determination of the ovenset point by the TCR intersection of $R_{REF}$ and $R_{Struc}$ (right) ..... 33

Figure 3.2: (a) Cross-sectional Lamé-mode resonator geometry and mode shape, (b) layout of the 4mm$^2$ MEMS die, and (c) detail dimensions of the resonator ..... 35

Figure 3.3: (a) SEM images, (b) optical image of a wafer-level packaged cross-sectional Lamé resonator fabricated by Qualtré Inc. (now Panasonic), and (c) cross-sectional view of the resonator along the red line in (a) and the SEM of the HARPSS nanogap ..... 36

Figure 3.4: (a) Measured S21 of the cross-sectional Lamé-mode resonator, (b) measured temperature characteristic of the resonant frequency, and (c) measured temperature characteristic of the resonator structural resistance ..... 37

Figure 3.5: (a) Sustaining amplifier and the high-frequency CFT cancellation circuit, (b) detailed TIA schematic ..... 39

Figure 3.6: Schematic of the active oven control loop. The simplified oscillator circuitry is shown in gray color ........ 40

Figure 3.7: (a) Closed-loop model of the oven control circuit. (b) Gain and phase frequency response of the control system. The control system achieves a unity-gain crossover frequency of about 20 Hz ........ 42

Figure 3.8: Operating principle of the feedforward calibration ........ 43

Figure 3.9: (Left) Oscillator output spectrum and transient waveform; (right) Photographs of the prototype PCB and the ASIC die ........ 45

Figure 3.10: (a) MEMS OCXO steady-state frequency stability with and without digital calibration, and (b) MEMS OCXO frequency stability under varying temperature with the digital calibration enabled ........ 46

Figure 3.11: Measured MEMS OCXO phase noise with oven control loop enabled at the ambient temperatures of −25°C, 30°C, and 85°C. The oscillation frequency is 77.7 MHz ........ 47

Figure 3.12: Measured Allan deviation of the MEMS OCXO with both oven-control loop and digital calibration enabled. The measurement time is about 140 h at 60°C. The sampling period ($\tau_0$) is about 0.4s. The minimum Allan deviation is 7.5 ppb between 100 and 1000s ........ 48

Figure 4.1: (a) Coriolis effect in a tuning fork, (b) Tuning-fork gyroscope (TFG) operating based on the Coriolis effect [35] ........ 53

Figure 4.2: (a) At mode-matched condition, gyroscope gain is directly proportional to sense-mode quality factor, and (b) at mode-split condition, gyroscope gain is inversely proportional to frequency split [39] ........ 56

Figure 4.3: Typical Allan variance plot showing different regions corresponding to different sources of noise and drift [39] ........................................................................ 60

Figure 4.4: The Allan variance plot of a MEMS gyroscope with different noise or environment error sources considered. Allan variance for an ideal gyroscope is dominated by ARW region only. Only flicker can affect the ARW-only trend of the Allan variance plot while the temperature effects are sufficiently compensated [39] ............................. 64

Figure 5.1: Image of the wafer-level-packaged TIMU and SEM images of the uncapped TIMU die ........................................................................................................... 67

Figure 5.2: The block diagram of the complete gyroscope interface circuits. Here we take the z gyroscope as an example ........................................................................ 69

Figure 5.3: (a) The conventional single-stage resistive feedback TIA, and (b) the proposed two-stage low-pass, high-pass TIA (LP-HP TIA) .......................................................... 70

Figure 5.4: The measured gain and bandwidth of the two types of TIAs. For the single-stage TIA, $R_F$ = 100KΩ, CF = 0. For the two-stage LP-HP TIA, $R_{F1}$ = 5MΩ, $C_{F1}$ = 1pF, $R_{IN2}$ = 25KΩ, $C_{IN2}$ = 100pF, $R_{F2}$ = 4KΩ, $C_{F2}$ = 2.5pF. ($C_P$ = 2pF at both cases) ............ 73

Figure 5.5: The Cadence noise simulation of the two types of TIAs. For the single-stage TIA, $R_F$ = 100KΩ, $C_F$ = 0. For the two-stage LP-HP TIA, $R_{F1}$ = 5MΩ, $C_{F1}$ = 1pF, $R_{IN2}$ = 25KΩ, $C_{IN2}$ = 100pF, $R_{F2}$ = 4KΩ, $C_{F2}$ = 2.5pF. ($C_P$ = 2pF at both cases) ....................... 73

Figure 5.6: (a) The typical structure of a resonator, (b) the cross-sectional view (A↔B) of the left-hand side resonator, and (c) an example of the capacitive coupling through the device layer ........................................................................................................... 74

Figure 5.7: (a) Typical resonator model with the parasitic feedthrough capacitance ($C_{FT}$), and (b) $C_{FT}$ creates an anti-resonance in the magnitude response of the resonator. At the

anti-resonance frequency, the phase response of the resonator rolls back up; a very large CFT can roll the phase back up before the zero-crossing, and thus prevent the phase from crossing zero ........ 75

Figure 5.8: Operating principle of the feedthrough cancellation circuit used in this work ........ 76

Figure 5.9: (a) Include the phase shift (φ) effect of the feedthrough cancellation amplifier into consideration, (b) simulated feedthrough cancellation effectiveness with different phase shift φ ........ 77

Figure 5.10: (a) The complete drive loop circuits; (b) The detailed schematic of the phase shifters used for z and x/y gyroscopes ........ 78

Figure 5.11: The complete schematic of the 3rd-order low-pass filter for the analog demodulator output. It consists of a passive 1st-order LPF and a 2nd-order Sallen-Key filter. The -3dB bandwidth is 100Hz ........ 80

Figure 5.12: (a) The schematic of the oven control loop; (b) The proposed low-noise low-drift inverting (left) and non-inverting (right) heater amplifiers using ADA4522 ........ 81

Figure 5.13: The layout floor plan of the 6-DoF TIMU prototype board. (Dimension = 3.5-inch x 3.5-inch) ........ 82

Figure 5.14: (a) The photograph of the prototype TIMU board, and (b) the zoomed in view for the interposer board and the TIMU die ........ 83

Figure 5.15: Transient waveform of the simultaneous operation of all 3-axis gyroscopes (rotated by hands) ........ 84

Figure 5.16: Measured Allan deviation of x-axis gyroscope without ovenization ........ 85

Figure 5.17: Measured Allan deviation of y-axis gyroscope without ovenization ........ 85

Figure 5.18: Measured Allan deviation of z-axis gyroscope without ovenization ........... 86

Figure 5.19: An example of cross-axis sensitivity measurement. The applied sinusoidal (2Hz) rotation has a rate amplitude of 40°/s. (a) The recorded gyro demodulator output in time domain. The cross-axis rotation signal cannot be visually inspected. (b) By doing an FFT analysis to the waveform in (a), the cross-axis rotation signal can be extracted ...... 87

Figure 5.20: The ovenized frequency stabilities of the timing resonator, y-axis gyro and z-axis gyro ........................................................................................................ 88

Figure 5.21: (Left) The scale factor variation of the y-axis gyroscope with and without ovenization, and (right) the zoomed-in view of the scale factor variation with ovenization ........................................................................................................ 89

Figure 5.22: (Left) The bias variation of the y-axis gyroscope with and without ovenization, and (right) the zoomed-in view of the bias variation with ovenization ............................ 90

Figure 5.23: The ADEV of the y-axis gyroscope with and without ovenization (12 hours, $\tau_0$ = 0.018 sec). Without ovenization (room temperature), the bias instability is 114°/hour. With ovenization, the bias instability is 140°/hour ........................................................ 90

Figure 5.24: (Left) The scale factor variation of the z-axis gyroscope with and without ovenization, and (right) the zoomed-in view of the scale factor variation with ovenization ........................................................................................................ 91

Figure 5.25: The measure z-axis gyro quality factor (Q) variation v.s. ambient temperature ........................................................................................................ 91

Figure 5.26: (Left) The bias variation of the z-axis gyroscope with and without ovenization, and (right) the zoomed-in view of the bias variation with ovenization ........................... 92

Figure 5.27: The ADEV of the z-axis gyroscope with and without ovenization (2 hours, $\tau_0$ = 0.018 sec). Without ovenization, the bias instability is 9°/hour. With ovenization, the bias instability is 12°/hour ........ 93

Figure 5.28: The measured TCR of the RStruc on this TIMU die. The TCR shows a turnover point at around 35°C ........ 94

Figure 6.1: (a) The thermal simulation (Comsol) of the MEMS device used in chapter 3 with resonator heated up to 80°C. (b) The illustration of the main heat transfer path and the main heat dissipation path ........ 97

Figure 6.2 (a) Merge the heater with the resonator (and the Rstruc temperature sensor). (b) The SEM of a MEMS device fabricated in Georgia Tech, which shows a heating efficiency of 2mW/°C with separated heater, and a heating efficiency of 1.1mW/°C with merged heaters. The MEMS device was fabricated by Anosh Daruwalla ........ 98

Figure 6.3 Illustration of how the heater resistance mismatch can degrade the temperature sensor accuracy (only show one branch of the heaters for simplicity) ........ 99

Figure 6.4 The heater resistance mismatch is modulated to higher frequency by using AC heating voltages/currents. The modulated mismatch error can be low-pass filtered easily. (only show one branch of the heaters for simplicity) ........ 100

Figure 6.5 The complete implementation of the AC heating oven control loop. The orange blocks convert the RTD output voltage into a sinusoidal wave with a rms amplitude equal to $V_{RTD}$ ........ 101

Figure 6.6 Measured resonance frequency stability (S21) of the ovenized resonator with the proposed AC heating scheme. The result shows a total frequency variation of 45ppm from 0°C to 70°C ........ 101

Figure 6.7 The parasitic $R_{via}$ between the joint of $R_{Struc}$ and $R_{heat}$, and the RTD input is one major cause of the larger (45ppm) frequency variation ……………………………….. 102

Figure 7.1 The suggested TIMU daughter board implementation, which includes a micro-controller, high-resolution digital-to-analog converters (DAC), and high-voltage buffers for all the gyro tuning voltages. The DC-DC converters and linear regulators should also be included for the supply voltages ........................................................................ 109

Figure A.1 The oscillator frequency deviation due to unwanted sustaining amplifier phase shift. Two resonant peaks with quality factors of 2,500 and 7,500 are depicted here ..... 102

Figure B.1 The example of a 100MHz MEMS oscillator ............................................ 104

Figure B.2 The exemplary 100MHz MEMS oscillator with an ideal phase shifter inserted ........................................................................................................................ 105

Figure B.3 The oscillator loop gain and loop phase simulation ................................... 106

Figure B.4 The noise figure and transient waveform of the oscillator .......................... 106

Figure B.5 Comparison of the simulated and calculated phase noise ........................... 107

# SUMMARY

The main objective of this research is to develop temperature and frequency stabilization techniques for silicon MEMS oven-controlled crystal oscillators (MEMS OCXO) with high frequency stability. The device is built upon an ovenized platform that uses a micro-oven ($\mu$-oven) to adjust the temperature of the resonator. The structural resistance ($R_{struc}$) of the resonator is used as an embedded temperature sensor. The $R_{Struc}$ exhibits a large temperature coefficient of resistance (TCR) and is used as a self-temperature sensor to accurately and locally monitor the temperature of the resonator. This technique is not only accurate but also obviates the need for any additional temperature sensors. An analog resistance temperature detector (RTD), high-gain loop filter, and heater amplifier are implemented as the analog micro-oven control loop. The micro-oven resistor is automatically controlled by the analog control loop to provide active temperature stabilization for the resonator. In addition, we introduce a feedforward digital calibration method, which uses the digitized RTD output to fine tune the phase shift of the sustaining amplifier, to reduce the residual frequency error further. A high-Q capacitive all-silicon cross-sectional Lamé-mode resonator fabricated using the nano-gap HARPSS$^{TM}$ process is used as the frequency selective element. This 77MHz oven-controlled resonator has been demonstrated with the oscillator circuits implemented on a proof-of-concept printed circuit board (PCB). The analog feedback oven control loop achieves a ±2.5ppm frequency stability from -25°C to 85°C. The digital feed-forward calibration further improves the frequency stability to ±0.3ppm within the same temperature range. The micro-resonator is interfaced with a high-bandwidth sustaining amplifier and feedthrough cancellation circuit implemented in Taiwan Semiconductor Manufacturing Company 0.35-μm CMOS process, consuming 16 mA from a 3.2-V supply. This MEMS OCXO achieves the highest

frequency stability improving factor (5000X) compared with all other literatures. An AC heating scheme was also introduced, which enables tighter integration of the resonator, temperature sensor ($R_{struc}$) and heaters

In another part of this research, the temperature stabilization technique was applied to silicon MEMS high-Q resonant gyroscopes (x/y-axis and z-axis). To enable this, an electronic interface circuit for characterization of a single-chip three-axis high-frequency resonant gyroscopes was developed on a 3.5” by 3.5” PCB using off-the-shelf discrete electronic components. Every gyroscope uses its own analog drive loop and demodulation channel. A new low-pass high-pass trans-impedance amplifier (LP-HP TIA) topology is proposed. The LP-HP TIA incorporates two stages, the first stage is a high-gain low-bandwidth trans-impedance stage to ensure low-noise current-to-voltage conversion, and the second stage is a high-pass voltage amplifier to compensate the bandwidth loss. This new TIA topology can effectively extend the bandwidth, reduce the input-referred thermal and flicker noise, and increase the gyro scale factor. The simultaneous operation of all the three axes of the gyroscopes was demonstrated and less than 1.3% of cross-axis sensitivity of the tri-axial gyroscope was measured. Furthermore, the ovenized three-axis gyroscope showed that the frequency stability of the three axes gyros are improved by 54 times from -10°C to 70°C. The temperature-induced scale factor variations of the x/y and z axes gyro were reduced by factors of 23 and 233 times, respectively. The variation in the zero-rate output (ZRO) of the gyroscopes were also substantially reduced by ovenization. This is the very first time that a three-axis mode-matched resonant MEMS gyroscopes are being ovenized with the temperature sensor and heaters all integrated on the same chip.

# CHAPTER 1

# INTRODUCTION

This chapter will introduce the concept and common uses of timing and frequency references. The performance specifications and the main challenge, *temperature-induced frequency drift,* of silicon MEMS (micro-electro-mechanical systems) frequency references will be stated. The last part of this chapter will introduce the main building blocks of a complete MEMS frequency reference.

## 1.1 A Brief History of Timing References – From Quartz to MEMS

Timing references have been essential tools for human beings for thousands of years. Starting from the earliest manmade devices, sundials, people have pushed the technology further and invented better timekeeping devices like water clocks, spring wound watches, and pendulum clocks. In the 1700s, an English clockmaker, John Harrison, developed the first marine chronometer, a very accurate timing device for solving the problem of establishing the longitude of a ship at sea, thus revolutionizing and extending the possibility of safe long-distance sea travel in the Age of Sail. This invention included techniques for providing temperature compensation and removing the effects of ship motion. These techniques led to England's domination of the seas for several years before their competitors' developed similar timing technology.

Nowadays, timing devices have broadened their applications to digital communication via universal serial bus (USB), radio frequency communication via WLAN, and global positioning via GPS. Most of them are based on resonator technologies.

Among the large variety of resonators, quartz has dominated the market for several reasons. First, the resonant frequency of the quartz device is set by the dimensions and material properties of the resonator. Because of the crystalline structure, the material properties of quartz are highly stable and repeatable from one fabrication process to the next. Second, the piezoelectric property of quartz facilitates transduction from the mechanical vibrations to the electrical signal. Third, when quartz is cut at a certain angle, it exhibits very little temperature dependence. With proper design, the temperature sensitivity of a quartz resonator can be set to zero at one, or even two temperatures in a small range, and many cuts maintain less than 200 ppm of frequency shift over a 200°C range [1]. This makes quartz crystal oscillators (XOs) extremely advantageous. Additional temperature compensation techniques can be added to a standard XO to reduce the frequency variation by one or two orders of magnitude. For example, temperature-compensated crystal oscillators (TCXOs), which are commonly used in cell phones and portable electronics, can achieve a frequency stability of only a few parts per million (ppm). Microcomputer compensated crystal oscillators (MCXO), which use digital electronics to assist the temperature compensation process, can further improve the frequency stability to hundreds of parts per billion (ppb). A common application for MCXOs is navigation. The most temperature-stable quartz oscillators employ ovenization technology to stabilize the temperature of XOs and can minimize the frequency drift down to sub-ppb levels. This kind of oven-controlled crystal oscillator (OCXO) is commonly used in high-end navigation, radar, and measurement instruments.

Advances in quartz crystal oscillators have reached a plateau, while there has been an increasing demand for higher performance, size, cost, and integration. The new silicon MEMS technology that can provide quartz-level performance is starting to encroach on

quartz devices in many applications. The MEMS-based oscillators have been making rapid progress and gaining a larger market share in the recent years. The new MEMS technology is showing sufficient promise to supplant quartz from its dominant position and offers a few advantages that quartz cannot match:

1) Size: MEMS devices can be as small as several hundred of micrometers square. As the sizes of portable electronic devices shrink, smaller timing references become more and more desirable. The smaller size also allows the timing references to be placed closer to the device it is supporting, for better signal integrity and lower electromagnetic interference (EMI). In addition, when MEMS resonators are small and are located near their sense amplifiers, the parasitic capacitances at the inputs of the amplifiers are reduced, which results in less phase noise.
2) Cost: MEMS devices can be massively produced at one time on a single wafer by wafer-scale batch fabrication. In addition, while quartz resonators often require special packaging, MEMS technologies require only low-cost wafer-level packaging.
3) Frequency: Manufacturing high-frequency (> 100MHz) quartz resonators is difficult due to the fabrication challenges of implementing ultra-thin structures in quartz crystal. However, fabricating high-frequency MEMS resonators, even ones with a gigahertz frequency range, is relatively easy. While high-frequency resonators and timing references already have a large assortment of potential applications [2], [3], the demand for MEMS timing devices will certainly increase.
4) Integration: One of the major goals for timing references is their integration with modern CMOS integrated circuit (IC) processes, which should be easy since the CMOS IC processes use silicon, silicon dioxide, and metal for fabrication, and MEMS processes use the same materials. In addition, unlike quartz, which is a different

material and requires different manufacturing tools, MEMS and IC processes share many fabrication tools. Thus, there is a greater opportunity to integrate MEMS resonators with the CMOS IC technology on the same die. This benefit may thereby enable smaller system size, lower cost, closer thermal coupling and higher performance compared to discrete quartz resonators.

5) Stress immunity: MEMS oscillators are much less sensitive to vibration. Electronic systems, especially those are deployed outdoors, are often exposed to environmental stresses such as vibration. Examples of the vibration stresses are wind, heavy vehicles and trains. Cooling fan inside many systems is another source of vibration stress. These vibration stresses can induce frequency shift and noise in the crystal resonator. In extreme cases, vibration can cause system failure and service interruption, especially in systems that need very stable frequency references such as wireless base stations and small cells. A key reason MEMS oscillators are resistant to shock and vibration is because MEMS resonators have approximately 1,000 to 3,000 times lower mass than quartz resonators. This means a given acceleration imposed on a MEMS structure, such as from shock or vibration, will result in much lower force than its quartz equivalent and therefore induce a much lower frequency shift [4, 5].

The MEMS technology has challenged the predominant quartz crystal by providing a viable alternative solution. The solution is highly affordable and can satisfy the requirements of a wide range of industrial applications. MEMS has witnessed a significantly high penetration across different applications, such as timing references, pressure sensors, and motion sensors.

## 1.2 Performance Requirements and Specifications

The prime driver of frequency control technology is the military need. Modern military systems require oscillators/clocks that are stable over a wide range of parameters (time, temperature, acceleration, radiation, etc.), low noise, low power, small size, and fast warm-up. Table 1-1 summarizes the typical applications of quartz crystal oscillators [6]. The first four are commonly seen in commercial products while the last two are mainly used for military and aerospace purposes.

Table 1-2 summarizes most of the commercial quartz OCXOs with single-digit ppb frequency stability. The power consumption of these commercial quartz OCXOs is high (> 1Watt), and the warm-up time is long (> 5 minutes). The goal of this research is to develop a silicon MEMS OCXO prototype with frequency stability comparable to their quartz crystal counterparts across the industrial temperature range.

**Table 1-1**: Frequency reference temperature stability for different applications [6]

| Oscillator Type | Accuracy | Typical Applications |
|---|---|---|
| Crystal & MEMS Oscillators | $10^{-5} \sim 10^{-4}$ | Computer timing |
| Temperature Compensated Crystal Oscillators (TCXO) | $10^{-6}$ | Frequency control in tactical radios |
| Microcomputer Compensated Crystal Oscillators (MCXO) | $10^{-8} \sim 10^{-7}$ | Spread spectrum system clock |
| Oven Controlled Crystal Oscillators (OCXO) | $10^{-8} \sim 10^{-9}$ | Navigation system clock & frequency standard, MTI radar |
| Small Atomic Frequency Standard (Rb, RbXO) | $10^{-9}$ | $C^3$ satellite terminals, bistatic, & multistatic radar |
| High Performance Atomic Standard (Cs) | $10^{-12} \sim 10^{-11}$ | Strategic $C^3$, EW |
| *Including environmental effects (e.g., -40°C to +75°C) and one year of aging<br>**$C^3$: Command, control, and communications, a military concept | | |

**Table 1-2**: Quartz OCXOs commercial products with single-digit ppb frequency stability

| Product | **Vectron** OX-300 | **Rakon** RK409 | **Connor-Winfield** OH200-60603CF | **CTS** 1180026 | **Abracon** AOCTQ5 | **Wenzel** Small Fry |
|---|---|---|---|---|---|---|
| $f_0$ (MHz) | 10 | 10 | 12 | 20 | 10 | 10 |
| Cut | SC | -- | -- | SC | SC | SC |
| Temp. Range (°C) | -40 to 85 | -40 to 85 | -40 to 85 | -40 to 85 | -40 to 85 | -55 to 85 |
| Freq. Stability (ppb) | ±3 | ±1 | ±3 | ±3.5 | ±3 | ±5 |
| Phase Noise (dBc/Hz) | -95 @ 1Hz<br>-122 @ 10Hz<br>-133 @ 100Hz<br>-143 @ 1kHz<br>-151 @ 10kHz | -105 @ 1Hz<br>-135 @ 10Hz<br>-145 @ 100Hz<br>-150 @ 1kHz<br>-155 @ 10kHz | -85 @ 1Hz<br>-115 @ 10Hz<br>-140 @ 100Hz<br>-145 @ 1kHz<br>-150 @ 10kHz | -70 @ 1Hz<br>-103 @ 10Hz<br>-130 @ 100Hz<br>-140 @ 1kHz<br>-142 @ 10kHz | - @ 1Hz<br>-120 @ 10Hz<br>-140 @ 100Hz<br>-145 @ 1kHz<br>-155 @ 10kHz | - @ 1Hz<br>-130 @ 10Hz<br>-155 @ 100Hz<br>-165 @ 1kHz<br>-165 @ 10kHz |
| Power Cons. @ 25°C (W) | 1.35 | 2 | 1.5 | 1.5 | 1.6 | 1.3 |
| Warm-up Time (min.) | 5 (±100ppb) | 30 | 5 | 15 (±10ppb) | 10 (±5ppb) | 5 |
| Package Size (mm) | 21 x 21 x 11 | 50 x 50 x 30 | 28 x 35 x 13 | 26 x 26 x 13 | 36 x 27 x 12 | 38 x 38 x 76 |
| Price (USD) | | $4000 | $136 | $77 | $156 | |

## 1.3 Origin of the Problem – Temperature-Induced Frequency Drift

The main drawback of silicon MEMS devices is their large temperature coefficient of frequency (TCF, typically -30ppm/°C), which has challenged their commercial viability. Hence, the mainstream research on silicon MEMS resonators and oscillators has focused on temperature compensation techniques as well as efficient electromechanical transduction schemes to realize temperature-stable MEMS frequency references.

Both the resonance frequency ($f_0$) and the quality factor ($Q$) of MEMS resonators typically show large temperature sensitivities. The thermal behavior of $Q$ is still under

further investigation because it depends on the geometry, operation mode, and frequency of the resonator. The temperature dependency of $f_0$ has been well characterized. Furthermore, while quartz resonators of certain crystal cuts show relatively small temperature dependency, uncompensated MEMS resonators show a large linear TCF. The first-order temperature sensitivity of $f_0$ can be defined by the following equation:

$$TCF = \frac{1}{f_0} \cdot \frac{\partial f_0}{\partial T} \approx \frac{1}{2}(TCE + CTE) \quad (1.1)$$

where TCE is the temperature coefficient of Young's modulus, and CTE is the coefficient of thermal expansion. Although this expression can be derived easily for MEMS resonators operating in extensional bulk acoustic or flexural modes, TCF of resonators operating in any arbitrary mode is more complicated and may not be formulated in closed form. The large TCF of MEMS resonators is due mainly to high TCEs of the materials commonly used. For native silicon resonators, the large native TCF of -30ppm/°C results in a frequency drift as large as 3750 ppm across the industrial temperature range of -40°C to 85°C. Major applications of MEMS resonators, such as temperature-compensated oscillators and thermally-stable sensors, often require sub-ppm instability levels, mandating a radical decrease in the TCF to facilitate full compensation through dynamic mechanisms such as active electronic methods. Therefore, passive TCF compensation techniques are of great interest. Examples of these techniques are the compensation of TCE through doping-profile engineering [7, 8, 9, 10, 11, 12] ; engineering device geometry to operate in resonance modes defined by elastic coefficients with lower TCF [13]; the addition of a compensating material with a TCE of the opposite sign to form a composite structure with reduced TCF [14].

Doping-profile engineering techniques introduce dopants into the substrate and reduce its large TCE by modifying the electronic energy levels. Different works in this category include utilization of heavily P-doped [8], [7] and N-doped silicon substrates [9], [10], thermo-migration of aluminum atoms into the silicon substrate [11], and carrier depletion of the device using multiple PN junctions [12]. The efficiency of doping-profile engineering depends considerably on the resonance mode as well as the relative crystallographic orientation of the device. Removal of the $1^{st}$-order temperature dependency results in a 2nd-order parabolic temperature characteristic. In addition to improving the overall frequency drift, this 2nd-order characteristic possesses a turn-over point with a zero local TCF. A turn-over point designed to be at a higher and proper temperature can facilitate implementation of an OCXO, minimizing the TCF at the target operating temperature. Figure 1.1 shows the temperature characteristic of a silicon bulk acoustic resonator with thin-film aluminum nitride (AlN) transduction, oriented in <100> crystal direction of a heavily doped silicon substrate, to achieve an overall frequency variation of 150ppm over the temperature range -40°C to 85°C.

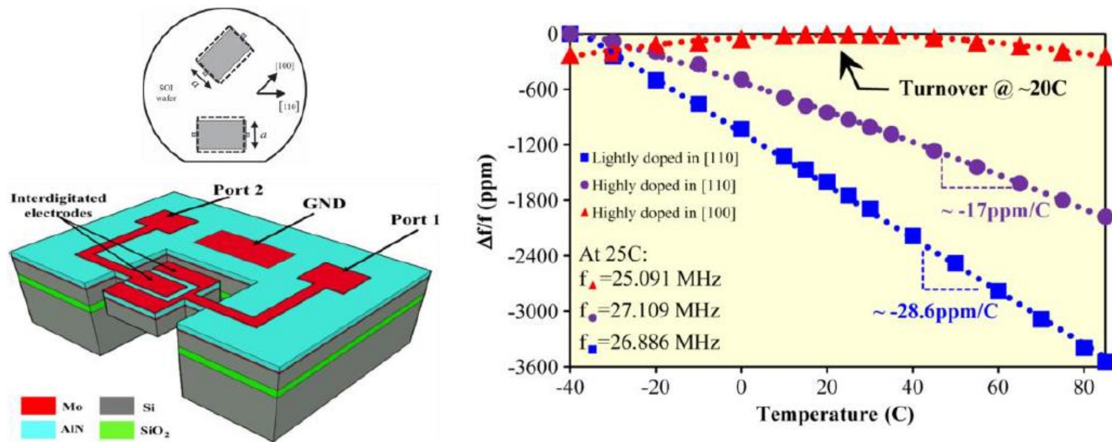


**Figure 1.1**: Temperature characteristics of extensional mode resonators aligned in the different crystallographic direction of silicon and for different doping concentrations [9]

An example of device geometry engineering is depicted in Figure 1.2 [13]. The SEM image shows a TCF-compensated concave silicon bulk acoustic resonator (CBAR) in comparison with a rectangular geometry silicon bulk acoustic resonator (SiBAR). The CBAR geometry excites a resonance mode with a large energy concentration in shear acoustic fields and thus considerably reduce the TCF. Furthermore, it shows significant improvement in *Q* due to the efficient compensation of energy leakage from the resonator towards the surrounding substrate [13]. This technique improves the TCF to -6.3ppm/°C (= 756ppm total from -40°C to +80°C).

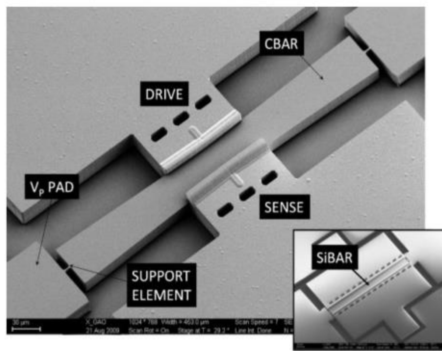


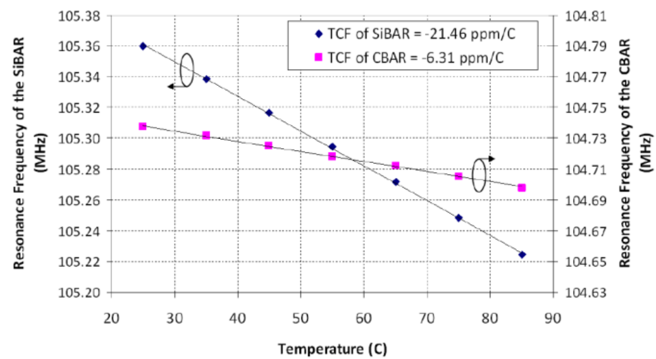


**Figure 1.2**: (left) Geometry-engineered concave SiBAR (CBAR) (right) device shows a TCF of -6 ppm/°C at 105MHz with a Q of 100 [13]

Addition of compensating material is a traditional way to reduce TCF. The negative TCE of native silicon is compensated by the addition of a material with positive TCE (usually $SiO_2$). Adding the correct amount of $SiO_2$ forms a composite $Si/SiO_2$ structure with temperature-compensated TCE. $SiO_2$ can be added in layers parallel to the resonator stack and is called *surface $SiO_2$ compensation* [15], [16]. Thick layers of $SiO_2$, comparable to that of silicon, is required to provide a full compensation of linear TCF. Hence this technique is mostly applicable to thin substrates and low-frequency flexural or extensional

mode resonators. Alternative TCF compensation for a thick and high-frequency silicon resonator has been demonstrated by a 27 MHz BAW resonators with piezoelectric transduction [14]. In this case, bulk $SiO_2$ is embedded inside the resonator body by carefully filling trenches with thermppmal of LPCVD $SiO_2$ to provide a solid voidless platform. Figure 1.3 shows the temperature compensated piezoelectric AlN-on-SilOx resonator in [14] with added $SiO_2$ pillars as compensation material. The total frequency drift is reduced to 90 ppm from -40°C to +80°C

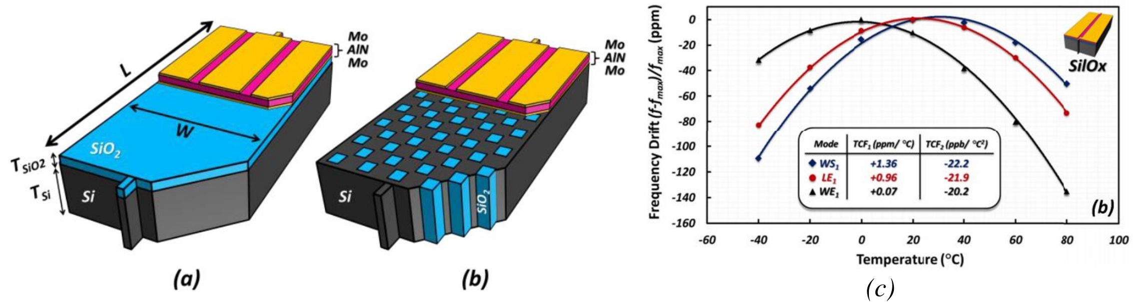


**Figure 1.3**: Silicon piezoelectric resonators with (a) surface oxide compensation, (b) bulk oxide compensation, and (c) measured temperature characteristic of three different resonance modes [14]

## 1.4 Motivation

Although the device-level temperature compensation techniques mentioned in section 1.3 are somewhat effective, the best result still shows several tens of ppm frequency variation. This performance cannot satisfy the accuracy requirement of most of the applications in Table 1-2. So, circuit and system-level temperature compensation techniques must be developed to further improve the frequency accuracy down to sub-ppm level. The major objective of this research is to develope system-level temperature compensation techniques for silicon MEMS resonators and frequency references.

# CHAPTER 2

# MEMS RESONATOR AND OSCILLATOR BASICS

This chapter will begin with the operation principle of electrostatic MEMS resonator and then introduce the equivalent circuit model. The second section will delve into the operation principle of MEMS oscillators and give an overview of all the building blocks in a general MEMS oscillator.

## 2.1 MEMS Resonator Basics

Before getting into details of MEMS oscillators, the basic operation and the transduction mechanism of MEMS resonators should be introduced. The transduction can be divided into two steps:

1) Drive: apply a voltage to actuate a MEMS resonator to convert the electrical signal into a mechanical motion
2) Sense: convert the mechanical motion back into an electrical signal

Electrostatic and piezoelectric actuation/sensing are the two most common transduction mechanisms in the MEMS community. Because silicon is not a piezoelectric material, piezoelectric transduction requires alternative materials (such as aluminum nitride, quartz, or lead zirconate titanate) and generally entails more advanced fabrication techniques compared to electrostatic structures. The experiments and devices described in this thesis rely exclusively upon electrostatic transduction. The only fabrication requirement imposed by electrostatic transduction is the need for small capacitive gaps ($< 1\mu m$). Here, we use a MEMS clamped-clamped silicon beam resonator with symmetric capacitive transducers (Figure 2.1) to explain the electrostatic transduction mechanism.

The drive and sense electrodes shown in Figure 2.1 are fixed. The center region of the clamped-clamped beam can move in response to external (electrostatic) force.

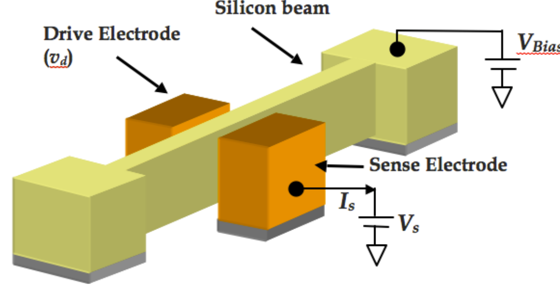


**Figure 2.1**: A MEMS clamped-clamped silicon beam resonator with symmetric capacitive transducers

The beam is biased to a dc voltage, $V_{\text{Bias}}$, and the two electrodes have zero dc bias ($V_S$ = 0V). By applying an ac signal to the drive electrode, the electrostatic force ($F_{\text{elec}}$) experienced by the beam can be expressed as

$$F_{elec} = \frac{1}{2}(V_{Bias} - v_d)^2 \frac{\partial C_d}{\partial x} + \frac{1}{2}(V_{Bias} - V_S)^2 \frac{\partial C_s}{\partial x} \tag{2.1}$$

where $v_d$ is the small ac actuation voltage, $x$ is the displacement of the beam, $C_d$ is the overlapping capacitance between the drive electrode and the beam, and $C_s$ is the overlapping capacitance between the sense electrode and the beam.

$$C_d = \frac{\varepsilon A}{d - x}, \quad C_s = \frac{\varepsilon A}{d + x}, \quad \left(C_0 = \frac{\varepsilon A}{d}\right) \tag{2.2}$$

In (2.2), $\varepsilon$ is the absolute permittivity, $A$ is the capacitance area of $C_d$ and $C_s$, $d$ is the rest gap size between the drive/sense electrode and the beam, and $C_0$ represents the rest capacitance of the drive and sense gaps. Because $V_S$ = 0V, the DC force on the drive and

sense capacitors cancel out. And we assume that $v_d << V_{Bias}$, and $x << d$. The net ac actuating force applied to the beam becomes

$$F_{elec} = -\frac{C_0 V_{Bias}}{d} v_d \tag{2.3}$$

Equation (2.3) shows that the electrical voltage can be transformed into the mechanical domain as a force acting on the moveable MEMS structure.

Now we consider the "sense" part of the transduction process. Because there is a fixed voltage, $V_{Bias}$, existing across the sense capacitance $C_s$, a current $I_S$ will flow out of the sense electrode according to the equation below.

$$I_S = \frac{d}{dt}(C_s V_{Bias}) = V_{Bias}\frac{d}{dt}\left(\frac{\varepsilon A}{d+x}\right) \approx -\frac{C_s V_{Bias}}{d}\frac{dx}{dt} \tag{2.4}$$

In (2.4), we assumed that $x << d$, again. Unlike the actuation part, $V_{Bias}$ is a necessary factor to generate $i_{sense}$ on the sense side.

To obtain expression of the displace $x$, we approximate the resonator system to a parallel plate capacitor and assume the beam behaves as a second order mechanical system.

$$M\frac{\partial^2 x}{\partial t^2} + D\frac{\partial x}{\partial t} + k \cdot x = F_{elec} \tag{2.5}$$

$M$, $D$ and $k$ are the mass, damping and spring constant of the beam respectively and are related to the resonance frequency ($\omega_{res}$) and the quality factor ($Q$) by:

$$\omega_{res} = \sqrt{\frac{k}{M}}, \quad Q = \frac{1}{D}\sqrt{k \cdot M} \tag{2.6}$$

By applying the Laplace transform and then substituting $s$ with $j\omega$, we have

$$\frac{X(j\omega)}{F_{elec}(j\omega)} = \frac{1}{M\omega_{res}} \frac{1}{\left(1 - \frac{\omega^2}{\omega_{res}^2}\right) + j\frac{1}{Q}\left(\frac{\omega}{\omega_{res}}\right)} \tag{2.7}$$

Assume the device is operating at the resonance frequency $\omega_{res}$, the magnitude and phase of (2.7) becomes

$$\left|\frac{X}{F_{elec}}\right| = \frac{Q}{M\omega_{res}^2} \quad , \quad \angle\frac{X}{F_{elec}} = -90° \tag{2.8}$$

Now we apply Laplace transform to (2.4) and substitute $s$ with $j\omega$ and replace $\omega$ *with* $\omega_{res}$.

$$\frac{I_S}{X} \approx \frac{C_0 V_{Bias}}{d} j\omega \quad \Rightarrow \quad \left|\frac{I_S}{X}\right| \approx \frac{C_0 V_{Bias}\omega_{res}}{d}, \quad \angle\frac{I_S}{X} = 90° \tag{2.9}$$

Finally, the overall transfer function magnitude can be derived as

$$\left|\frac{I_S}{v_d}\right| = \left|\frac{I_S}{X}\right|\left|\frac{X}{F_{elec}}\right|\left|\frac{F_{elec}}{v_d}\right| = \frac{C_0 V_{Bias}\omega_{res}}{d} \cdot \frac{Q}{M\omega_{res}^2} \cdot \frac{C_0 V_{Bias}}{d} = \frac{Q C_0^2 V_{Bias}^2}{M d^2 \omega_{res}} \tag{2.10}$$

The total phase of the transfer function can be obtained in a similar way as 360°. Figure 2.2 shows the summary of the beam resonator transduction process and transfer function.

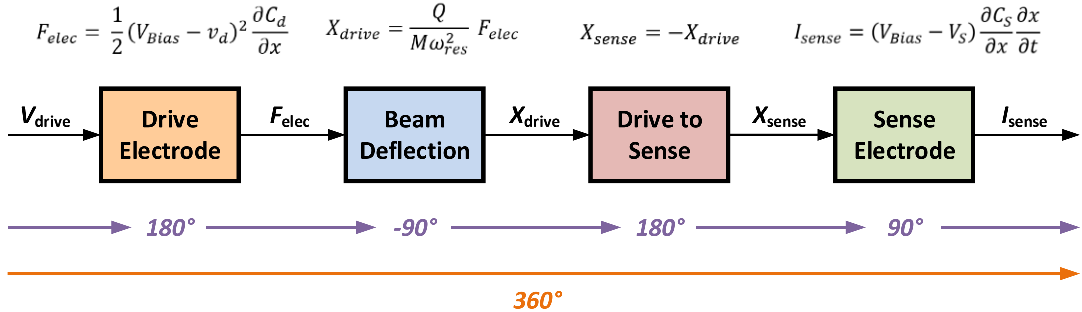


**Figure 2.2**: Summary of the beam resonator transfer function

For convenience, an equivalent circuit model of the resonator is often used instead of the mechanical transfer function. The second order transfer function can be modeled using a simple series RLC as shown in Figure 2.3. The core transduction part can be modeled as a series combination of a resistor ($R_m$), a capacitor ($C_m$), and an inductor ($L_m$). This RLC

combination is called the *motional impedances* of the resonator. The parameters for $R_m$, $C_m$, and $L_m$ are given in Table 2-1.

The motional resistance, $R_m$, is the most important parameter because it defines the ratio of the output current signal to the input voltage signal when the device is driven at its resonance frequency. Many researches have been reported to reduce this resistance value from the typical range of kilo-Ohms or even Mega-Ohms to hundreds of Ohms. Large motional resistance value can complicate the design for the sustaining amplifiers in oscillators.

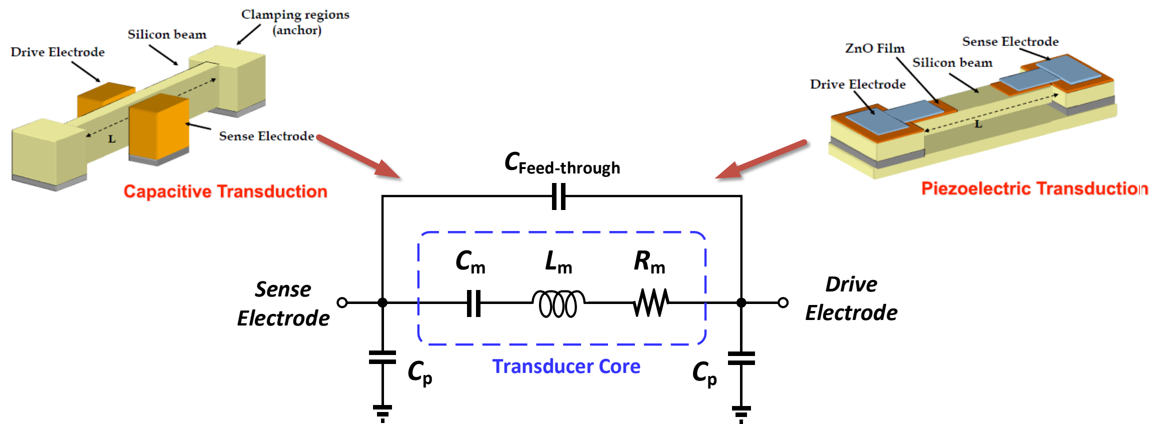


**Figure 2.3**: Equivalent RLC model of electrostatic (capacitive) and piezoelectric MEMS resonators

Table 2-1
RLC parameters for the equivalent model of electrostatic MEMS resonator

| Circuit Element | $R_m$ | $L_m$ | $C_m$ |
|---|---|---|---|
| **Mechanical Parameters** | $\frac{Md^2\omega_{res}}{QC_0^2V_{Bias}^2}$ | $\frac{kd^2}{\omega_{res}^2C_0^2V_{Bias}^2}$ | $\frac{C_0^2V_{Bias}^2}{k\cdot d^2\left(1-\frac{2V_{Bias}^2C_0}{k\cdot d^2}\right)}$ |

The shunt parasitic capacitance from the drive/sense electrodes to ground is represented as $C_p$. Basically, this shunt parasitic capacitance has only negative impact on the oscillator design. The stray capacitance between the drive and sense terminals forms a feedthrough capacitor $C_{FT}$ and is usually more noticeable in capacitive resonators than in piezoelectric resonators. $C_{FT}$ adds an anti-resonance peak and an additional phase transition from -90° to +90°. When $C_{FT}$ is small compared to $1/\omega_0 R_m$, its effects can sometimes be neglected. However, $C_{FT}$ can be a limiting factor for high-frequency MEMS devices (capacitor admittance increases with frequency). If the anti-resonance occurs too close to the main resonance, the resonator phase may not transition fully from +90° to below 0°. This can significantly complicate the design of a sustaining oscillator. To reduce the total $C_{FT}$, differential structure and shielding between the drive and sense electrodes are effective methods. In addition, some circuit techniques have been developed to minimize the effect of feedthrough capacitance. The feedthrough cancellation circuits will be discussed in detail in Chapter 4.

## 2.2 MEMS Oscillator Basics

To initiate an oscillation, the "Barkhausen Criterion" must be satisfied at the resonant frequency for an oscillator.

1. The total loop gain must be greater than or equal to one.

2. The phase shift around the loop must be 0° or 360°.

Figure 2.4 illustrates the concept of this oscillation criterion. In addition, a nonlinear mechanism must be present to limit the oscillation amplitude. In reality, there are always some effects in a system that limit the oscillation amplitude to a finite value. In MEMS

oscillators, this effect comes from the nonlinear dynamics of the MEMS device itself. However, it is usually preferred not to drive the MEMS device with too large an amplitude, as this can degrade the device performance or even damage the device. This limiting function can also come from the inherent nonlinearity of an amplifier or a designer-added clamping or automatic gain control circuitry.

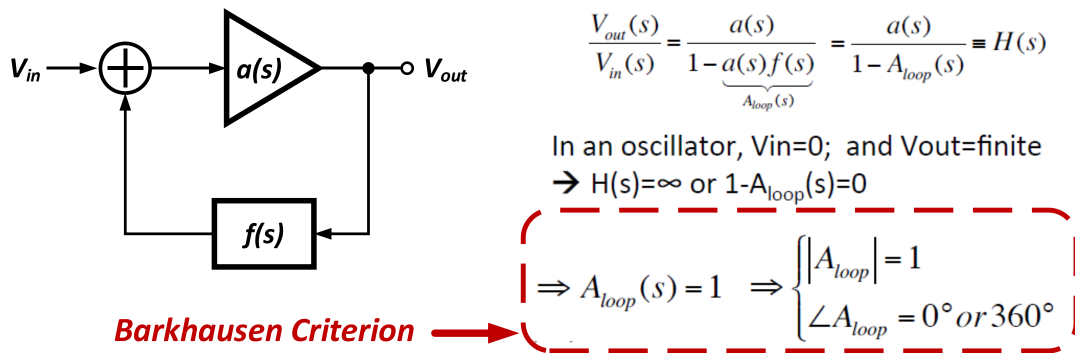


**Figure 2.4**: Illustration of Barkhausen Criterion for oscillation

The RLC equivalent model (Figure 2.3) of a resonator takes a voltage as the input and provides a current to the bias voltage of the sense electrode as the output. Therefore, a transimpedance amplifier (TIA) that converts the current signal (input) to the voltage signal (output) is often chosen to interface the resonator for completing the feedback loop of an oscillator.

Figure 2.5 shows a typical MEMS oscillator implementation. This implementation consists of an electrostatic (capacitive) MEMS resonator, TIA, phase shifter, variable gain amplifier (VGA), automatic level control (ALC) circuitry, and an output buffer. The body of the resonator is biased to a DC voltage (polarization voltage, $V_P$) to create a voltage

difference between the sense electrode and the resonator to enable the transduction. The combination of TIA, phase shifter, VGA and ALC is called the *sustaining amplifier*.

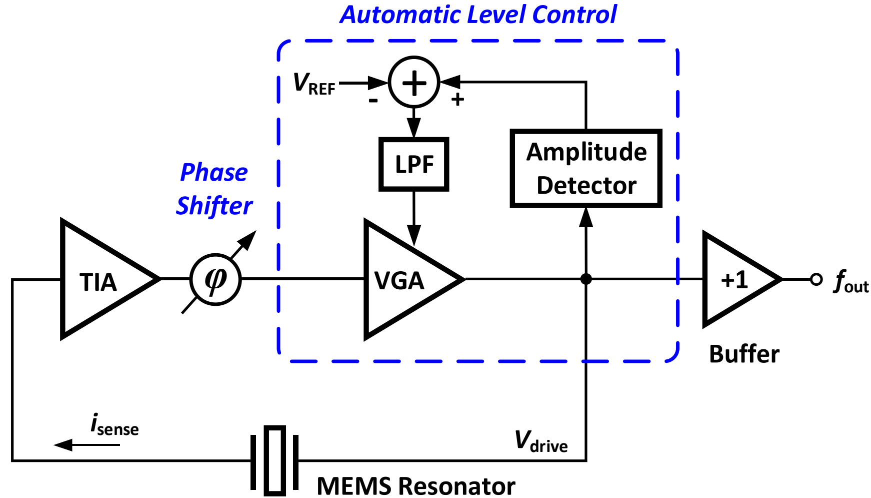


**Figure 2.5**: General implementation for an electrostatic MEMS oscillator.

The TIA and VGA provide an overall transimpedance gain larger than $R_m$ to meet the Barkhausen loop gain criterion at $f_{res}$. Achieving small motional impedance in electrostatic resonators often requires minuscule transduction gaps (< 1μm). This process is difficult. Special fabrication techniques are needed, particularly in processes with high aspect ratios. The MEMS resonators in this work (introduced in Chapter 3 and 5) use the High-Aspect-Ratio combined Poly- and Single-crystal Silicon (HARPSS$^{TM}$) process [17] to create narrow (200nm) air gaps. Such a narrow gap enables small motional resistance at high frequency and, hence, relaxes the design of the sustaining amplifier. The phase shifter compensates for the unwanted phase shift from the TIA and VGA to ensure the loop exhibits a 360° phase at the resonance frequency (Barkhausen loop phase criterion). The ALC circuitry keeps the drive amplitude constant to avoid driving the MEMS resonator into nonlinear regime or breaking the device. Limiting the drive amplitude makes the

output waveform more like sinusoidal than square, which introduces less nonlinearity and benefits the close-in phase noise. The output buffer is used to drive the other circuits or instruments, and to isolate the loop from any extra loading. In the following, the typical implementations of each building block in an oscillator will be introduced.

### 2.2.1 Transimpedance Amplifier (TIA)

The most import performance parameters of TIA used in MEMS oscillators are gain, bandwidth and input-referred noise current. TIA converts the small sense current into a voltage signal, so the gain has the unit of Ohm (Ω). The TIA gain should be large enough to compensate the insertion loss ($R_m$) and to suppress the second stage noise of the sustaining amplifier. The TIA bandwidth doesn't need to be broad band because we only care about the gain at $f_{res}$. The input-referred noise current should be minimized to achieve better phase noise and ADEV performance. For the thermal noise, we only care about the spot noise at $f_{res}$, which mainly affects the far-out phase noise. For the flicker noise, although it is usually in low-frequency band far from the resonance frequency, it can be modulated to $f_{res}$ to degrade the close-in phase noise due to the nonlinear effect in the oscillator loop.

There are three commonly seen TIA topologies: common gate, resistive feedback and capacitive feedback. The typical implementations of common gate TIAs are shown in Figure 2.6. The transimpedance gain, pole frequencies and input-referred noise are summarized in Table 2-2. The main advantage of common gate TIA is the broad bandwidth due to the low input impedance ($R_{in}$ = $1/g_{m1}$). In optical communication and MEMS oscillator applications, there is often a large parasitic capacitance ($C_{in}$) of several picofarad to ground at the input. The low input impedance can provide a wide bandwidth even with

such a parasitic capacitance. The second advantage is that there is no feedback, so there is no stability concern.

The drawbacks of the common gate TIA are listed below.

1) The noise currents of $M_2$ and $R_D$ are directly referred to the input. At high frequency, the noise of $M_1$ comes into play, which scales with $C_{in}$ and frequency.
2) It is difficult for low-voltage design because both $M_2$ and $R_D$ need more voltage headroom to reduce their noise currents (trade-off)
3) The TIA gain ($R_D$) is hard to be high because higher $R_D$ requires more voltage head room. The noise contributed by the subsequent stage can be significant.

Figure 2.6(b) shows an improved version of the common gate TIA, which has an auxiliary amplifier to boost the $g_m$ of $M_1$. The input impedance is reduced by (1+$A$) times, and, hence, the input pole frequency is increased by (1+$A$) times. This input stage topology is often referred to as "regulated cascode". In brief, the common gate TIA is good for high-frequency application but not suitable for low-noise design.

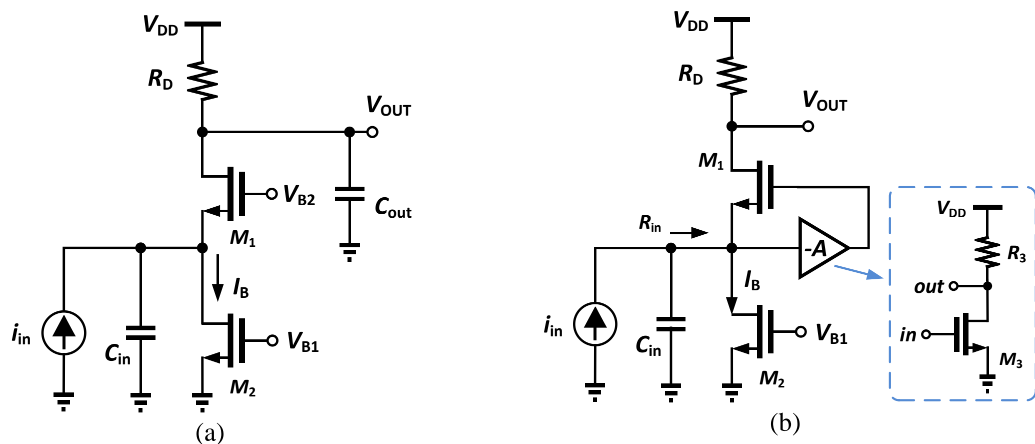


**Figure 2.6**: (a) The basic common gate TIA, and (b) the common gate TIA with gm boosting

Table 2-2
The performance parameters of the common gate TIA

| **Common Gate TIA** | |
|---|---|
| **Gain (Ω)** | $\approx R_D$ |
| **Pole Frequencies (rad/s)** | $\omega_{p1} = \frac{g_{m1}}{C_{in}}, \quad \omega_{p2} = \frac{1}{R_D C_{out}}$ |
| **Input-referred Noise Current (A/$\sqrt{Hz}$)** | At low frequency: $\overline{I_{n,in}^2} \approx 4kT\left(\gamma g_{m2} + \frac{1}{R_D}\right)$<br>At high frequency: $\overline{I_{n,in}^2} = \left(\frac{C_{in}s}{g_{m1}}\right)^2 \overline{I_{n,M1}^2} + \left(\frac{C_{in}s}{g_{m1}} + 1\right)^2 \overline{I_{n,RD}^2} + \overline{I_{n,M2}^2}$ |
| **Common Gate TIA + gm boosting** | |
| **Gain (Ω)** | $\approx R_D$ |
| **Pole Frequencies (rad/s)** | $\omega_{p1} = \frac{g_{m1}(1 + g_{m3}R_3)}{C_{in}}, \quad \omega_{p2} = \frac{1}{R_D C_{out}}$ |
| **Input-referred Noise Current (A/$\sqrt{Hz}$)** | Similar to the original common gate TIA |

The resistive feedback TIA topology is shown in Figure 2.7. This topology consists of an inverting voltage amplifier and feedback resistor ($R_F$) between the input and output. If the amplifier's gain is high enough, the TIA gain is close to -$R_F$.

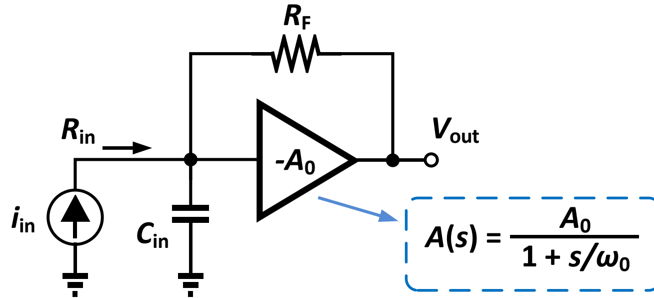


**Figure 2.7**: The resistive feedback TIA topology

The transimpedance gain, transfer function, bandwidth and input-referred noise are summarized in Table 2-3. The main advantage of this topology is the relaxed tradeoff

between TIA gain (≈-$R_F$) and the voltage headroom. Because there is no dc current flowing through $R_F$, the TIA gain can be increased without sacrificing any voltage headroom. Compare to the common gate TIA, the larger $R_F$ not only contributes less noise current to the input but also suppresses the noise from the second stage more. In addition, there is no current source noise ($M_2$ in Figure 2.6) directly flowing into the TIA input.

Table 2-3
The performance parameters of the resistive feedback TIA

| **Resistive feedback TIA** | |
|---|---|
| **Gain (Ω)** | ≈ -$R_F$ |
| **Pole Frequencies (rad/s)** | $\omega_{p1} = \frac{(1+A)}{R_F C_{in}}$ |
| **Transfer Function** | $\frac{V_{out}}{I_{in}} = -\frac{A_0\,\omega_0/C_{in}}{s^2 + \frac{R_F C_{in} + 1/\omega_0}{R_F C_{in}/\omega_0} + \frac{(A_0+1)\omega_0}{R_F C_{in}}}, \quad \xi = \frac{1}{2}\frac{R_F C_{in}\omega_0 + 1}{\sqrt{(A_0+1)\omega_0 R_F C_{in}}}$ ($\xi$ = damping factor) |
| **Bandwidth (rad/s)** | $when\ \xi = \frac{1}{\sqrt{2}}, \quad \omega_0 = \frac{2A_0}{R_F C_{in}}, \quad \omega_{3dB} = \sqrt{\frac{(1+A_0)\omega_0}{R_F C_{in}}} \approx \frac{\sqrt{2}A_0}{R_F C_{in}}$ |
| **Input-referred Noise Current (A/$\sqrt{Hz}$)** | $\overline{I_{n,in}^2} \approx 4kT\frac{1}{R_F} + \overline{V_{n,A}^2}\left(\frac{1}{R_F^2} + \omega^2 C_{in}^2\right)$ |

The resistive feedback TIA has two drawbacks. First, the input resistance may not be as small as common gate topology, especially when $g_m$ boosting technique is applied. Second, the inverting amplifier design can be challenging if a high TIA bandwidth is required. In brief, the resistive feedback TIA is suitable for low-noise applications, but bandwidth may be lower than the common gate topology (design challenge). For discrete implementation, OPA657, OPA656, ADA4817 and LTC6268 are high-bandwidth and low-noise commercial off-the-shelf opamps, which should be considered.

The capacitive feedback TIA topology is shown in Figure 2.8 [18]. This topology consists of an inverting voltage amplifier, one feedback capacitor ($C_1$) and an output current buffer ($M_1$). If the gain $A_0$ is high enough, the circuit behaves as a current amplifier with a current gain of $(1+ C_2/C_1)$.

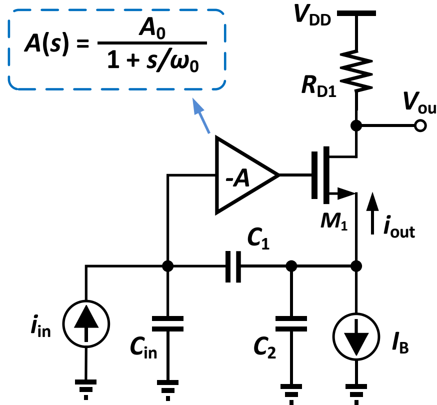


**Figure 2.8**: The capacitive feedback TIA topology [18]

The transimpedance gain, bandwidth and input-referred noise are summarized in Table 2-4. The key feature of this topology is that it can achieve a high transimpedance gain without involving large resistance because of the current factor $(1+C_2/C_1)$. The other advantages of this topology are listed below.

1) Compare to common gate TIA, both the $R_D$ and $I_B$ noises are suppressed by the factor of the current gain $(1+C_2/C_1)$.
2) The capacitive feedback network and gain $(1+ C_2/C_1)$ do not contribute noise.
3) The pole from $R_D C_{out}$ appears outside the feedback loop, it does not affect the loop stability (compared to resistive feedback TIA).

The main drawback of this topology is that the noise of $M_1$ may kick in if the operating frequency is higher than the bandwidth of amplifier ($-A$). In brief, the capacitive feedback

TIA topology is suitable for low-noise applications and exhibits a comparable bandwidth as the common gate topology.

Table 2-4
The performance parameters of the capacitive feedback TIA [18]

| **Capacitive feedback TIA** | |
|---|---|
| **Gain (Ω)** | $\approx \left(1+\frac{C_2}{C_1}\right) R_{D1}$ |
| **Bandwidth (Hz)** | $assume\ \ \omega_0^2 \gg \left(\frac{g_{m1}}{C_2}\right)^2, \qquad \omega_{3dB} = \frac{g_{m1}}{\sqrt{2}C_2}$ |
| **Input-referred Noise Current (A/$\sqrt{Hz}$)** | $\overline{I_{n,in}^2} \approx \frac{4kT}{R_{D1}\left(1+\frac{C_2}{C_1}\right)^2} + \frac{\overline{I_{n,IB}^2}}{\left(1+\frac{C_2}{C_1}\right)^2} + \overline{V_{n,A}^2}\left[\omega^2\left(C_{in}+C_1\right)^2\right]$ |

## 2.2.2 Variable Gain Amplifier (VGA)

The variable gain amplifier is the most important part of the ALC circuitry. A good VGA provides a wide gain tuning range and a stable bandwidth under different gain settings. For analog controlled VGA, a control voltage ($V_C$) is applied the control pin to adjust the voltage gain. Usually, a linear-in-dB gain tuning characteristic ($V_C$ v.s. gain in dB) is preferred for an ALC loop to achieve a constant loop settling time. However, linear-in-magnitude ($V_C$ v.s. gain in V/V) VGAs can also be found among commercial off-the-shelf components.

For integrated circuit design, using a variable resistor is a very common way to realize the gain tuning function in a VGA. Figure 2.9 shows three examples of variable resistor-based VGAs. Their gain equations are also listed in the same figure. MOSFET transistors are used to implement variable resistors very often. The gate of a transistor can serve as the gain tuning node. The advantages are the large gain tuning range and easy

implementation. However, to achieve a linear-in-dB gain tuning curve, extra design effort is required. The main drawback of this method is the bandwidth and phase variation due to the resistance change.

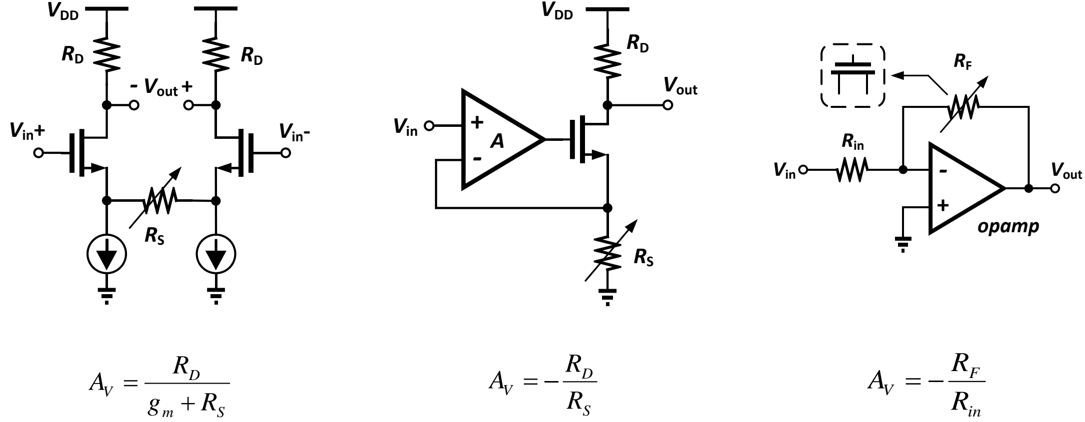


$$A_V = \frac{R_D}{g_m + R_S} \qquad A_V = -\frac{R_D}{R_S} \qquad A_V = -\frac{R_F}{R_{in}}$$

**Figure 2.9**: Three examples of variable-resistor based VGAs

Figure 2.10(a) shows another VGA topology with pseudo exponential gain tuning characteristic [19]. The gain tuning mechanism is based on redistributing the bias currents of the input differential pair ($I_{\text{input}}$) and active loads ($I_{\text{load}}$) to approximate an exponential curve. The exact gain expression is shown below.

$$A_V = \frac{g_{m.input}}{g_{m.load}} = \sqrt{\frac{(W/L)_{input} \cdot (I_{SS} + \Delta I)}{(W/L)_{load} \cdot (I_{SS} - \Delta I)}} = K\left(\frac{1+x}{1-x}\right)^{0.5} \tag{2.11}$$

Figure 2.10(b) shows a numerical analysis of how close the equation in (2.11) can be to a real exponential function. The pseudo exponential function with $K$=1 can approximate the exponential function $e^{1.2x}$ with < 0.5dB error within the -0.7 < x < 0.7 range. The major advantage of this topology is that it avoids using the parasitic bipolar devices in CMOS IC processes. Although the gain tuning range of this VGA is not large, a wider gain tuning range can be achieved by cascading multiple stages.

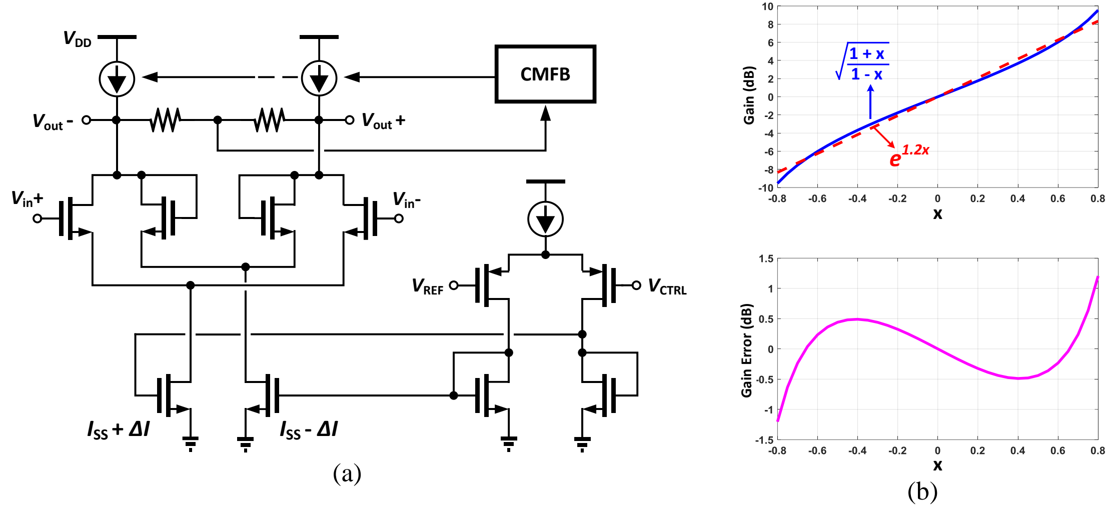


**Figure 2.10**: (a) The pseudo exponential gain control VGA [19], and (b) the gain tuning curve

Figure 2.11 shows another popular VGA topology - the Gilbert cell-based VGA. This output of this VGA is proportional to the output current difference of two input differential pairs ($M_{3,4}$ and $M_{5,6}$). So, by redistributing the tail currents (adjust $V_{RF}$) of these two differential pairs, a wide gain tuning range can be achieved. The exact input-output relationship can be expressed as

$$V_{out} = I_{SS}R\left(\frac{V_{RF}}{V_{GS1}-V_{TH}}\right)\sqrt{1-\left[\frac{V_{RF}}{2(V_{GS1}-V_{TH})}\right]^2}\left(\frac{V_{LO}}{V_{GS3}-V_{TH}}\right)\sqrt{1-\left[\frac{V_{LO}}{2(V_{GS3}-V_{TH})}\right]^2} \quad (2.12)$$

If both $V_{RF}$ and $V_{LO}$ are small signals, (2.12) can be approximated as

$$V_{out} = k_n'\sqrt{2\left(\frac{W_1}{L_1}\right)\left(\frac{W_3}{L_3}\right)}R \cdot V_{LO}V_{RF} \quad (2.13)$$

This VGA topology has the advantages of wide bandwidth, stable bandwidth at different gain settings, and stable output common mode level. There are two drawbacks. First, the voltage gain has two polarities, which poses design challenge for the gain control circuit. Second, this architecture consumes more voltage headroom due to transistor

cascading. These two problems were solved by modifying the Gilbert cell to a folded structure and adding an offset tail current to one of the input differential pair [20].

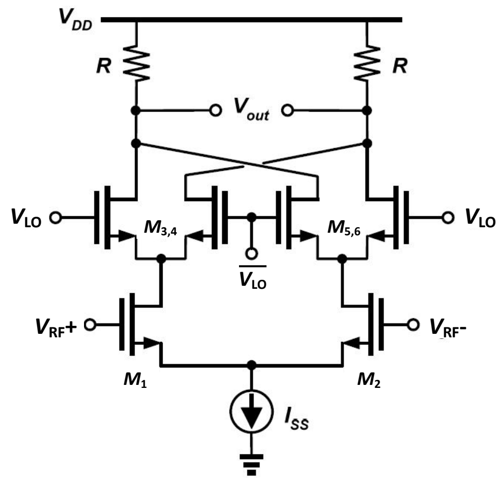


**Figure 2.11**: Gilbert cell based variable gain amplifier

The folded Gilbert cell VGA in [20] achieved a 2GHz bandwidth and a 50dB linear-in-magnitude gain tuning range and showed a constant bandwidth at different gain settings (Figure 2.12). Another ISSCC paper in 2006 [21] further improved this Gilbert cell VGA by adding an exponential voltage generator to create a linear-in-dB gain control and using inductive peaking to extend the bandwidth to 10GHz.

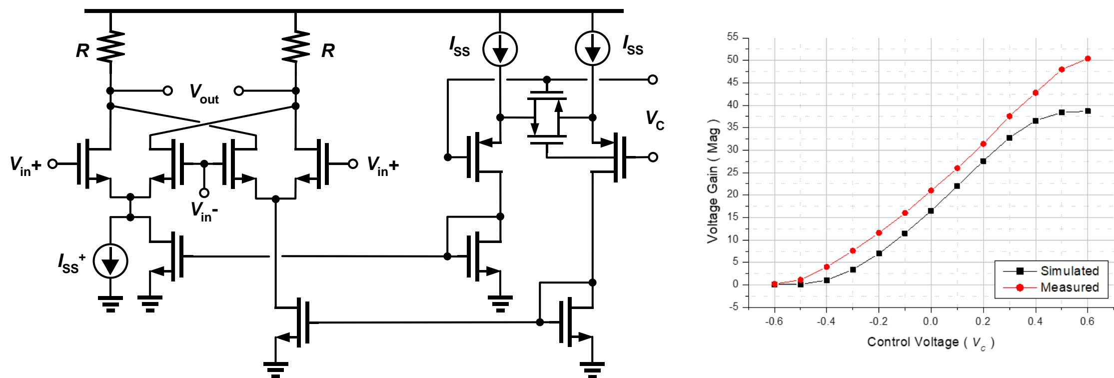


**Figure 2.12**: The 2GHz bandwidth, folded Gilbert cell VGA in [20]

For discrete implementation, VCA810, VCA2613, LMH6502, AD8338, AD8336, and AD605 are good choices for commercial off-the-shelf VGAs.

### 2.2.3 Amplitude Detector

The amplitude detector is an essential component in an ALC loop, it extracts the amplitude of the oscillator output. Non-coherent detection is often employed in an ALC circuit and can be either an absolute value detector or an envelope detector. Diode based amplitude detector is the most common/popular design, the diode acts like a one-way valve that allows the current to flow through it in only one direction. Two typical diode-based amplitude detectors are depicted in Figure 2.13(a). The combination of an opamp and a diode in the bottom of Figure 2.13(a) forms a "super diode", which can eliminate the effect of the diode's turn-on threshold voltage.

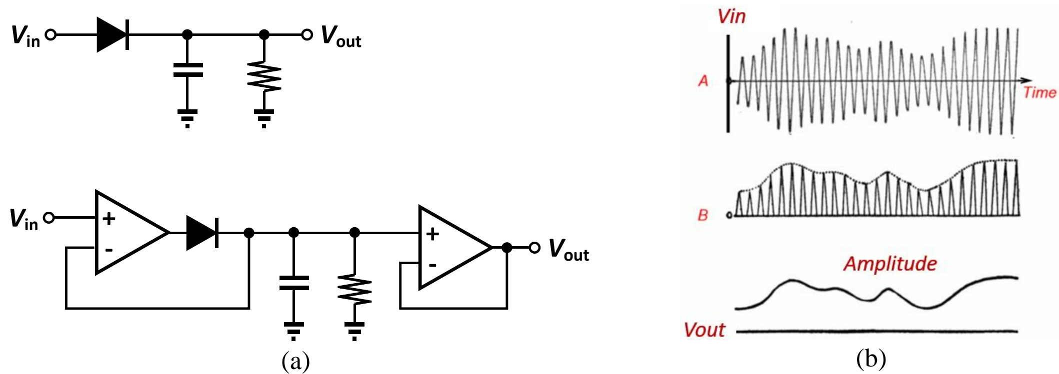


**Figure 2.13**: (a) Typical diode-based amplitude detectors; (b) The input and output waveform of a diode-based amplitude detector

For discrete implementation, LTC1968 is a high accuracy rms-to-dc converter, it can detect small signal down to 5mVrms and has a very linear input-output transfer function. AD8361 and LTC5507 are good choices for high frequency applications up to GHz range.

### 2.2.4 Phase Shifter

A phase shifter provides a phase shift determined by its circuit parameters (ex: $R$ and $C$) at the target frequency. In general, any circuit with pole(s) or zero(s) near the frequency of interest can be used as a phase shifter. However, if we use a simple LPF or HPF as phase shifter, the gain changes as well. A preferred phase shifter characteristic should have a constant gain across a wide frequency range despite the phase change. In an oscillator loop, the phase shifter can compensate the unwanted phase shift generated by the sustaining amplifiers to make sure the Barkhausen phase criterion is satisfied at the resonance frequency. Phase shofter is especially useful for a high-frequency MEMS oscillator because the TIA and VGA will inevitably introduce significant phase shift due to finite bandwidth. It is possible to reduce the phase shift to a negligible value by making the bandwidth of amplifiers much higher (ex: 100X) than the resonance frequency. However, this method will increase the power consumption significantly, which is very inefficient.

It is also important for the sustaining amplifier chain to have an accurate 180° or 360° total phase shift. If the phase shift is inaccurate, sometimes the oscillator can still work but will lock into a frequency slightly different from the resonance frequency ($f_{osc} \neq f_{res}$). The phase noise performance can degrade a lot if the frequency deviation is too large. This phenomenon will be demonstrated with a simulation in the appendix.

Figure 2.14 shows the schematic and frequency response of a typical passive phase shifter. The phase shift at the frequency $\omega = 1/(RC)$ equals to -90°. The implementation is very simple and consumes no dc power; however, it does not have driving capability and requires a differential input for the following stage.

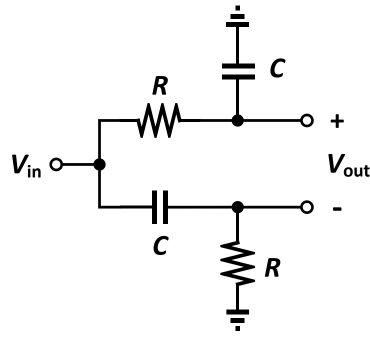


$$\frac{V_{out}}{V_{in}}(s) = \left(\frac{1 - sRC}{1 + sRC}\right)$$

(a)

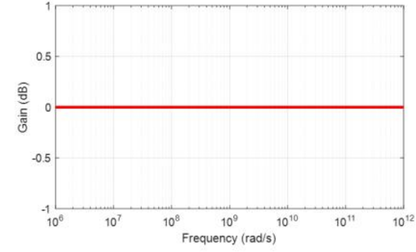


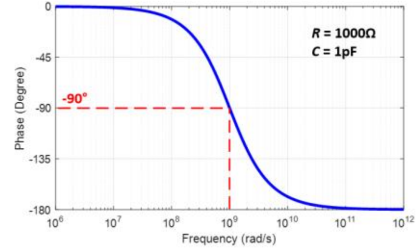


(b)

**Figure 2.14**: (a) Typical passive phase shifter and its transfer function; (b) The simulated gain and phase frequency response. The phase shift at the frequency $\omega = 1/(RC)$ equals to -90°.

Two types of active phase shifters with similar implementation are shown in Figure 2.15, their phase shifts differentiate by 180° if using the same RC values. These phase shifters can provide driving capability as well as voltage gain. The phase shift value is determined by $R_2$ and $C_2$, which can be tunable by using variable resistors (potentiometers) and variable capacitors. The phase shift generated by these two types of phase shifters can be calculated as follow.

$$Type - 1: \quad \Delta\Phi = -2\tan^{-1}(\omega R_2 C_2) \quad \text{rad/s} \tag{2.14}$$

$$Type - 2: \quad \Delta\Phi = +2\tan^{-1}(\omega R_2 C_2) \quad \text{rad/s} \tag{2.15}$$

For discrete implementation, the 3214W series and PVG3 series from Bourns Inc. are good choices for potentiometers, which have available resistance range from 10Ω to 2MΩ. For commercial variable capacitors, the TZY2 series from Murata and the JR series from Knowles Voltronics are good choices with capacitance range from 0.3pF to 3nF available.

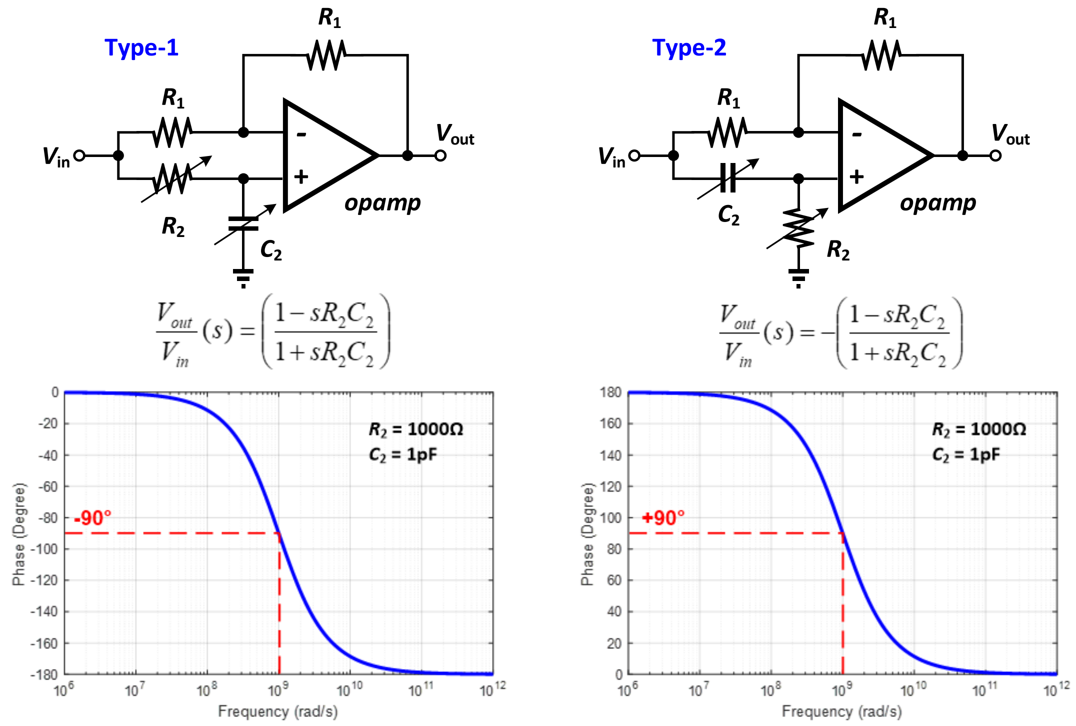


**Figure 2.15**: (Left) Type-1 active phase shifter, and (right) Type-2 active phase shifter

At last, the more detailed MEMS oscillator implementation with discrete electronics will be introduced in chapter 5.

# CHAPTER 3

# A MEMS OCXO USING STRUCTURAL RESISTANCE-BASED TEMPERATURE SENSING

In this chapter, the implementation and measurement results of a silicon MEMS OCXO are presented. Ovenization has been used to provide temperature and frequency control in quartz crystal oven-controlled oscillators (OCXO) to achieve the highest precision acoustic resonator-based oscillators available today. However, it has been challenging to integrate the heater with a quartz resonator on the same die, and hence reducing the ovenization power requires more design effort. On the contrary, silicon MEMS resonators have the advantage of integration in as much as the resonator, heater, and temperature sensors can be integrated on the same die to reduce power consumption as well as the overall size and cost of the system. For example, our group has demonstrated an integrated ovenization technique for a 100-MHz MEMS SiBAR oscillator [22] in which the resistive body of a rectangular silicon bar resonator was used as a heater to self-ovenize the high-*Q* bulk-acoustic wave (BAW) resonator. In addition to integration possibilities, silicon resonators exhibit the other temperature-sensitive characteristics of a semiconductor, which quartz crystal resonators may not possess. The temperature coefficient of resistance (TCR) of the resonator's structural resistance is a good example. Other self-temperature sensing approaches include quality factor *Q*(T)-based [23] and dual (or beat) frequency-based techniques [24].

This research explores the use of the structural (electrical) resistance of a silicon resonator for self-temperature sensing in an integrated all-silicon MEMS OCXO. Such an embedded thermistor not only shows large temperature sensitivity but also nearly zero hystereses in cooling and heating cycles. While such a concept was previously

demonstrated in the instrumental level [25, 26], here we present the complete implementation of a temperature-compensated frequency-reference oscillator with both discrete and CMOS integrated electronics. The silicon MEMS resonator is wafer-level and vacuum packaged. My colleague Roozbeh Tabrizian designed the MEMS resonator of this work.

### 3.1 Silicon MEMS OCXO System

The active compensation system based on structural resistance temperature sensing is explained in Figure 3.1. The system consists of a main oscillator, a resistance temperature detector (RTD), a low-pass loop filter $H(s)$, and a heater amplifier for the micro-oven. The resonator and a resistive heating element sit next to each other on the same die. The resistive element is used as the micro-oven heater (with voltage applied across its body). The silicon MEMS resonator is designed to have a high-frequency BAW resonant mode and a measurable structural resistance ($R_{Struc}$). The RTD circuit extracts the resonator temperature information, i.e., its structural resistance, compares it with a reference resistor ($R_{REF}$), and then generates a resistance error signal to the low-pass loop filter, $H(s)$.

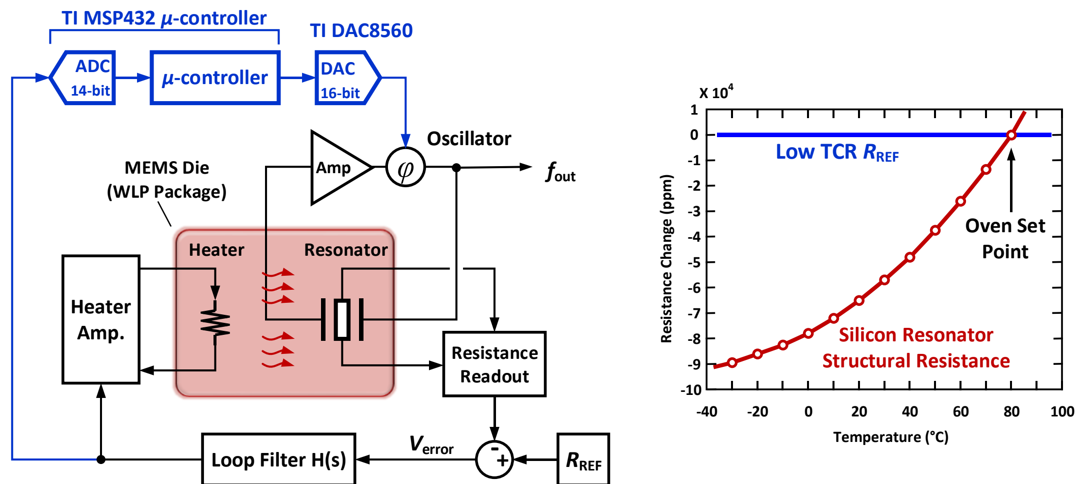


**Figure 3.1**: System block diagram of the silicon MEMS OCXO (left); and determination of the oven set-point by the TCR intersection of $R_{REF}$ and $R_{Struc}$ (right)

The main objective of the loop filter is to provide a high gain to suppress the resistance error and lock the $R_{\mathrm{Struc}}$ value to the oven set-point value with minimum temperature deviation. The micro-oven adjacent to the main resonator is controlled by this feedback loop automatically and, hence, achieves an active temperature stabilization. A digital feedforward calibration path is added to further reduce the residual frequency error by fine-tuning the phase shift of the oscillator's sustaining amplifier. This will be discussed in detail in Section 3.3.

Several benefits exist for the resistance-based sensing and control scheme. First, the resistive characteristic is extracted from the same resonator used for oscillator, so it represents the true temperature of the device. When compared with an external thermistor, the resistance-based sensing and control scheme exhibits little or no thermal lag. Second, the structural resistance shows a large temperature sensitivity (local TCR > 1500 ppm/°C) at around 90°C, which makes it suitable for an embedded temperature sensor in an ovenized platform. Third, resistance can be easily measured accurately with modern circuit techniques, and the readout circuit can operate at a much lower frequency than the main oscillator can. This "quiet" background operation will only cause imperceptible crosstalk or mutual interference compared to the dual frequency-based temperature sensing method [24]. This further benefits higher frequency (gigahertz) oscillators.

### 3.2 Silicon MEMS Resonator Design

A waveguide-based silicon acoustic cavity is designed and implemented to operate in a purely shear Lamé mode at 77.7 MHz. The waveguide has a rectangular cross-section and is carefully designed to trap the acoustic energy of an eigenmode with Lamé cross-sectional polarization in the central region of a microstructure [27]. Figure 3.2(a) shows

the resonator geometry as well as its mode shape. Proper design considerations guarantee the excitation of evanescent waves in the flank regions of the microstructure, providing an exponential decay in energy density toward the two end anchors. Such an energy distribution obviates the need for narrow tethers conventionally used for low-loss suspension of the acoustic cavity [28]. This narrow tether structure is essential for a cross-sectional Lamé-mode that lacks a nodal line for nondestructive energy suspension. Furthermore, such a design facilitates implementation of Lamé-mode devices with much smaller form factors and operating at higher frequencies compared to conventional planar square Lamé resonators. Figure 3.2(b) shows the actual layout of the 4-mm$^2$ MEMS die with two identical resonators. The upper right resonator is used as the micro-oven (heater). The four pads adjacent to the sense and drive electrodes are all connected to a top polysilicon electrode, which is not used here. The detailed dimensions of the resonator are illustrated in Figure 3.2(c).

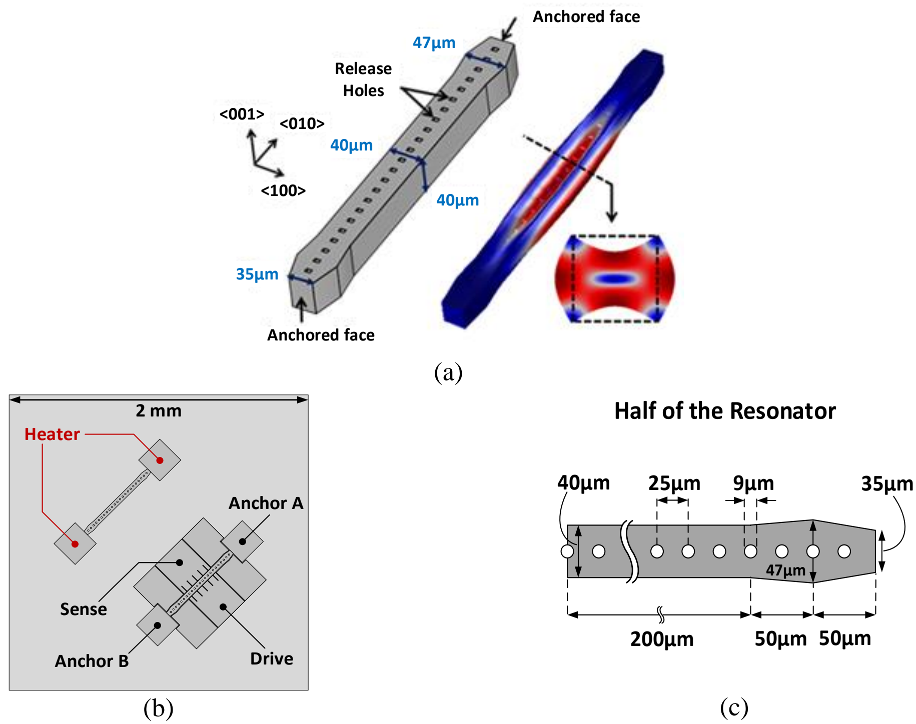


**Figure 3.2:** (a) Cross-sectional Lamé-mode resonator geometry and mode shape, (b) layout of the 4mm$^2$ MEMS die, and (c) detail dimensions of the resonator

Figure 3.3(a) and 3.3(b) show the SEM images of the 77.7-MHz device implemented using the high aspect-ratio combined poly- and single-crystal silicon (HARPSS) process and the wafer-level packaged die, respectively. In Figure 3.3(a), the cross-sectional view of the resonator structure along the red dashed line is drawn in Figure 3.3(c). A close-up SEM image of the HARPSS nanogap is highlighted here. The frequency response of the resonator in Figure 3.4(a) shows a high-$Q$ of ~40,000. The temperature characteristic of the resonant frequency is measured from −30 °C to 90 °C in Figure 3.4(b). The curve shows the first-order TCF of −25.3 ppm/°C and the second-order TCF of −38.9 ppb/°C$^2$. The structural resistance of the MEMS resonator is measured across its two terminals, A and B, as shown in Figure 3.3(a), from −30 °C to 90 °C.

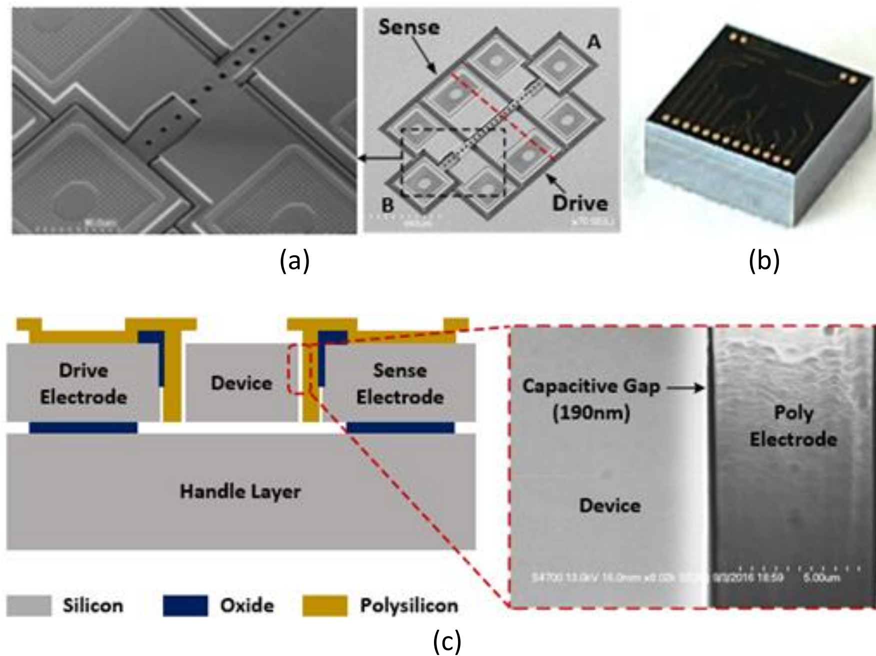


**Figure 3.3:** (a) SEM images, (b) optical image of a wafer-level packaged cross-sectional Lamé resonator fabricated by Qualtré Inc. (now Panasonic), and (c) cross-sectional view of the resonator along the red line in (a) and the SEM of the HARPSS nanogap

The $R_{Struc}$-$T$ characteristic is shown in Figure 3.4(c). The TCR exhibits a significant second-order behavior and has an average value of ~760 ppm/°C. The derivative of the curve (hereinafter "local TCR") increases with temperature and reaches 1560 ppm/°C at 90 °C. The high TCR at the target oven set-point makes it suitable to accurately and locally monitor the resonator temperature for ovenization application.

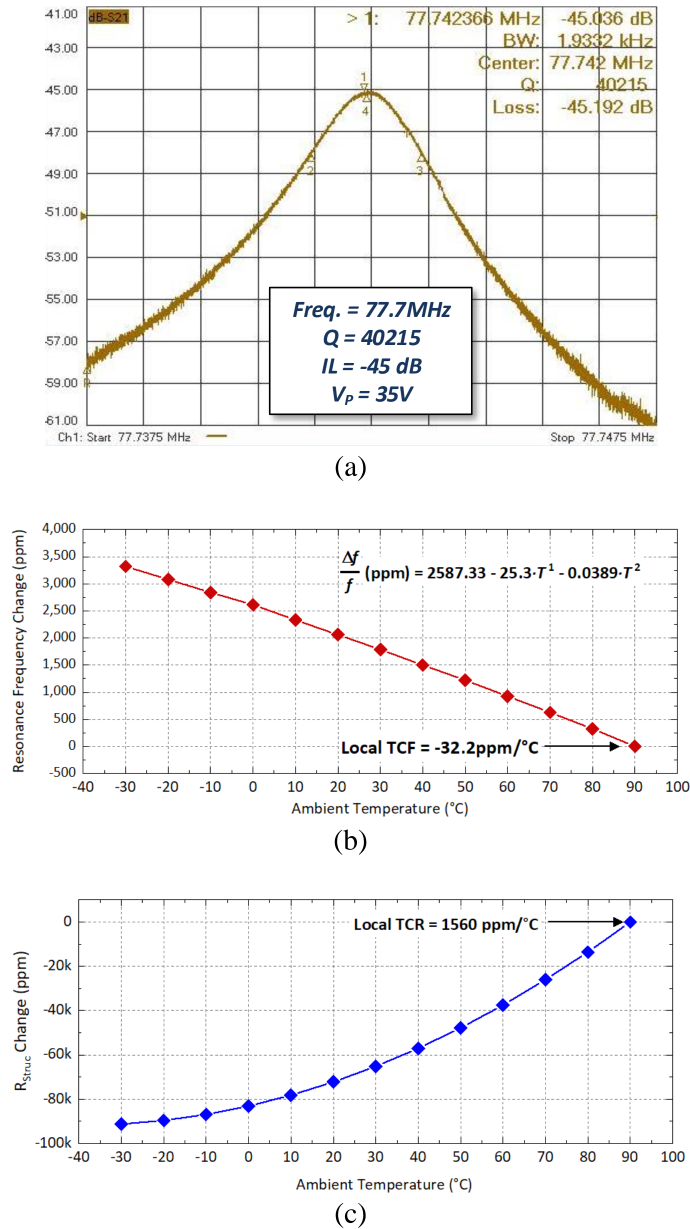


**Figure 3.4:** (a) Measured S21 of the cross-sectional Lamé-mode resonator, (b) measured temperature characteristic of the resonant frequency, and (c) measured temperature characteristic of the resonator structural resistance

## 3.3 Oscillator Circuit Design

### 3.3.1 CMOS Oscillator Circuit

The oscillator sustaining amplifier is implemented as an application-specified integrated circuit (ASIC) in the Taiwan Semiconductor Manufacturing Company (TSMC) 0.35-µm CMOS process (Figure 3.5a). The differential amplifier structure is employed to have better supply noise rejection and to enable the high-frequency feedthrough cancellation function. The feedthrough capacitance of the resonator from drive electrode to sense electrode is about 0.5 pF and needs to be eliminated so the oscillator can function correctly. Since the operating frequency is high, the feedthrough cancellation requiring an auxiliary amplifier is not preferred [29]. The auxiliary amplifier generates a significant phase shift to the inverted drive signal and would not cancel the feedthrough signal completely. As shown in Figure 3.5(a), a new method that makes use of the other output of the amplifier to feed an on-chip tunable PMOS capacitor array to achieve a zero-delay feedthrough cancellation path.

The on-chip tunable PMOS capacitor array can be digitally controlled by switches for coarse tuning. It can also be controlled in an analog manner for fine tuning by adjusting the bulk bias voltage of the PMOS transistor. Figure 3.5(b) shows the detailed transimpedance amplifier (TIA) schematic. Because both the drive and sense electrodes have large shunt parasitic capacitance of about 6 pF, a regulated cascode input stage is designed to create a low input resistance (<10) to minimize the shunt parasitic capacitance impact on the overall bandwidth. The second stage of TIA utilizes the current injection technique to increase the voltage gain. It also has a tunable gain-peaking function. The gain-peaking function is to extend the amplifier bandwidth and can be tuned to overcome

process variation for the best frequency response. The second stage of the TIA provides a voltage gain of about −4 V/V.

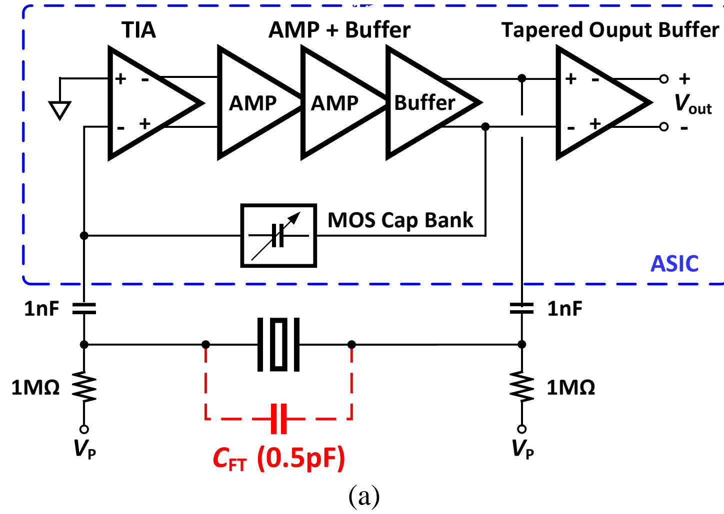


(a)

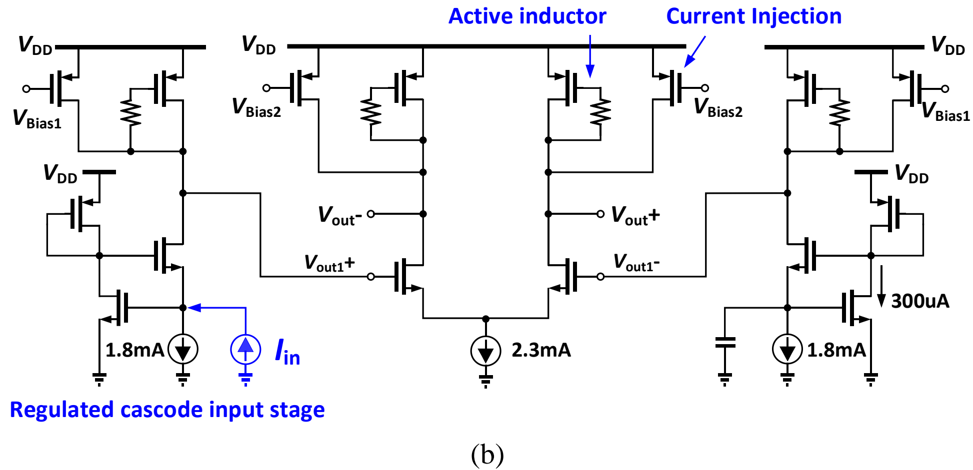


(b)

**Figure 3.5:** (a) Sustaining amplifier and the high-frequency $C_{FT}$ cancellation circuit, (b) detailed TIA schematic

### 3.3.2 Closed-Loop Oven Control

Figure 3.6 shows the detailed schematic of the proposed active oven control loop implemented with off-the-shelf components. The reference resistor ($R_{REF}$) is formed by a

combination of low TCR thin film surface-mount resistors to achieve a total resistance equal to four times of the resonator structural resistance at the target oven temperature (90 °C). The $R_{\mathrm{REF}}$ exhibits a total resistance drift of 50 ppm across the operating temperature range of -25°C - 85°C. The effect of $R_{\mathrm{REF}}$ drift on the frequency stability of the system is weakened by the resonator body resistance TCR at the target oven temperature (~1560 ppm/°C). As described by the following equation, when resonator TCF equals −32.3 ppm/°C (local TCF at 90 °C), the resulting effect is about 1 ppm:

$$\frac{R_{REF}\ Drift}{R_{struc}\ TCR@72°\mathrm{C}} \times (Resonator\ TCF) = \frac{40(ppm)}{1400\left(\frac{\mathrm{ppm}}{°\mathrm{C}}\right)} \times 27.3\left(\frac{ppm}{°\mathrm{C}}\right) = 0.78\mathrm{ppm} \tag{3.1}$$

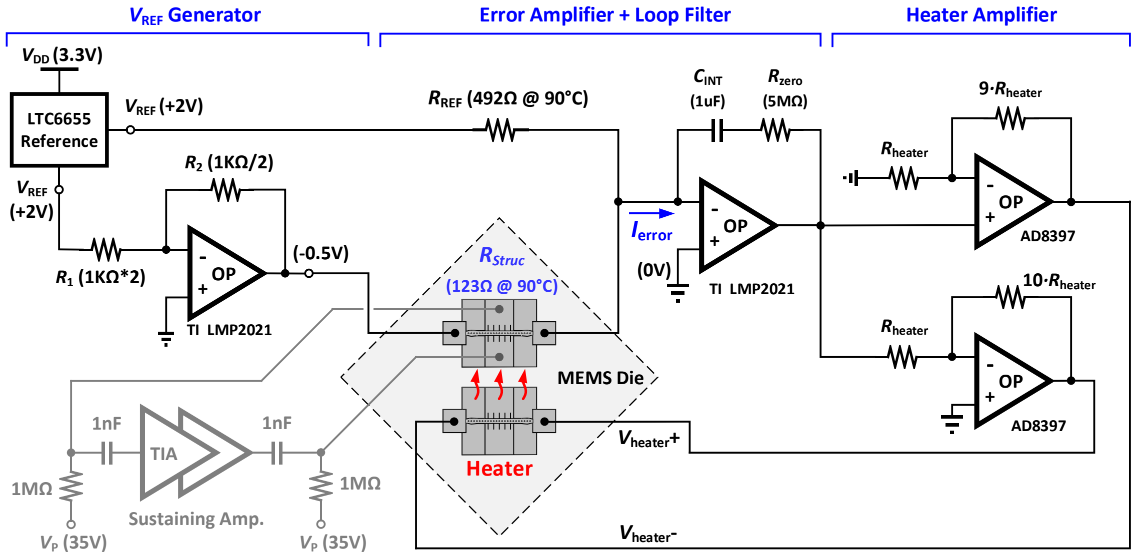


**Figure 3.6:** Schematic of the active oven control loop. The simplified oscillator circuitry is shown in gray color.

To compare the resistances of $R_{\mathrm{REF}}$ and $R_{\mathrm{Struc}}$, we apply −0.5V and +2V reference voltages to $R_{\mathrm{Struc}}$ and $R_{\mathrm{REF}}$, respectively. An error current ($I_{\mathrm{error}}$) is then produced:

$$I_{error} = 2 \times R_{REF} - 0.5 \times R_{Struc} \quad (3.2)$$

$I_{error}$ is set to zero at the oven set-point (90 °C). When the ambient temperature deviates from the target oven temperature, a finite $I_{error}$ is generated and integrated by the integrator.

The integrator op-amp (TI LMP2021) is carefully chosen to have a very small input offset voltage drift (<0.02 μV/°C). It only contributes a 0.5-ppm frequency variation to the overall system. Two high-voltage, high-output-current op-amps (AD8397) are used as the heater amplifiers. The heater amplifiers take in the integrator output and generate feedback voltages ($+V_{heater}$ and $-V_{heater}$) to set the oven temperature to target (90 °C), bringing $I_{error}$ back to nearly zero. Although the 2-V voltage reference (LTC6655) has a 2-ppm/°C drift, it appears as a "common-mode" error to both the $R_{REF}$ and $R_{Struc}$ current paths. This drift is greatly suppressed by the matching between $R_{REF}$ and $R_{Struc}$; and, hence, would have an insignificant effect on the overall frequency stability.

Figure 3.7 shows the control model of the closed-loop system. We begin by modeling the current comparator as a subtraction element (subtracts the current of $R_{Struc}$ from that of $R_{REF}$) with gain $K_{LP}$. The loop filter is a simple opamp integration stage. By placing a resistor in series with the integrator feedback capacitor, we added a zero to the integrator transfer function to ensure maximum phase margin for the overall system. Because the heater amplifier bandwidth is much larger than the overall system bandwidth, the gain of heater amplifier is lumped with the gain of the integrator stage ($K_{LP}$). Next, the micro-oven is modeled as a first-order system that converts voltage to temperature with a 3-dB bandwidth of about 0.02 Hz and a gain computed from measuring the $V_{heater}$–$R_{Struc}$ curve. Finally, we model the structural resistance of the resonator as a temperature-controlled resistor whose output is $R_{Struc}(T)$. Because the control loop keeps the oven temperature almost constant, the gain of the temperature-controlled resistor ($K_{TCR}$) is assumed to be a

simple constant that is the derivative of the $R_{\mathrm{Struc}}$-$T$ curve in Figure 3.4(c) at the oven set-point. Note that $R_{\mathrm{REF}}$ is treated as a constant input to the system because its sensitivity to temperature is almost 1600× smaller than that of $R_{\mathrm{Struc}}$. Because the system has two poles, the locations of the electrical pole of the loop filter ($\omega_{p1}$) and the zero of the integration stage ($\omega_z$) determine the system phase margin and stability. Using this model in Figure 3.7(b), we plot the computed closed-loop frequency response of the oven control circuit. The control system achieves a unity-gain crossover frequency of about 20 Hz.

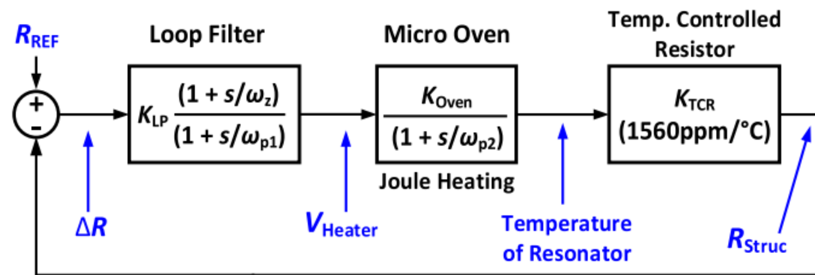


(a)

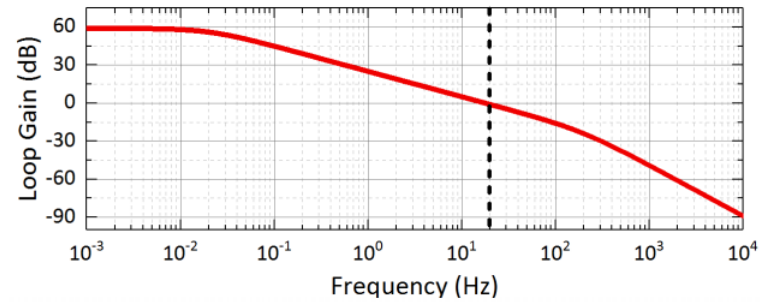


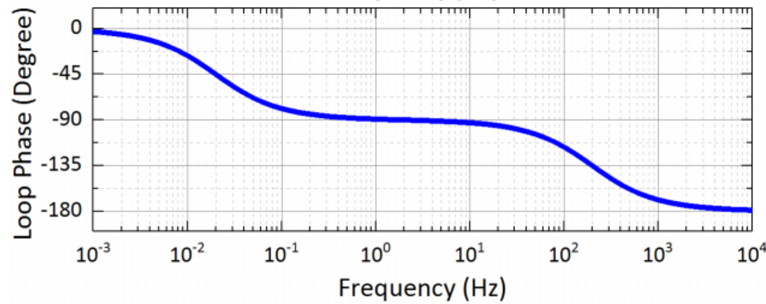


(b)

**Figure 3.7:** (a) Closed-loop model of the oven control circuit. (b) Gain and phase frequency response of the control system. The control system achieves a unity-gain crossover frequency of about 20 Hz

### 3.3.3 Feedforward Digital Calibration

The digital feedforward calibration is used to further reduce the residue frequency drift due to the temperature sensing error, the temperature-induced phase shift of the sustaining amplifier, and the temperature-induced oscillation amplitude variation. The temperature sensing error causes a finite temperature variation inside the micro-oven, which results in frequency drift. The temperature-induced phase shift of the sustaining amplifier forces the MEMS resonator to operate at a frequency slightly off the nominal resonant frequency $f_0$. The temperature-induced oscillation amplitude variation can slightly change the frequency via the A–$f$ effect [24].

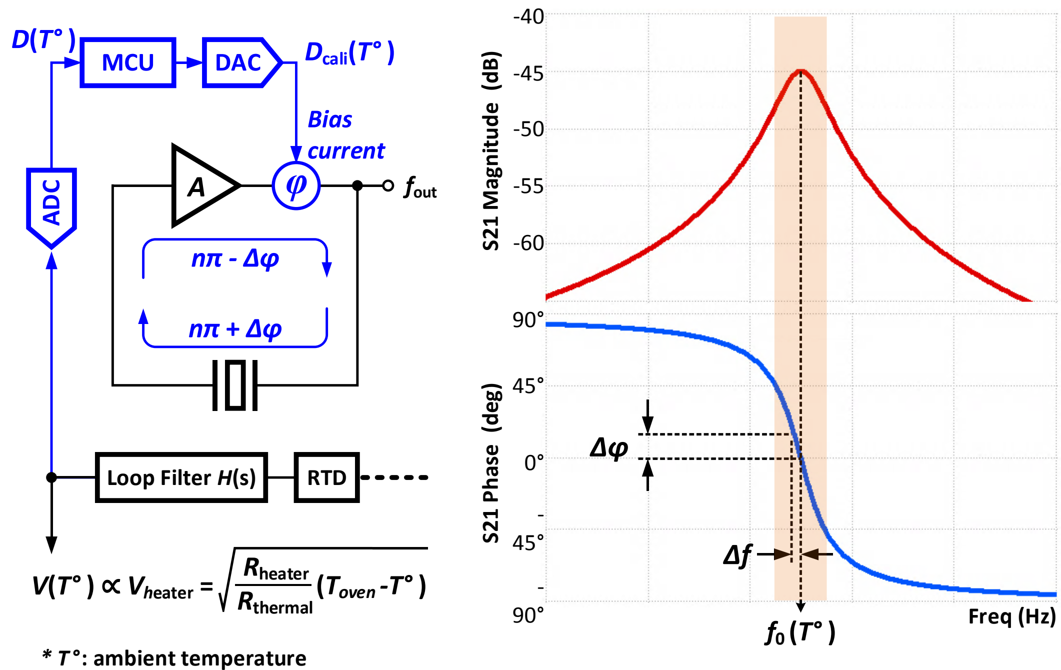


**Figure 3.8:** Operating principle of the feedforward calibration

As shown in Figure 3.8, the output of the loop filter that represents the temperature information is first digitized by a 14-bit analog-to-digital converter (ADC) embedded in

the microcontroller (TI MSP432). The digital data is then processed by a fourth order polynomial curve fitting and then converted to a predefined set of codes that can minimize the oscillator frequency drift. The digital output of the microcontroller is then converted to an analog voltage by a digital-to-analog converter (DAC, TI DAC8560) and fed to the phase-tuning mechanism inside the oscillator loop for fine-frequency tuning. If both ADC and DAC have $N$-bit resolution, theoretically this method can reduce the residue frequency error by a factor of $2^N$.

Notice that any parameter capable of tuning the oscillator frequency by a few parts per million could be used for this calibration, such as polarization voltage ($V_P$), TIA phase response, and A–$f$ effect. In this work, the master bias current of the sustaining amplifier is chosen as the amplifier phase-tuning mechanism. Compared to the feedback digital calibration in [24], the main advantage of our feedforward digital calibration scheme is that it does not interfere with the temperature sensor's operation. Therefore, the frequency stability can be improved not only under steady-state temperatures but also under dynamically changing ambient temperatures.

## 3.4 Measurement Results

### 3.4.1 Implementation

Figure 3.9 shows the photograph of the prototype printed circuit board (PCB) and the ASIC die of the entire temperature compensation system. The resonators, oscillator electronics, and microcontroller were implemented at the board level and experienced the same ambient temperature change in an ESPEC SH-240 benchtop temperature chamber.

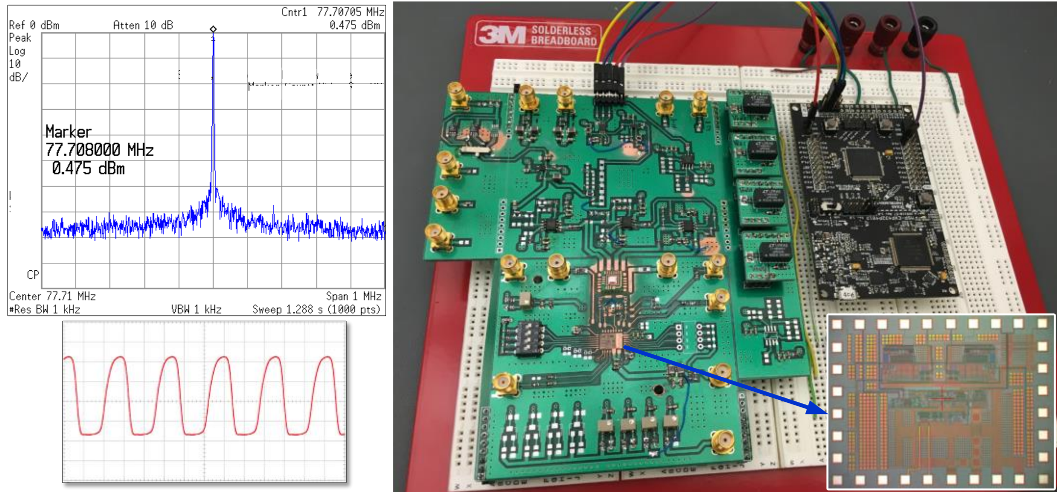


**Figure 3.9:** (Left) Oscillator output spectrum and transient waveform; (right) Photographs of the prototype PCB and the ASIC die

### 3.4.2 Frequency Stability

The oscillating frequency of the MEMS OCXO is 77.7 MHz. Figure 3.10(a) shows the measured steady-state frequency stability across the temperature range from −25°C to +85°C. Without any compensation, the intrinsic frequency drift of the MEMS resonator is about 3000 ppm. When the analog micro-oven control loop is enabled, the frequency drift is greatly reduced to ±2.5 ppm (600 times improvement). The residual frequency error shows an approximately linear relationship with the temperature. This error is due to the asymmetric heater arrangement and the parasitic resistance in series with $R_{\text{struc}}$. The asymmetric heater arrangement can cause a temperature gradient on the resonator body. It shifts the $R_{\text{struc}}$– $f_{\text{res}}$ curve slightly and introduces a frequency error [26]. The device is packaged at the wafer level; the interconnections between the resonator body and the pads on the package have small parasitic resistances. The bonding wires and the PCB traces also contribute finite parasitic resistances. These parasitic resistances are made of metals and

usually exhibit large TCRs (e.g., TCR of copper = 3900 ppm/°C). The large TCR of the parasitic resistances can lead to an inaccurate temperature reading in the RTD circuit.

Other error sources may also contribute to the residue frequency variation: 1) temperature-induced sustaining amplifier phase shift, 2) temperature-induced oscillator output amplitude variation, 3) temperature dependence of the feedthrough capacitor, and 4) temperature variation of the $R_{REF}$.

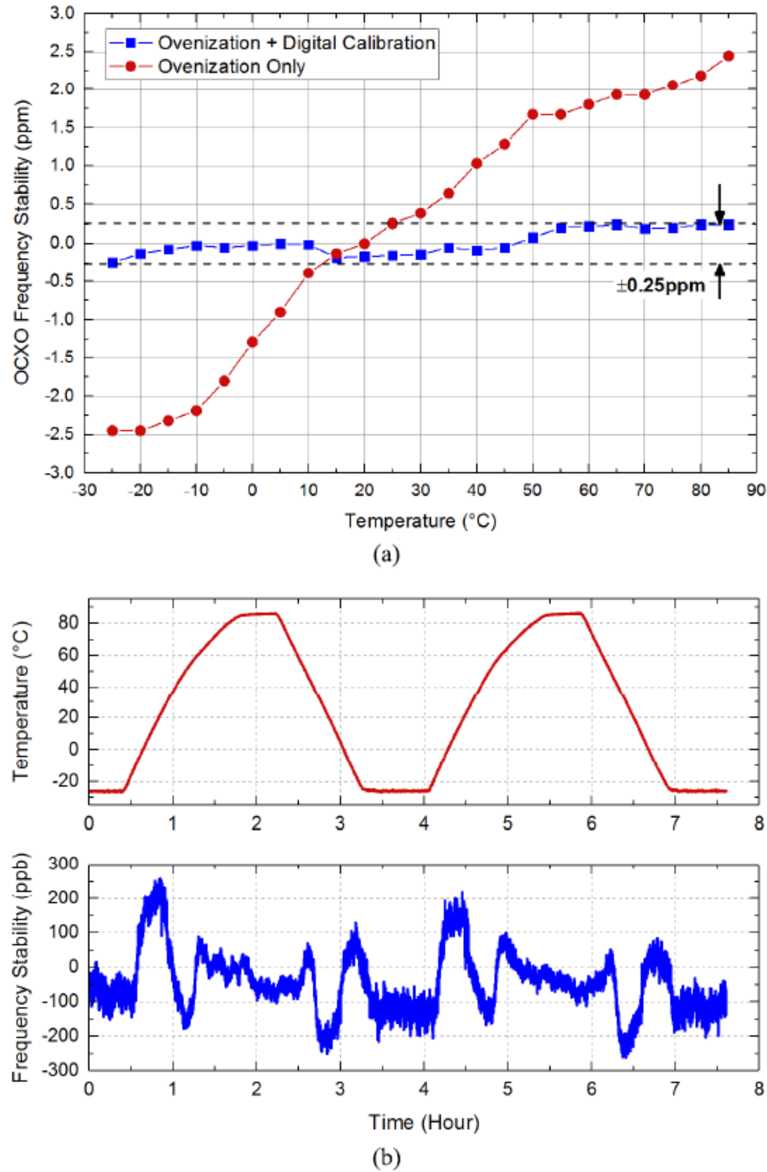


**Figure 3.10:** (a) MEMS OCXO steady-state frequency stability with and without digital calibration, and (b) MEMS OCXO frequency stability under varying temperature with the digital calibration enabled.

After applying the feedforward digital calibration, the frequency stability is further improved by 10 times, down to ±0.25 ppm. Most of the error sources mentioned earlier are greatly reduced by this calibration scheme. The dynamic frequency stability of the MEMS OCXO was also characterized under varying temperature between −25°C and 85°C at a ramp rate of 1.8°C/minute. As shown in Figure 3.10(b), the frequency variation is still

within the ±0.3 ppm range, which is very close to the steady-state frequency stability. This result demonstrates that the proposed digital calibration scheme not only improves the steady-state but also the dynamic temperature frequency stability.

### 3.4.3 Phase Noise

The phase noise of this silicon MEMS OCXO is measured by a Rohde and Schwarz FSWP phase noise analyzer under different ambient temperatures (Figure 3.11). At 30°C, it shows a −100-dBc/Hz phase noise at the 1-kHz frequency offset. At far-from-carrier frequency (1 MHz), the phase noise dropped to −116 dBc/Hz. The high close-in phase noise is mainly due to the flicker noise from the sustaining amplifier ASIC. This result is consistent across a 110°C ambient temperature change.

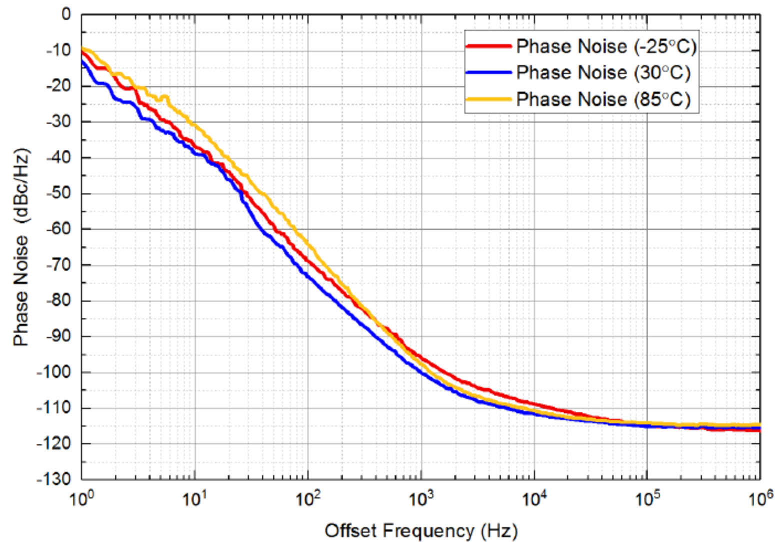


**Figure 3.11:** Measured MEMS OCXO phase noise with oven control loop enabled at the ambient temperatures of −25°C, 30°C, and 85°C. The oscillation frequency is 77.7 MHz.

### 3.4.4 Allan Deviation

Figure 3.12 shows the Allan deviation of this silicon MEMS OCXO. It was measured by a Keysight 53210A frequency counter for 140 hours with the oven-control loop and the

digital calibration both enabled under a constant ambient temperature of 60°C. The sampling period ($\tau_0$) is about 0.4 second. A Connor Winfield OH-300 10-MHz quartz OCXO was used as the frequency reference of 53210A. The ADEV result shows a minimum value of 7.5 ppb between 100 and 1000 second. At approximately 1000 second, the Allan deviation starts to increase due to long-term frequency drift. Aging is one of the possible causes. Further investigation is required to determine the root cause of the frequency drift and to identify ways of reducing it.

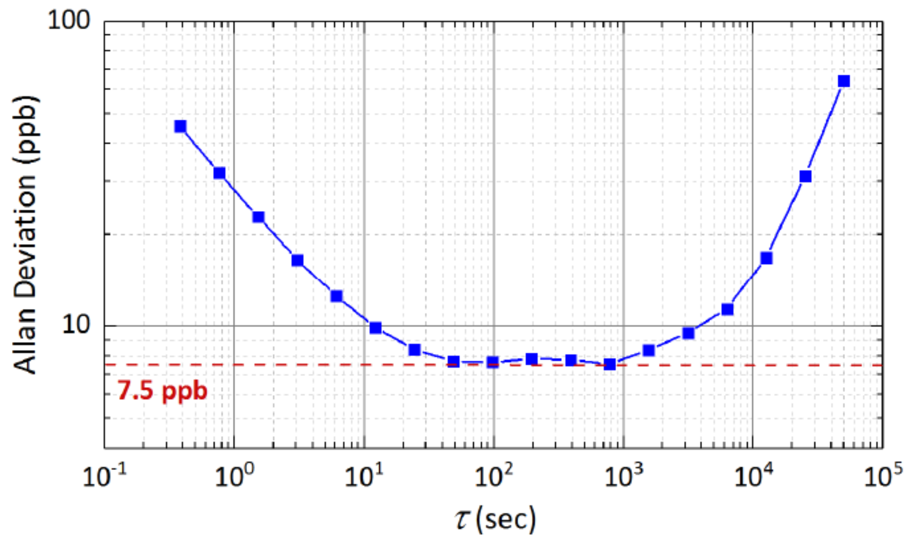


**Figure 3.12:** Measured Allan deviation of the MEMS OCXO with both oven-control loop and digital calibration enabled. The measurement time is about 140 h at 60°C. The sampling period ($\tau_0$) is about 0.4s. The minimum Allan deviation is 7.5 ppb between 100 and 1000s.

### 3.4.5 Power Consumption

The sustaining amplifier ASIC consumes 16 mA from a 3.2V power supply. The differential structure of the sustaining amplifier and the need for a high-gain at 77.7 MHz cause the significant power consumption. The RTD, loop filter, and heater amplifier consume 22mW total power. The measured heating efficiency of the micro-oven is about 0.3°K/mW. It results in a Joule heating power of 383mW at −25°C ambient temperature.

The lowest thermal resistance path is from the $SiO_2$ layer (2μm thick) under the resonator posts ($R_{th} \approx 70$ K/W), through the silicon substrate ($R_{th} \approx 1$ K/W), then to the PCB. A better micro-oven design with optimized insulation geometry to minimize power consumption can further reduce the Joule heating power [30].

## 3.5 Conclusion and Discussion

We have demonstrated a micro-ovenized silicon MEMS oscillator operating at 77.7MHz and achieving a frequency stability of ±0.3 ppm across the temperature range of −25°C – +85°C. The oscillator relies on real-time monitoring structural resistance of the resonator and an automatic closed-loop control to regulate the temperature of the micro-oven. A novel high-$Q$ cross-sectional Lamé-mode resonator was used in this MEMS OCXO. The board level prototype achieves an approximate 5,000 times improvement in the frequency stability.

Table 3-1 summarizes the performance of this MEMS OCXO and compares it with state-of-the-art MEMS OCXO research efforts. With the help of digital calibration, this work achieves the highest frequency stability improvement factor ever reported.

$$Frequency\ Stability\ Improvement\ Factor = \frac{MEMS\ resonator\ frequency\ drift}{\text{OCXO frequency stability}} \tag{3.3}$$

The micro-oven power consumption is high but can be improved in the next generation design. In the future, with a TCF-compensated resonator and a more accurate temperature sensor design, the frequency stability can be further improved. The performance potentially can be comparable with the quartz crystal OCXOs.

Table 3-1
MEMS OCXO Performance Summary and Comparison

| | | 2006 Krishna | 2010 Salvia | 2012 Tazzoli | 2015 Chen | 2015 Wu | 2015 Wojciechowski | 2016 Chen | 2017 Koo | **This Work** |
|---|---|---|---|---|---|---|---|---|---|---|
| $f_0$ (MHz) | | 103 | 1.2 | 582 | 10 | 19.2 | 15 | 10.7 | 756 | **77.7** |
| Temp. Sensing | | Thermistor | $\Delta$-$f$ | Thermistor | $R_{Struc}$ | $\Delta$-$f$ | Thermistor | $\Delta$-$f$ | Thermistor | **$R_{Struc}$** |
| Temp. Range (°C) | | 100°C (25 – 125) | 100°C (-20 – 80) | 130°C (-45 – 85) | 120°C (-40 – 80) | 100°C (-40 – 70) | 125°C (-40 – 85) | 100°C (-20 – 80) | 85°C (-5 – 80) | **110°C (-25 – 85)** |
| MEMS Freq. Drift (ppm) | | 2980 | 1500 | 3640 | 300 | 3300 | 234 | 1800 | 300 | **3000** |
| OCXO Freq. Stability (ppm) | | 56 | 2 | 125 | 4 | 8 | 0.35 | 0.5 | 3.1 | **0.6** |
| Freq. Stability Improvement Factor | | 53 | 750 | 29 | 75 | 413 | 669 | 3600 | 97 | **5000** |
| Power Cons. @ 25°C (mW) | μ-heater | 170 | 10 | 6.5 | 70 | 3.8 | 5.8 | 400 | 9 | **216.5** |
| | Others | 22 | 127 | -- | -- | 15.6 | 25.3 | -- | 2.9 | **74** |


ACKNOWLEDGMENT

I would like to thank Qualtré Inc. (now Panasonic) for the MEMS resonator fabrication and packaging. I would also like to thank Mr. Albert Lu for microcontroller technical support and Rohde and Schwarz Inc. for providing a FSWP phase noise analyzer.

# CHAPTER 4

# MEMS CORIOLIS VIBRATORY GYROSCOPES

Gyroscopes based on microelectromechanical systems (MEMS) are micro-scale inertial sensors that measure the rotation of an object without relying on external references. This chapter will introduce the basic operational principle and performance metrics of silicon MEMS vibratory gyroscopes. MEMS vibratory gyroscopes are an extended application of MEMS resonators, which also suffer from the challenge of *temperature-induced frequency drift* as the MEMS resonators. The temperature change can cause scale factor and output bias variations. We will address this problem for the gyroscopes in Chapter 5.

## 4.1 MEMS Coriolis Vibratory Gyroscopes (CVG)

Inertial measurement units (IMUs) consisting of 3-axis gyroscopes and 3-axis accelerometers have been successfully deployed in a variety of industrial and aerospace applications over the past few decades to provide high precision motion sensing and navigation [31, 32]. With the advances in micromachining technology, the miniaturized inertial sensors were used for a wide array of low-accuracy and low-power consumer and automotive applications such as image stabilization for digital cameras, motion sensing for gaming consoles, anti-skid control, and airbag deployment in automobiles.

Different applications require different performance levels for the inertial measurement system. Table 4-1 summarizes the performance grades for gyroscopes [33]. Rate grade, tactical grade, and inertial grade performances are used in consumer applications, industrial and automotive applications, and navigation applications,

respectively. While consumer applications require relatively relaxed noise, accuracy and stability performance, navigation applications typically have stringent requirements for noise, accuracy, and overall performance stability, to provide precision positioning.

**Table 4-1**: Performance grades of gyroscopes [33]

| Parameter | Rate Grade | Tactical Grade | Inertial Grade |
| --- | --- | --- | --- |
| Bias drift | 10 to 1000 °/hr | 0.01 to 10 °/hr | < 0.01 °/hr |
| Angle random walk | > 0.5 °/√hr | 0.5 - 0.05 °/√hr | < 0.001 °/√hr |
| Scale factor accuracy | 0.1 - 1% | 100 – 1000 ppm | < 10 ppm |
| Full scale range | 50 - 1000 °/sec | > 500 °/sec | > 400 °/sec |
| Bandwidth | > 70 Hz | ~100 Hz | ~100 Hz |

### 4.1.1 Principle of Operation

Vibratory gyroscopes operate based on the Coriolis effect, which is the energy transfer between two orthogonal resonance modes of a device as a result of an out-of-plane rotation [34]. Figure 4.1 shows the operation of a tuning-fork gyroscope based on Coriolis energy transfer. The primary resonance mode is actuated along the *x*-axis, and a rotation around the *z*-axis induces Coriolis acceleration along the *y*-axis, moving the fork tines along the *y* direction. Coriolis acceleration can be mathematically expressed as

$$\vec{a}_{Cor} = 2\vec{v} \times \vec{\Omega}_z \quad (4.1)$$

where $v$ is the velocity of the primary in-plane mode, also called the drive mode, and $\Omega_z$ is the rotation around the out-of-plane axis (*z*-axis). Based on (4.1), the Coriolis acceleration is generated at the same frequency as that of the drive mode but along the secondary in-plane mode, also known as the sense mode. The Coriolis acceleration can generate a larger

displacement along the sense axis if the resonance frequencies of the sense mode and drive mode are matched [35, 36].

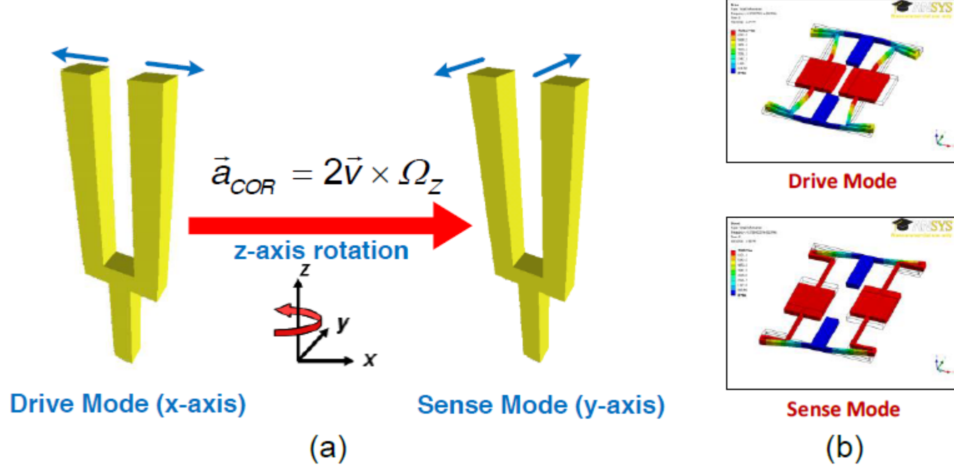


**Figure 4.1**: (a) Coriolis effect in a tuning fork, (b) Tuning-fork gyroscope (TFG) operating based on the Coriolis effect [35]

The mathematical representation of MEMS vibratory gyroscopes operation can be described as follows:

$$\begin{aligned} m\ddot{x} + d_{xx}\dot{x} + k_{xx}x + k_{yx}y + d_{yx}\dot{y} &= f_x(t) - 2m\lambda\Omega_z\dot{y} \\ m\ddot{y} + d_{yy}\dot{y} + k_{yy}y + k_{xy}x + d_{xy}\dot{x} &= f_y(t) + 2m\lambda\Omega_z\dot{x} \end{aligned} \tag{4.2}$$

where $m$ is the mass of the resonator, $d_{ii}$ and $k_{ii}$ terms are the damping and stiffness of the resonance modes along their respective axes, and $d_{xy} = d_{yx}$ and $k_{xy} = k_{yx}$ are the damping and stiffness coupling terms between the two modes [37, 38]. This equation can be represented in the Laplace domain as follows:

$$\begin{bmatrix} s^2 + \frac{\omega_x}{Q_x}s + \omega_x^2 & \omega_{xy}^2 + \frac{\omega_{xy}}{Q_{xy}}s + 2\lambda\Omega_z s \\ \omega_{yx}^2 + \frac{\omega_{yx}}{Q_{yx}}s - 2\lambda\Omega_z s & s^2 + \frac{\omega_y}{Q_y}s + \omega_y^2 \end{bmatrix} \cdot \begin{bmatrix} X(s) \\ Y(s) \end{bmatrix} = \begin{bmatrix} F_x(s)/m \\ F_y(s)/m \end{bmatrix} \tag{4.3}$$

In the above set of equations:

$$\frac{d_{xx}}{m}=\frac{\omega_x}{Q_x},\frac{d_{yy}}{m}=\frac{\omega_y}{Q_y},\ \frac{k_{xx}}{m}=\omega_x^{\ 2},\frac{k_{yy}}{m}=\omega_y^{\ 2}$$
$$\frac{d_{xy}}{m}=\frac{d_{yx}}{m}=\frac{\omega_{xy}}{Q_{xy}}=\frac{\omega_{yx}}{Q_{yx}},\ \frac{k_{xy}}{m}=\frac{k_{yx}}{m}=\omega_{xy}^{\ 2}=\omega_{yx}^{\ 2} \tag{4.4}$$

Theoretically each of the $x$ and $y$ modes can be excited into resonance via mechanical forces $f_x$ and $f_y$, respectively. As explained earlier, the Coriolis coupling from a primary mode to a secondary mode is proportional to both the applied mechanical rotation rate around the sensitive axis ($z$-axis in this case), $\Omega_z$, and the velocity of the primary mode vibration. The cross product of the two vectors is scaled by a scalar angular gain, $\lambda$, which is determined by the geometry and the mode shapes of the device. The opposite-phase Coriolis terms change the gyroscope equations, and thus the gyroscope's overall transfer function when a rotation is applied.

### 4.1.2 Mode-Matching in MEMS Coriolis Gyroscopes

The most common way of interfacing a Coriolis vibratory gyroscope is to excite the $x$ mode (drive mode) into oscillation and then detect the Coriolis-induced deflection along the $y$ mode (sense mode) axis. The deflection along the sense ($y$) mode is an amplitude-modulated (AM) signal with its envelope proportional to the applied rate and at the frequency of the drive mode oscillations. In this case, and in the absence of mode coupling terms, (4.3) can be simplified to

$$\left(s^2+\frac{\omega_x}{Q_x}s+\omega_x^{\ 2}\right)X(s)=\frac{F_x(s)}{m},\ f_x(t)=F_0\cos\omega_x t$$
$$\left(s^2+\frac{\omega_y}{Q_y}s+\omega_y^{\ 2}\right)Y(s)=-2s\lambda\Omega_z X(s). \tag{4.5}$$

In the above representation, the drive mode is actuated by a sinusoidal excitation at $\omega_x$ while the sense mode is excited by the Coriolis force. The drive mode resonator can be used in a series-mode oscillator loop to provide self-sustaining actuation to the gyroscope. The Coriolis-induced displacement of the sense mode can be multiplied by the drive signal to demodulate the rate. Based on (4.5), and given that typically $\omega_x$, $\omega_y >> \Delta\omega$, the drive and sense displacements are derived as

$$\begin{aligned} x(t) &= \frac{Q_x F_x}{m\omega_x^2}\sin\omega_x t,\;\; \dot{x}(t) = \frac{Q_x F_x}{m\omega_x}\cos\omega_x t \\ y(t) &\approx \frac{2\lambda\Omega_z Q_x F_x \cos(\omega_x t + \varphi)}{m\omega_x^2 \times \sqrt{(2\Delta\omega)^2 + (\omega_y/Q_y)^2}},\;\; \varphi \approx \tan^{-1}\frac{\omega_y/Q_y}{2\Delta\omega} \end{aligned} \tag{4.6}$$

where $\Delta\omega$ is the angular frequency split between the two gyroscope modes, and $\omega_y/Q_y$ is the sense mode 3-dB bandwidth ($BW$). The sense mode displacement can also be specifically derived in mode-matched condition (i.e. $\Delta\omega = 0$) and in mode-split condition ($\Delta\omega > BW$) as follows:

$$\begin{aligned} \Delta\omega = 0 &\rightarrow y(t) \approx -\frac{2\lambda\Omega_z Q_x}{m\omega_x^3} Q_y F_x \sin(\omega_x t) \\ \Delta\omega \gg BW &\rightarrow y(t) \approx \frac{\lambda\Omega_z Q_x}{m\omega_x^2}\frac{F_x\cos(\omega_x t)}{\Delta\omega} \end{aligned} \tag{4.7}$$

In mode-matched condition in (4.7), i.e. $\Delta\omega = 0$ (Figure 4.2a), the sense-mode displacement is directly proportional to the sense-mode quality factor, $Q_y$, while in mode-split condition where $\Delta\omega >> BW$ (Figure 4.2b), the sense mode displacement becomes inversely proportional to $\Delta\omega$. In mode-matched condition, the Coriolis-induced displacement always has a quadrature-phase relationship with the drive signal, which facilitates the rate demodulation by simply multiplying the Coriolis output with the drive signal (coherent AM demodulation). However, in mode-split condition, if $\Delta\omega$ is

comparable to the sense-mode $BW$, the phase shift of the AM demodulator must be adjusted accordingly to achieve maximum sensitivity.

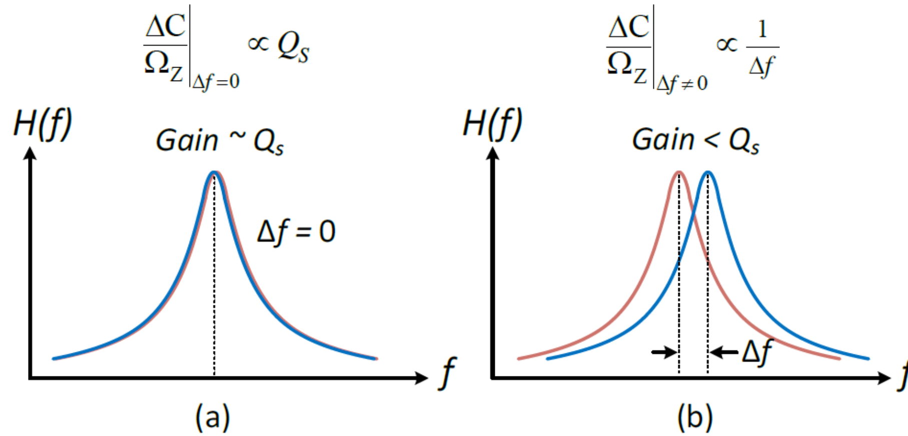


**Figure 4.2**: (a) At mode-matched condition, gyroscope gain is directly proportional to sense-mode quality factor, and (b) at mode-split condition, gyroscope gain is inversely proportional to frequency split. [39]

## 4.2 Gyroscope Performance Specifications

In this section, we discuss the parameters that are commonly used to describe the performance of MEMS vibratory gyroscopes. These parameters include scale factor, bandwidth, resolution, zero-rate output, angle random walk, and bias instability [40].

### 4.2.1 Scale Factor

Coriolis force causes deflection along the sense axis of a vibratory gyroscope. Scale factor, or angular rate sensitivity, of a vibratory gyroscope is the ratio of the change in a measurable quantity to the input rotation rate. The measurable quantity can be sense-mode deflection, sense output current, or sense-mode capacitance variation. Scale factor is typically measured in units of (pA/°/sec) or (mV/°/sec) depending on whether the sensor

output current or the system output voltage is being reported. The current sensitivity of a capacitive gyroscope can be expressed as

$$I_{Coriolis} = \frac{2V_P C_{s0} Q_{eff} x_{drive}}{d_{s0}} \Omega_z \quad (4.8)$$

where $V_P$ is the polarization of the capacitive device, $C_{s0}$ is the sense capacitance at rest, $d_{s0}$ is the sense gap at rest, and $x_{drive}$ is the displacement amplitude of the drive-mode oscillation, also described by (4.6). In mode-matched condition, $Q_{eff}$ is equal to the sense-mode quality factor, $Q_s$. In mode-split condition, $Q_{eff}$ can be modified to match the sensitivity defined by (4.6). Mode-matching maximizes the gyroscope scale factor and thus increases the SNR of the front-end electronics.

### 4.2.2 Bandwidth

Bandwidth (*BW*) of a gyroscope is a measure of its response time to input rotation changes. Bandwidth (single-sided bandwidth) of the sensor is related to the resonance frequency, $f_0$, and quality factor, $Q$ by

$$BW = \frac{f_0}{2Q}(Hz) = \frac{\omega_0}{2Q}\ (rad/s) \quad (4.9)$$

Higher bandwidth provides faster response to rotation changes of the gyroscope. Increasing the sense-mode quality factor increases the SF but also leads to a smaller bandwidth. Therefore, a higher operation frequency is favorable to achieve a large bandwidth while having a high sense-mode quality factor and scale factor.

### 4.2.3 Resolution

The resolution of a gyroscope is the minimum rotation rate that can be distinguished from the noise floor of the system per square root of detection bandwidth and is expressed in units of (°/sec/√Hz) or (°/hr/√Hz). The overall resolution of a gyroscope is defined by

the total noise equivalent rotation (TNEΩ), which is comprised of two main components: the mechanical noise equivalent rotation (MNEΩ) and the electrical noise equivalent rotation (ENEΩ).

$$TNE\Omega = \sqrt{MNE\Omega^2 + ENE\Omega^2} \tag{4.10}$$

Mechanical noise is caused by the Brownian motions of the suspended mass along the sense axis. By equating the displacement caused by the Brownian motion to the displacement caused by the mechanical rotation, MNEΩ can be derived as:

$$MNE\Omega = \frac{1}{2x_{drive}} \sqrt{\frac{4k_B T}{\omega_s m Q_s}} . \sqrt{BW} \tag{4.11}$$

where $k_B$ is the Boltzmann constant ($1.38\times10^{-23}$ *Joules/K*), $T$ is temperature in Kelvin, $m$ is mass, $\omega_s$ is the sense-mode angular frequency, $Q_s$ is the sense-mode quality factor, and $BW$ is the measurement bandwidth (in units of Hz).

Electronic noise is dominated by the input-referred current noise of the sense pickoff circuits. Using the same method, ENEΩ can be derived as

$$ENE\Omega = \frac{d_{s0}}{2V_P C_{s0} Q_{eff} x_{drive}} . I_{n,total} . \sqrt{BW} \tag{4.12}$$

where $I_{n.total}$ is the total input-referred current noise of the sense pickoff electronics, and $Q_{eff}$ is the same effective quality factor described in (4.8). In other words, ENEΩ is the ratio of the input-referred current noise to the current sensitivity of the gyroscope. Both MNEΩ and ENEΩ are inversely proportional to the amplitude of drive-mode displacement, $x_{drive}$. Therefore, increasing the drive amplitude within the linear operation region is commonly used to enhance the overall gyroscope noise performance [41, 42].

Mode-matching can significantly reduce ENEΩ by increasing the current sensitivity and thus improving the SNR of the gyroscope output [36, 41]. However, MNEΩ is

unaffected by the frequency split between the two modes because the mechanical noise and the Coriolis-induced displacement see the same gain to the gyroscope output, and thus are affected equally by the mode split and the transducer. The value of ENEΩ is typically much lower than MNEΩ by design. ENEΩ can be reduced by decreasing the input-referred current noise of the sense TIA by careful design, which will be discussed in chapter 5.

### 4.2.4 Zero-Rate Output and Bias Drift

Zero-rate output (ZRO) is the output of a gyroscope in the absence of angular rotation. The long-term drift of the ZRO is called *bias drift* (measured in °/hr or °/sec), which shows the long-term stability of the gyroscope stationary output. The long-term stability is important when the rate output is integrated to calculate the angle. In such a case, the bias drift of the sensor can accumulate and cause errors in the deduced orientation angle.

The drift of ZRO is most commonly attributed either to the drift of the stiffness and damping coupling or to the variations of mode-split, resonance frequency, quality factor, and transduction coefficient over time. Environmental effects such as temperature can also contribute to bias drift.

### 4.2.5 Allan Variance

Bias drift is a statistical measure of how a sensor performs over short or long periods of time. Consequently, stochastic methods are used to model bias drift. The most useful and informative method is Allan variance [43, 44, 33]. Allan variance is based on calculating the standard deviation of the averages of different sized clusters, of a large array of bias-only samples of the sensor output. Allan variance can be mathematically represented as

$$\sigma^2(\tau) = \frac{1}{2(n-1)} \sum_i \left( y(\tau)_{i+1} - y(\tau)_i \right)^2 \tag{4.13}$$

where $\sigma(\tau)$ is the root Allan variance as a function of averaging time $\tau$, $n$ is the total number of data clusters of size $\tau$, and $y(\tau)_i$ is the average of the measurement in cluster $i$.

The root Allan variance at each $\tau$ is the standard deviation of the averages of $\tau$-size data clusters. In other words, the value of $\sigma(\tau)$ at each $\tau$ is a measure of the error between each two consecutive samples of the averaging size $\tau$. Therefore, if the output contains solely thermal noise and no other drift errors, then both the value of the averages of size $\tau$ and the standard deviation of these averages, $\sigma(\tau)$, constantly decrease as $\tau$ increases. However, if the output bias monotonically drifts over time due to temperature change, then with an increasing $\tau$, the difference and thus the standard deviation between the averages of size $\tau$ will also increase. From an intuitive perspective, the root Allan variance can be considered as the probability and extent of having an erroneous bias output after $\tau$ seconds of averaging. This intuition can be directly used to understand the stringent requirements of inertial sensors for navigation.

Figure 4.3 shows a sample Allan variance analysis in which the values of root Allan variance are plotted as a function of averaging time, $\tau$, on a log-log scale [44]. The time-domain data from the stationary sensor contains different noise sources, each correlated to a different averaging time and thus corresponding to a different part of the Allan variance plot. This allows a thorough analysis of the time domain drift behavior of the sensor.

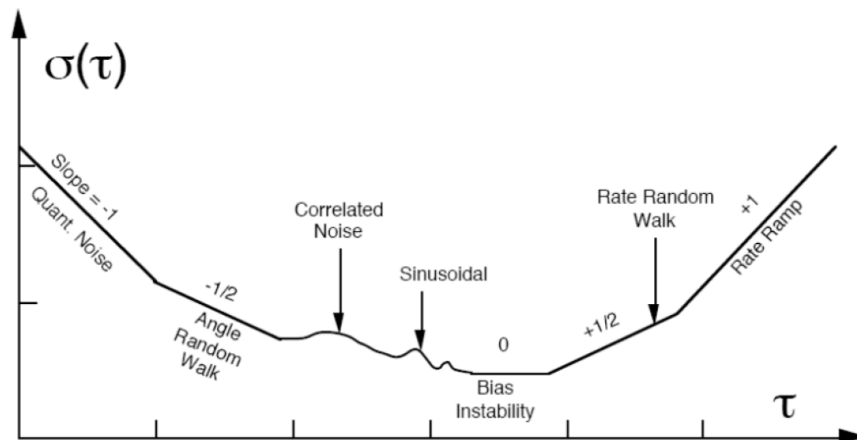


**Figure 4.3**: Typical Allan variance plot showing different regions corresponding to different sources of noise and drift. [39]

The main drift and noise components in a typical Allan variance plot are quantization noise, angle random walk (ARW), bias instability, rate random walk (RRW), and rate ramp. The random processes associated with these error terms can be assumed to be uncorrelated. Therefore, the total Allan variance at each $\tau$ can be calculated by

$$\sigma_{total}^2(\tau) = \sigma_{Quantization}^2(\tau) + \sigma_{ARW}^2(\tau) + \sigma_{Bias-drift}^2(\tau) + \sigma_{RRW}^2(\tau) \quad (4.14)$$

*Quantization Noise*

Quantization noise in the Allan variance plot has a slope of -1 when plotted in a log-log scale. The expression for quantization noise can be found in [45]. This component is measured at the lowest averaging times as related to the high-frequency sampling at the sensor output. Notice that the quantization noise formulas are different for a Nyquist rate analog-to-digital (A/D) converter and a noise-shaped oversampled A/D converter backend.

*Angle Random Walk*

Angle random walk (ARW) is the angle error build-up over time, due to white noise in the angular rate output. If the power spectral density (PSD) of the wideband white noise is given by $S_W(f) = N^2$, where $N$ is the input-referred angular rate noise of the system (TNEΩ) in °/hr/√Hz, then the ARW variance is [45]:

$$\sigma_{ARW}^2(\tau) = \frac{N^2}{\tau} \quad (4.15)$$

So, on a log-log scale Allan variance plot, ARW is represented by a straight line with a slope of -1/2 (a function of $\tau^{-1/2}$). The value of ARW can be found by fitting a line with a slope of -1/2 to the Allan variance plot and reading the value of the line at $\tau = 1$ sec, which is equal to $N$. Typically, the Allan variance plot itself has $\tau = 1$ in its ARW region. If $\sigma(\tau)$

is plotted in units of °/hr, then ARW has the same value of $N$ in units of °/hr/√Hz. However, it is more common to report ARW as $N/60$, in units of °/√hr, to be directly used as a measure of short-term stability of the system. For instance, a gyroscope ARW of 0.01 °/√hr results in an integrated angle error of 0.005° after 15 minutes of integration.

*Bias Instability (Drift)*

It is shown in [45] that the contribution of random low-frequency noise with $1/f$ PSD is a flat line with slope of zero on the Allan variance plot. The value of the flat region in Allan variance plot is called bias instability which represents the minimum achievable error between consecutive averages of size larger than the bias drift timescale. In other words, if the averaging time is shorter than that of the bias drift time constant, the error between consecutive averages reduces with the increase of $\tau$. However, for averaging time beyond the bias drift time constant, this error will not reduce anymore.

*Rate Random Walk and Rate Ramp*

Rate random walk (RRW) is an unknown random process with acceleration PSD, creating a slope of +1/2 on the log-log Allan variance plot. RRW can be caused by demodulation of $1/f^2$ terms from the phase noise of the drive loop by the zero-rate output in the sense-mode response.

Rate ramp is caused by deterministic errors that monotonically change the output over long periods of time [45]. The main source of this error is environmental variations, which changes the gyroscope transfer function and its resonance parameters. Temperature variation for instance, can cause drift of output bias by affecting the magnitude of the quadrature and damping coupling terms, thereby changing the output bias terms at the demodulator output. Moreover, temperature variation can affect both resonance frequency and quality factor of the gyroscopic resonance modes, and consequently change the

response of the gyroscope to the coupling terms. Rate ramp region with slope of +1 is more commonly recognized on most of the Allan variance plots.

In a coherent demodulation scheme, temperature-induced frequency shift does not affect the gyroscope performance directly because both modes shift equally as temperature changes. However, this frequency shift can change the output bias when the self-sustaining actuation signal is coupled to the sense-mode output current through reactive electrical coupling paths, such as capacitive feedthrough, Through-Silicon-Via (TSV) structures, and inductive coupling through long parallel unshielded signal traces on the PCB or the interface IC. Reactive coupling can become a significant source of bias variation in high-frequency gyroscopes, where higher oscillation frequency generates larger output bias and bias variation, for the same amount of capacitive or inductive coupling. The relatively lower sensitivity of high-frequency gyroscopes further exaggerates the effect of such electrical couplings. Careful circuit implementation and sophisticated packaging for high-frequency CVG is important.

### 4.2.6 Determining Minimum Detectable Rotation Rate:

If the output noise of an ideal gyroscope is only limited by the white noise from both the MEMS device and the circuits, the minimum detectable rotation rate is theoretically determined by the ARW and the bandwidth. However, in a real gyroscope system, the other components of the Allan variance plot also induce errors in the rate output. The flicker noise and the slowly varying temperature-induced drift are the two most common sources of long-term drift in MEMS gyroscopes.

Figure 4.4 depicts the contributions of these drift and noise sources to the Allan variance plot of a typical gyroscope. While the standard deviation due to white noise reduces with the increase of averaging time, the flicker noise flattens the Allan variance plot. In the presence of slight temperature-induced drift, the rate error starts increasing with $\tau$ above a certain value of $\tau$, implying further increase in the integrated angle error than

expected by only integrating the white and flicker noises. The time constant $\tau$ where the roll-up takes place, determines the optimum averaging size of the rate output for angle detection. This optimum averaging size determines the suitable sampling rate and the temperature recalibration period for the navigation system.

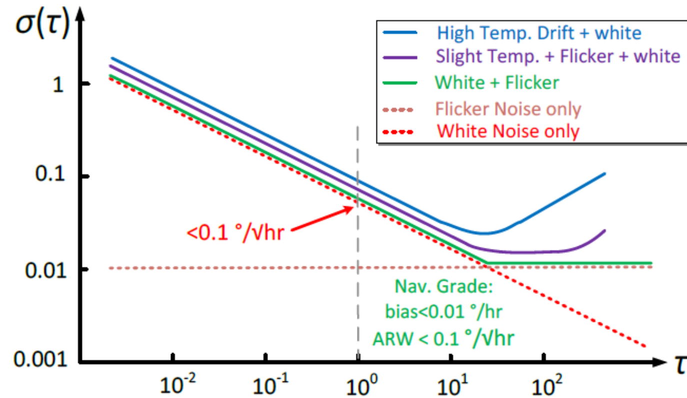


**Figure 4.4**: The Allan variance plot of a MEMS gyroscope with different noise or environment error sources considered. Allan variance for an ideal gyroscope is dominated by ARW region only. Only flicker can affect the ARW-only trend of the Allan variance plot while the temperature effects are sufficiently compensated. [39]

In the presence of large temperature drifts, the roll-up of the Allan variance plot starts at a smaller $\tau$, resulting in a larger bias instability. The reduction of the bias instability time constant, and more importantly the increase of the bias instability can be detrimental to any deduced reckoning operation. Therefore, reduction of temperature effect on the bias and scale factor drift is of the utmost importance when using gyroscopes for navigation.

Using low-flicker bipolar devices rather than CMOS transistors for analog frontend circuit (Ex: transimpedance amplifier) can reduce flicker further. Flicker noise from the backend electronics can also be reduced by using high-resolution A/D converters (after the analog frontend) and all digital architectures. Moreover, the phase noise of the drive signal can be demodulated into baseband $1/f^2$ noise that can result in rate random walk. Using lower flicker devices and architectures can reduce the phase noise of drive loop.

Regarding the temperature effects, besides using temperature compensation techniques, reducing feedthrough and inductive coupling in the gyroscope can also reduce rate ramp. With completely compensated temperature effects, in the presence of flicker and thermal noise sources only, the Allan variance plot looks closest to the green line in Figure 4.4, where the Allan variance line flattens at the bias instability levels required by the desired application, e.g. < 0.01 °/hr for navigation. To achieve this level of temperature compensation, sophisticated electrical calibration and temperature compensation techniques are required.

### 4.2.7 Scale Factor Instability and Drift Mechanisms

The stability of gyroscope scale factor depends strongly on the stability of each of the parameters in (4.6) over time and temperature variation. While frequency variation with temperature is relatively low (0.2-0.4%) over the entire temperature range, the total quality factor variations can go up to 50%, which can affect the scale factor stability dramatically. Moreover, variations of mode split, $\Delta\omega$, can be a significant source of scale factor variation especially when the gyroscope is nominally operating at near-mode-matched condition.

Variation of mode-split can be mainly caused by variations of stiffness coupling between the two modes due to anisoelasticity [46]. Besides the parameter drifts effect on the amplitude of the sense-mode displacement, the phase of the sense signal also depends on the bandwidth and mode-split of the gyroscope, resulting in scale factor degradation and leakage of quadrature error into the in-phase rate output.

A scale factor stability of 100 ppm is required for the high-end tactical gyroscope market. This level of stability needs both the electrical compensation techniques and additional calibration. A temperature stabilization technique based on chip-level ovenization for high-frequency MEMS gyroscopes is proposed in this work and will be introduced in Chapter 5.

# CHAPTER 5

# INTERFACE SYSTEM FOR OVENIZED MEMS GYROSCOPES

This chapter introduces the design and implementation of the interface circuit of a six-degree-of-freedom silicon MEMS inertial measurement unit (IMU). First, we will briefly introduce the MEMS sensor devices. Second, we will introduce the interface circuit of the gyroscopes, accelerometers, and the micro-oven control loop. All the interface circuits have been implemented with commercial off-the-shelf electronics. Third, the measurement result of the gyroscopes' scale factor, output bias, bias instability, and Allan deviation will be shown. The last part will demonstrate how the proposed ovenization technique mitigates the *temperature-induced frequency drift* problem and improves the performance of the 3-axis gyroscopes.

## 5.1 The Single Chip Silicon MEMS TIMU

Figure 5.1 shows the die and the SEM photographs of the single-chip timing and inertial measurement unit (TIMU) with dimensions of 4.5mm×5.5mm. This TIMU has robust 3-axis high-frequency resonant gyroscopes, 3-axis high-bandwidth accelerometers, and a high-$f{\cdot}Q$ BAW timing resonator. The TIMU is fabricated using the HARPSS+ process with wafer-level-packaging. The resonant devices (i.e., gyroscopes and resonator) and stationary accelerometers are enclosed in separate cavities by the bonding, and the accelerometer cavity is brought to atmospheric pressure during dicing through vent holes located at the edge of the cavity to ensure an over-damped stable quasi-static response [47].

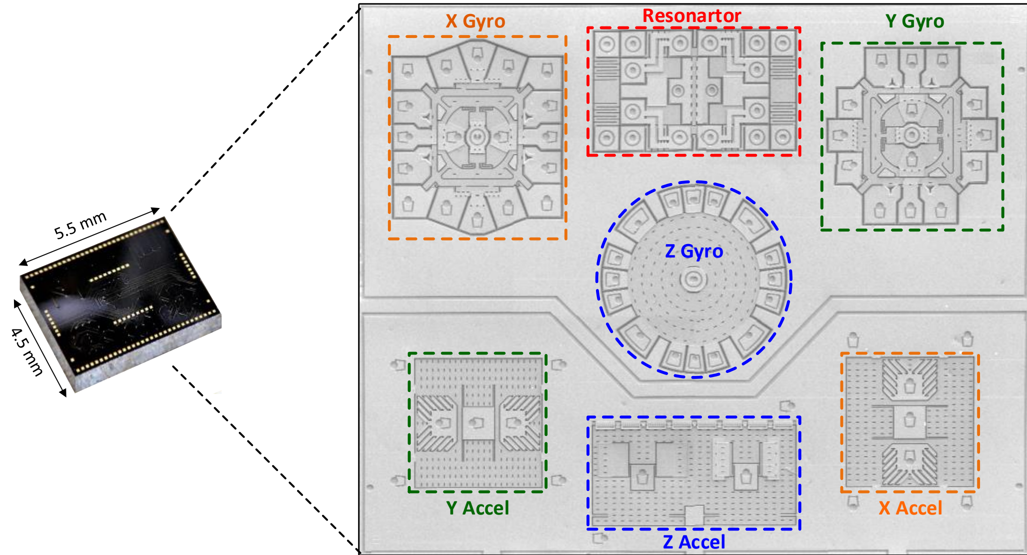


**Figure 5.1:** Image of the wafer-level-packaged TIMU and SEM images of the uncapped TIMU die.

### *5.1.1 Three-Axis Gyroscopes*

The z gyroscope is implemented using a quasi-solid disk BAW structure and has an operational frequency of 5.4MHz. The x and y framed-annulus gyroscopes are orientated in orthogonal directions. This is the first single-chip IMU with robust high-frequency resonant gyroscopes for all three sensing axes. The operational frequencies of the x and y gyroscopes are slightly different (700kHz and 660kHz), which can reduce the crosstalk. The handle layer and the substrate are electrically connected using through-BOX-layer poly plugs to ensure proper grounding and AC signal isolation. All 3-axis gyroscopes were designed by Haoran Wen and Anosh Daruwalla [48].

### *5.1.2 Three-Axis Accelerometers*

All three accelerometers use the nano-gap electrodes enabled by the HARPSS+ process. The nano-gaps can improve the electrode transduction and capacitive sensitivity

of the sensor significantly. The nano-gaps allow the use of a stiffer structure with higher resonant frequencies (> 10 kHz), therefore enabling a wider bandwidth. The x-axis and y-axis accelerometers have sloped sensing electrodes, which provide a larger than gap-size traveling range and enable the use of non-sloped nano-gaps as shock stops. The z-axis accelerometer uses a see-saw torsional design, which increases the yield and immunity against stiction. All three axes accelerometers were designed by Yaesuk Jeong [49].

### *5.1.3 Timing Resonator*

In navigational applications, stable frequency references (or timing units) are important for robust IMU operation where the quality of the frequency references can be crucial for the gyroscope performance. Conventional solutions are based on the individually packaged and assembled timing unit and IMUs, which results in larger size, higher cost, and lower reliability. Therefore, having an on-chip robust high-frequency timing unit is essential. A cross-sectional Lamé mode resonator is integrated on the TIMU as a potential timing reference [50]. The design uses a localized cross-sectional mode with wide tethers as low-loss anchors to minimize the vibration sensitivity. Integrated heaters are built around the resonator to provide the potential for closed-loop ovenization of the TIMU for high temperature stability [51]. The heater and the oven control loop design will be introduced in detail in the next section.

## 5.2 Interface Circuits for the 6-DoF MEMS IMU

Figure 5.2 shows the block diagram of the complete gyroscope interface circuits. The entire block diagram includes four parts: the drive loop, the sense channel, the

demodulator, and the DC tuning voltage generator. The drive loop generates a sinusoidal oscillation (drive signal) at the resonance frequency of the gyroscope to actuate the device continuously. The sense channel extracts the amplitude-modulated (AM) rate signal from the sense electrodes. The AM rate signal is next multiplied by the drive signal using an analog multiplier (AD835) and then low-pass filtered to demodulate the baseband rate signal. The DC tuning voltage generator provides the polarization voltage ($V_P$) to enable transduction, the frequency tuning voltage ($V_T$) to match the frequencies/modes, and the quadrature tuning voltage ($V_Q$) to cancel the quadrature.

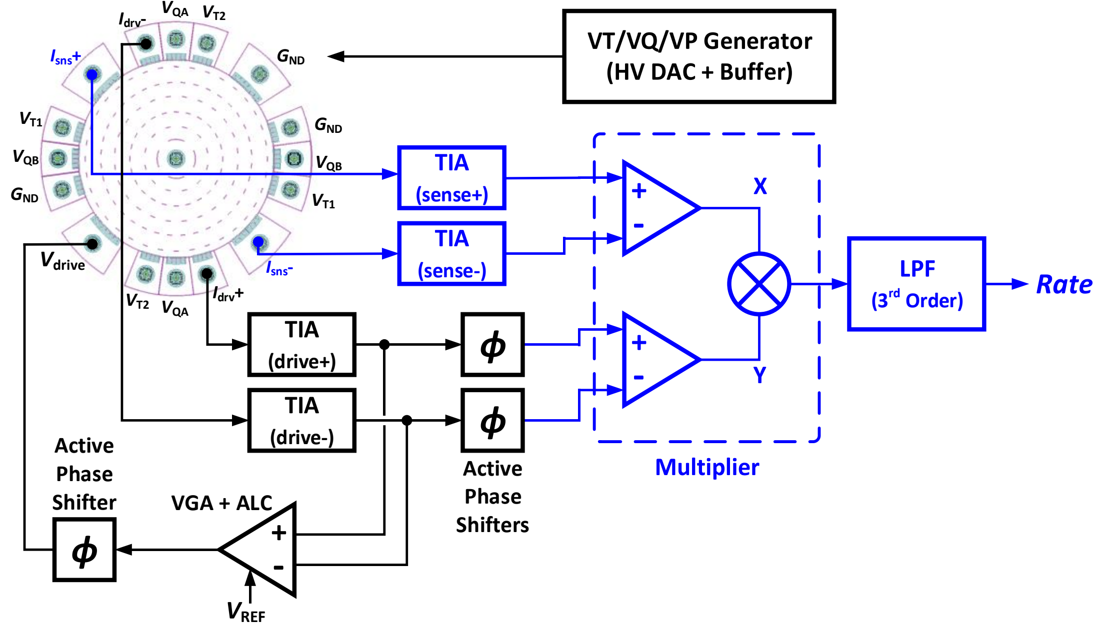


**Figure 5.2**: The block diagram of the complete gyroscope interface circuits. Here we take the z gyroscope as an example.

### *5.2.1 Transimpedance Amplifier (TIA) Design*

The transimpedance amplifier is the most important block in the gyroscope interface circuit because it is the very first circuit that receives the output current from the MEMS device. For the drive loop, the noise of TIA has a significant impact on the phase noise

performance. For the sense channel, the gain and noise of TIA determine the overall sensor scale factor and the signal-to-noise ratio (SNR), respectively.

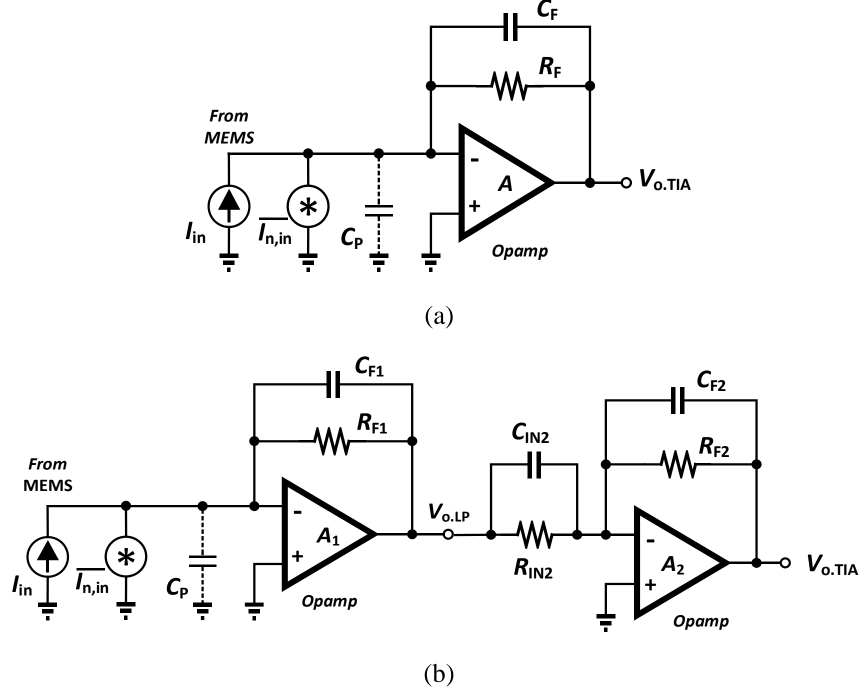


**Figure 5.3**: (a) The conventional single-stage resistive feedback TIA, and (b) the proposed two-stage low-pass, high-pass TIA (LP-HP TIA).

The single-stage resistive-feedback TIA (Figure 5.3a) is one of the conventional TIA architectures. However, a direct tradeoff exists between the bandwidth and the input-referred current noise performance. This tradeoff can be explained by equation (5.1) and (5.2), which show the input-referred current noise ($\overline{I_{n.in}}$) and the bandwidth ($BW$) expressions of the conventional TIA, respectively.

$$\overline{I_{n,in}^2} = \frac{4kT}{R_F} + \frac{1}{R_F^2}\overline{V_{n,A}^2} + \omega^2(C_P + C_F)^2 \cdot \overline{V_{n,A}^2} \tag{5.1}$$

$$BW = \frac{A+1}{2\pi R_F(C_p + C_F)} \tag{5.2}$$

In (5.1), $R_F$ is the feedback resistance, and $\overline{V_{n.A}}$ is the input-referred voltage noise of the opamp. $C_P$ is the total shunt parasitic capacitance at TIA input, which includes the parasitic capacitance of the opamp's input, the MEMS device, and the PCB traces. In (5.2), $A$ represents the dc voltage gain of the opamp. We can easily observe that if $R_F$ is reduced to increase the bandwidth, the first two terms of $\overline{I_{n,in}^2}$ will rise. This direct tradeoff poses a challenge for our TIA design because all our gyroscopes use high-frequency bulk-acoustic (BAW) modes. It is difficult to design a higher bandwidth TIA without sacrificing the noise performance.

To mitigate this BW-noise tradeoff problem, we propose a two-stage low-pass, high-pass TIA (LP-HP TIA) architecture as shown in Figure 5.3(b). The first stage uses a much larger $R_{F1}$ (>> $R_F$ in Figure 5.3a) to make the contribution of the first two terms in (5.1) nondominant. The $\overline{I_{n,in}^2}$ of the LP-HP TIA can be expressed as

$$\overline{I_{n,in}^2} = \frac{4kT}{R_{F1}} + \left[\frac{1}{R_{F1}^2} + \omega^2 (C_P + C_{F1})^2\right] \overline{V_{n,A1}^2} + \left[\frac{1}{R_{F2}^2} \overline{V_{n,A2}^2} + 4kT \frac{1}{R_{F2}}\right] \left(\frac{C_{F1}}{C_{F2}}\right)^2 \qquad (5.3)$$

In (5.3), the $R_{F1}$-related terms can be neglected by choosing a large enough $R_{F1}$ value. The $R_{F2}$-related terms can also be negligible by choosing $C_{F2} >> C_{F1}$, in our case, $C_{F2} > 100 \cdot C_{F1}$.

Although the large $R_{F1}$ narrows the first stage bandwidth and hence reduces the transimpedance gain, the zero introduced by $C_{in2}$ and $R_{in2}$ can compensate the bandwidth loss and the gain loss at the operational frequency ($f_{res}$). The transimpedance gain ($T_z$) of the proposed TIA can be expressed as

$$\frac{V_{o.TIA}}{I_{in}} = \frac{R_{F1} R_{F2}}{R_{IN2}} \frac{(1 + sR_{IN2} C_{IN2})}{(1 + sR_{F1} C_{F1})} \approx R_{F2} \frac{C_{IN2}}{C_{F1}}\bigg|_{\omega=\omega_{res}} \qquad (5.4)$$

Table 5-1 summarizes the transimpedance gain ($T_z$), bandwidth ($BW$), and input-referred noise current ($\overline{I_{n.in}}$) of these two types of TIAs. Compared to the conventional single-stage TIA, the proposed LP-HP TIA has the following advantages:

1) lower $\overline{I_{n.in}}$ because the $R_F$ noise is reduced, and the opamp noise ($\overline{V_{n.A}}$) is also suppressed by the larger $R_F$
2) higher transimpedance gain ($T_z$) because now $T_z$ is determined by the capacitance ratio $C_{IN2}/C_{F1}$, which can be increased without much less bandwidth penalty
3) higher bandwidth because the $BW$ is determined mainly by $C_{F2}$ and $R_{F2}$, and we can choose a small $R_{F2}$ (<< $R_F$ in Figure 5.3a) to extend the $BW$ further

Table 5-1
Comparison of the Single-Stage and Two-Stage TIAs

| | **Conventional Single-Stage TIA** | **Two-Stage LP-HP TIA** |
|---|---|---|
| **Transimpedance Gain ($T_z$) at $f_{res}$** | $\approx -R_F$ | $R_{F2} \cdot \frac{C_{IN2}}{C_{F1}}$ |
| **Bandwidth ($BW$)** | $\frac{A+1}{2\pi R_F (C_p + C_F)}$ | $\approx \frac{1}{2\pi R_{F2} C_{F2}}$ |
| **Input-referred current noise ($\overline{I^2_{n,in}}$)** | $4kT\frac{1}{R_F} + \overline{V^2_{n,A}}\left[\frac{1}{R_F^2} + \omega^2 (C_P + C_F)^2\right]$ | $\approx \omega^2 (C_P + C_{F1})^2 \cdot \overline{V^2_{n,A1}}$ |

Here we demonstrate the superior performance of the LP-HP TIA with a measured gain and $BW$ result (Figure 5.4). We use the Analog Device ADA4817 for all the opamps in the TIAs. The circuit parameters of the LP-HP TIA were used for the z gyro sense channel. The measured frequency response shows that the LP-HP TIA can easily achieve a four times higher gain and a 50% wider bandwidth than the conventional single-stage TIA.

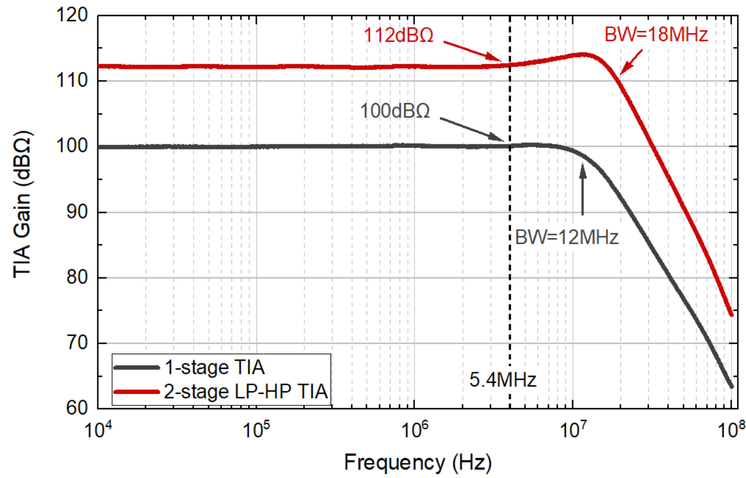


**Figure 5.4**: The measured gain and bandwidth of the two types of TIAs. For the single-stage TIA, $R_F$ = 100KΩ, $C_F$ = 0. For the two-stage LP-HP TIA, $R_{F1}$ = 5MΩ, $C_{F1}$ = 1pF, $R_{IN2}$ = 25KΩ, $C_{IN2}$ = 100pF, $R_{F2}$ = 4KΩ, $C_{F2}$ = 2.5pF. ($C_P$ = 2pF at both cases)

Figure 5.5 shows the input-referred noise spectral density of the two types of TIAs. The LP-HP TIA exhibits a much lower flicker noise at frequencies below 100Hz, and also a lower thermal noise at the 5.4MHz z gyro operational frequency. The thermal noise improvement is even larger at the x/y gyro operational frequency (700KHz).

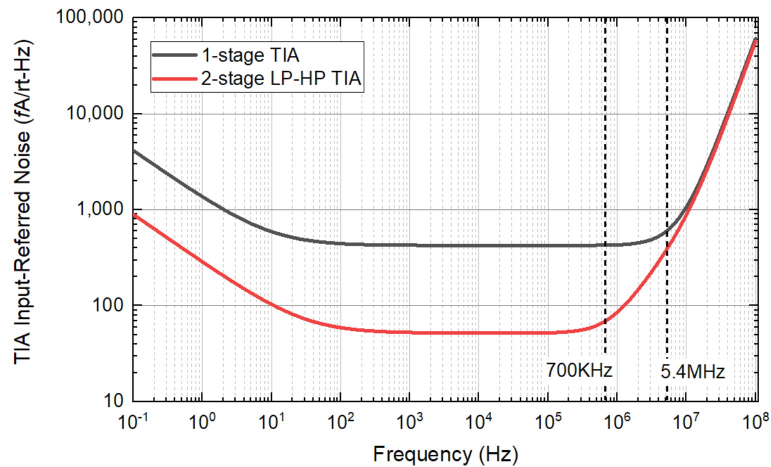


**Figure 5.5**: The Cadence noise simulation of the two types of TIAs. For the single-stage TIA, $R_F$ = 100KΩ, $C_F$ = 0. For the two-stage LP-HP TIA, $R_{F1}$ = 5MΩ, $C_{F1}$ = 1pF, $R_{IN2}$ = 25KΩ, $C_{IN2}$ = 100pF, $R_{F2}$ = 4KΩ, $C_{F2}$ = 2.5pF. ($C_P$ = 2pF at both cases)

*5.2.2 Feedthrough Cancellation*

The feedthrough in a MEMS resonator or gyroscope is the capacitive coupling between any two of the electrodes. In a MEMS gyroscope, the feedthrough capacitance ($C_{FT}$) between the drive electrode and each sense electrode (direct or indirect channel) is especially unwanted because it can cause the drive loop malfunction or the false gyro output reading (ZRO). The typical sources of the feedthrough capacitance are:

1) the direct overlapping capacitance of the transducer
2) capacitive coupling through the substrate
3) capacitive coupling through the device layer
4) interconnects of the wafer-level packaging (ex: through-silicon vias, TSV)
5) the signal traces on PCB

These feedthrough sources are illustrated in Figure 5.6.

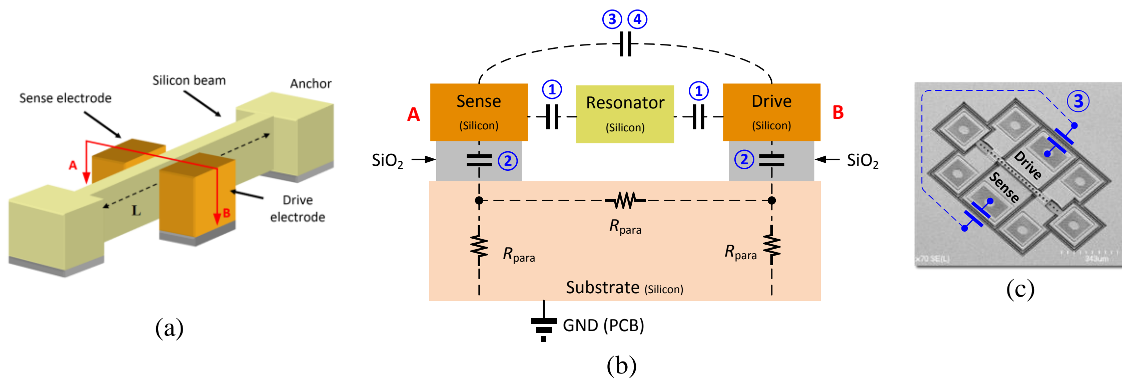


**Figure 5.6**: (a) The typical structure of a resonator, (b) the cross-sectional view (A↔B) of the left-hand side resonator, and (c) an example of the capacitive coupling through the device layer

Because of feedthrough, the magnitude response of the resonance peak changes as described by Figure 5.7b (top), where an anti-resonance is created at the frequency of

$$f_p = \frac{1}{2\pi\sqrt{L_m \frac{C_{FT}C_m}{C_{FT}+C_m}}} \tag{5.5}$$

where $f_p$ represents the parallel-mode resonance. Figure 5.7b (bottom) shows the phase response of the resonance peak, where the resonator current phase has 0° transition points at both the series and parallel resonance frequencies.

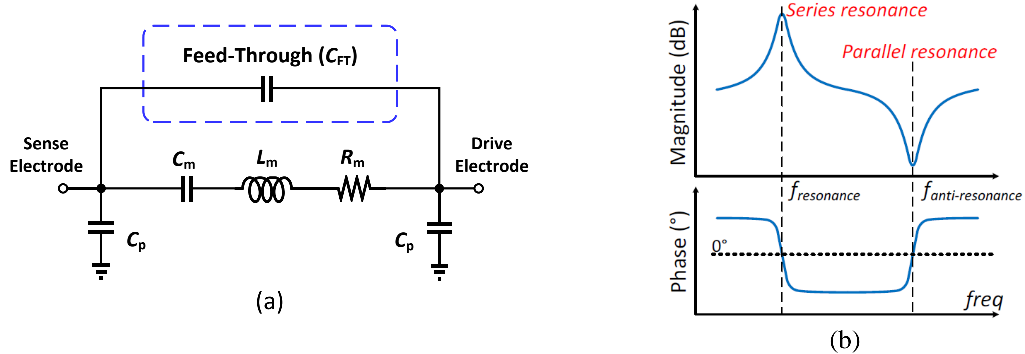


**Figure 5.7**: (a) Typical resonator model with the parasitic feedthrough capacitance ($C_{FT}$), and (b) $C_{FT}$ creates an anti-resonance in the magnitude response of the resonator. At the anti-resonance frequency the phase response of the resonator rolls back up; a very large $C_{FT}$ can roll the phase back up before the zero-crossing, and thus prevent the phase from crossing zero.

In (5.5), with a larger $C_{FT}$, the frequency $f_p$ becomes closer to the series-mode resonance frequency, $f_{res}$. If $f_p$ falls too close to the series resonance, $f_{res}$, the phase may roll back up before reaching the 0° point, and thus makes a series-mode oscillator unable to lock into oscillation. The amount of feedthrough capacitance in most packages typically ranges from tens to hundreds of femtofarads (fF). The responses in Figure 5.7b are plotted with $C_{FT}$ = 50fF, and $C_m$ = 140aF.

A feedthrough cancellation circuit in parallel with the resonator (Figure 5.8) can cancel the feedthrough effect by providing a negative feedthrough signal across the resonator. The drive signal, $V_{IN}$, is first inverted by the feedthrough cancellation amplifier. Then, the inverted signal drives the feedthrough cancellation capacitance ($C_1$) to generate

a current signal ($i_1$) to cancel the feedthrough current ($i_{FT}$). If the feedthrough cancellation amplifier has an infinitely wide bandwidth (i.e., zero phase shift), the feedthrough effect can be cancelled completely by properly choosing an amplifier gain.

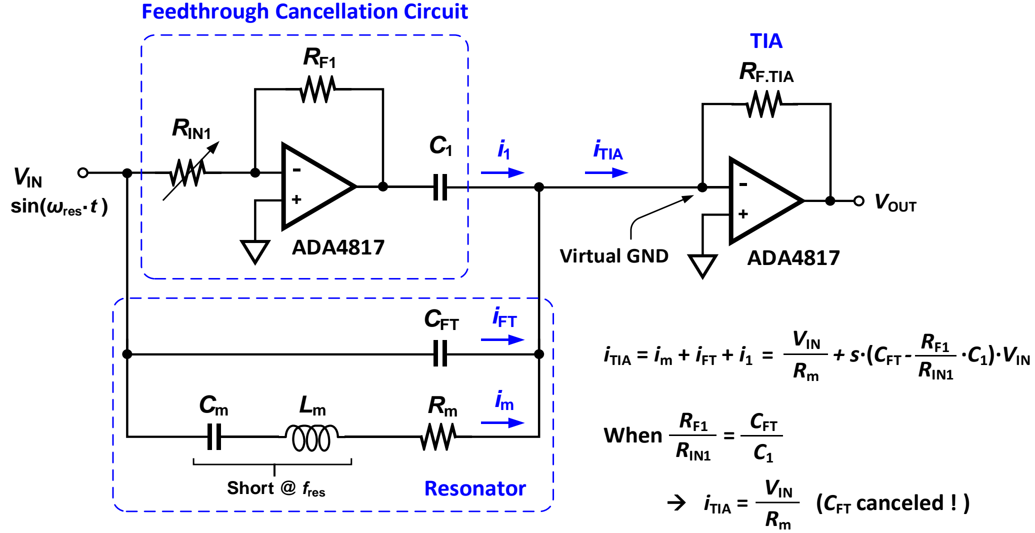


**Figure 5.8**: Operating principle of the feedthrough cancellation circuit used in this work

In reality, the feedthrough cancellation amplifier will always have a finite bandwidth, and, hence, will provide a finite phase shift. If we consider a finite phase shift $\varphi$ of the inverting amplifier as shown in Figure 5.9(a), then the feedthrough cancellation equation can be derived as

$$\begin{aligned} i_{TIA} &= i_1 + i_{FT} + i_m \\ &= V_{in} \cdot sC_{FT}\{[1 - A\cos(\varphi)]\sin(\omega_{res}t) - A\sin(\varphi)\cos(\omega_{res}t)\} + i_m \end{aligned} \quad (5.6)$$

where $i_{TIA}$ stands for the net signal current going into the TIA. Inside the curly bracket of (5.6), the $sin(\omega_{res}\cdot t)$ related feedthrough term can be eliminated by choosing a proper amplifier gain $A$. However, the $cos(\omega_{res}\cdot t)$ related feedthrough term remains. Figure 5.9(b) shows the simulated feedthrough cancellation effectiveness with different phase shift ($\varphi$)

values. Even a small phase shift difference can cause a significant feedthrough level variation. So, to minimize the remaining feedthrough, the inverting amplifier's bandwidth must be wide enough, or we will have to insert a phase adjustment mechanism to the inverting amplifier.

The feedthrough cancellation amplifier only adds a small amount of current noise to the $\overline{I_{n.in}}$ of the TIA because the feedthrough canceling capacitance ($C_1$) is usually small (< 0.2pF) and creates a large impedance between the amplifier and the TIA. The added noise current to $\overline{I_{n.in}}$ can easily be less than 100fA/$\sqrt{Hz}$ with proper design.

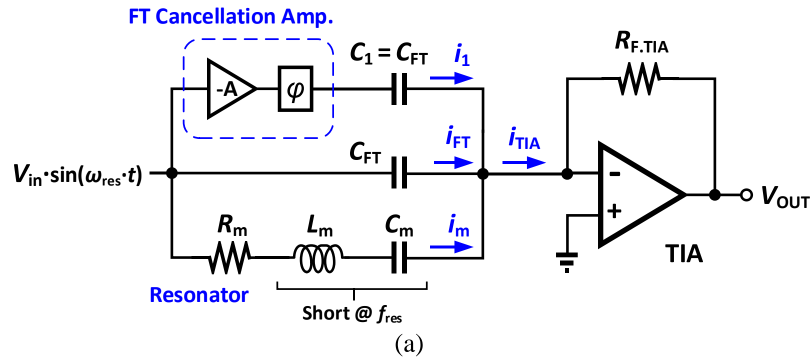

(a)

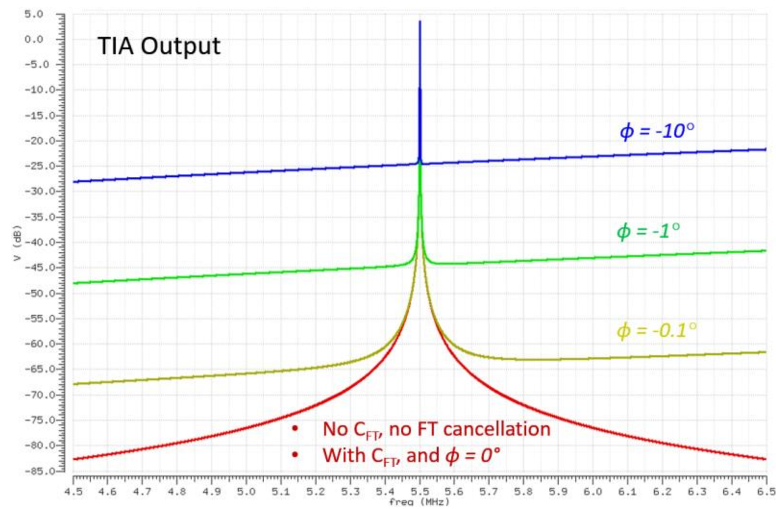

(b)

**Figure 5.9**: (a) Include the phase shift ($\varphi$) effect of the feedthrough cancellation amplifier into consideration, (b) simulated feedthrough cancellation effectiveness with different phase shift $\varphi$

### *5.2.3 Drive Loop*

Figure 5.10(a) shows the complete drive loop circuits. The variable gain amplifier provides a gain tuning capability in which the VCA810 from Texas Instrument is used. The phase shifter provides compensate the excess phase shift generated by the TIA and VGA to ensure the whole drive loop has a 0° (or 360°) phase at the resonance frequency. The oscillator can still work even if the drive loop locks at a frequency slightly off the resonance frequency, however, the phase noise performance will degrade. Figure 5.10(b) shows the detailed circuits of the phase shifters used for all three axes gyroscopes.

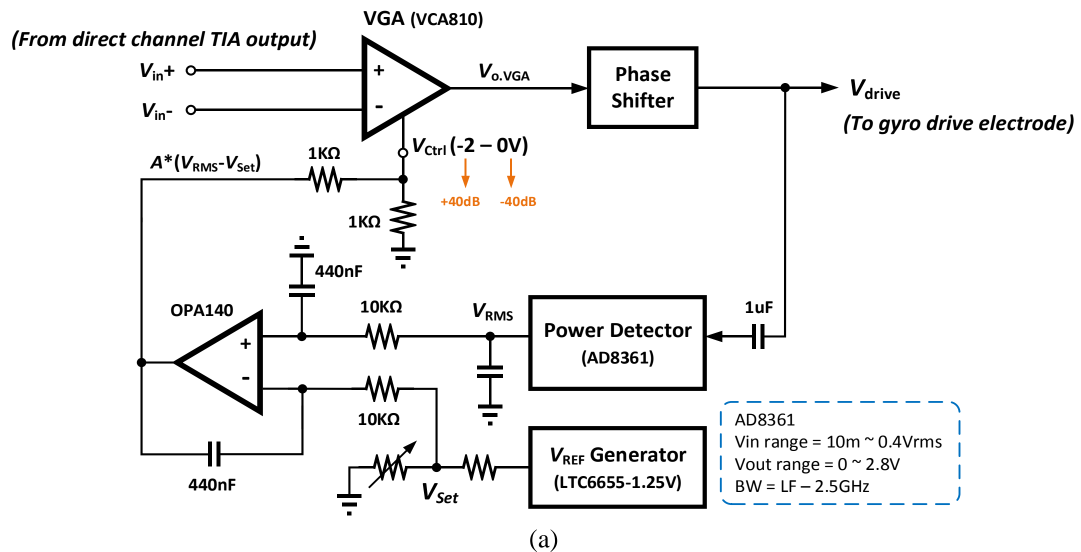


(a)

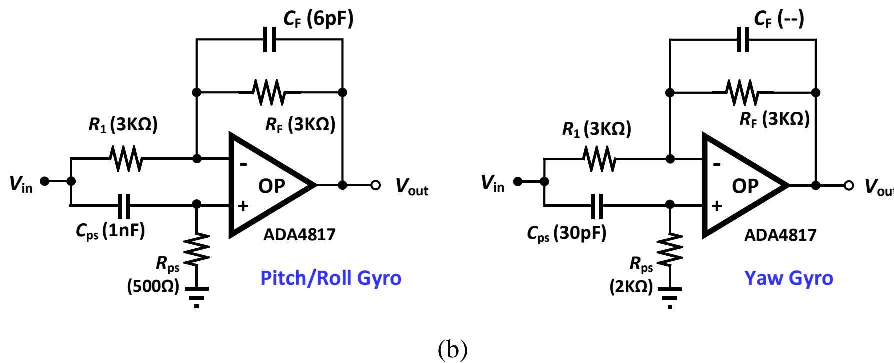


(b)

**Figure 5.10**: (a) The complete drive loop circuits; (b) The detailed schematic of the phase shifters used for z and x/y gyroscopes

The amplitude (or rms-power) detector is a key component in the automatic level control (ALC) part. We chose AD8361 power detector here because it works well for small input signals (<10m$V_{rms}$) and has a wide operational frequency range. LTC1968 can also detect small input signal well, however, its internal ADC exhibits a larger input-output latency which can cause amplitude fluctuation in the x/y drive loop.

The error amplifier (OPA140) subtracts the outputs of the power detector and the amplitude-set voltage ($V_{Set}$) generator, integrates the difference, and generates a control voltage ($V_{Ctrl}$) to adjust the gain of VGA. A 0.5V/V voltage divider is needed to ensure a correct ALC loop operation due to the control voltage limitation of VCA810. The $V_{Set}$ is generated by a reference voltage IC, LTC6655, and a tunable voltage divider.

There is usually an optimal drive signal ($V_{drv}$) amplitude for each gyroscope. If the amplitude is too small, the resulting smaller scale factor can degrade the signal to noise ratio and the Allan deviation performance. If the drive amplitude is too large, the MEMS device may operate in the nonlinear region and can introduce more flicker noise to the rate output and, hence, degrades the bias instability. The optimal drive amplitude for the z gyroscope is about 40mV to 70mV. The optimal drive amplitude for the x/y gyroscope is about 100mV to 150mV.

### *5.2.4 Sense Channel and Demodulator*

As shown in Figure 5.2, the sense (indirect) channel TIAs extract the amplitude-modulated (AM) rate signal from the sense electrodes. The AM rate signal is next multiplied by the drive signal using an analog multiplier to demodulate the baseband rate

signal. The Analog Device AD835 4-quadrant multiplier was chosen as the multiplier because it provides a high bandwidth and low noise. Two active phase shifters, similar to the one in the drive loop, are inserted between the drive TIAs' outputs and the multiplier's inputs. These two phase shifters compensate the phase difference between the sense TIAs and the drive TIAs, and also provide a four times of gain to boost the scale factor. The output of AD835 is then low-pass filtered to remove the out-of-band noise. Figure 5.11 shows the complete schematic of the low-pass filter, which consists of a passive 1st-order LPF and a 2nd-order Sallen-Key filter. The -3dB bandwidth is 100Hz.

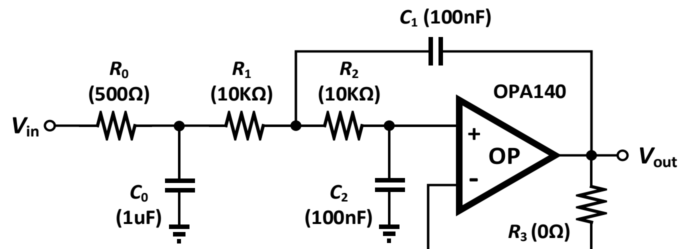


**Figure 5.11**: The complete schematic of the 3rd-order low-pass filter for the analog demodulator output. It consists of a passive 1st-order LPF and a 2nd-order Sallen-Key filter. The -3dB bandwidth is 100Hz.

### *5.2.5 Oven Control Loop*

Figure 5.12 shows the detailed schematic of the oven control loop for this TIMU die. The oven control loop is similar to the one used in Chapter 3. The structural resistance ($R_{Struc}$) of the resonator is used as the temperature sensor. The discrete low TCR reference resistor ($R_{REF}$) is chosen so that the temperature of $R_{Struc}$ is stabilized at 80°C. In this design, there are two symmetric heaters sitting beside the resonator.

The heater amplifier in Chapter 3 uses AD8397 because it provides a maximum output current of 300mA and a maximum output voltage range of ±11V. However, the noise and temperature drift performance of AD8397 are not good. Here, we chose ADA4522 instead

because it has low flicker noise (117nVp-p), low temperature-induced offset drift (2.5nV/°C), and high output voltage range (±25V). The only minor drawback of ADA4522 is that the maximum output current is 14mA. This minor drawback can be overcome by combining four amplifiers in parallel as shown in Figure 5.12(b). A 10Ω resistor is inserted at each amplifier's output to prevent large short circuit current.

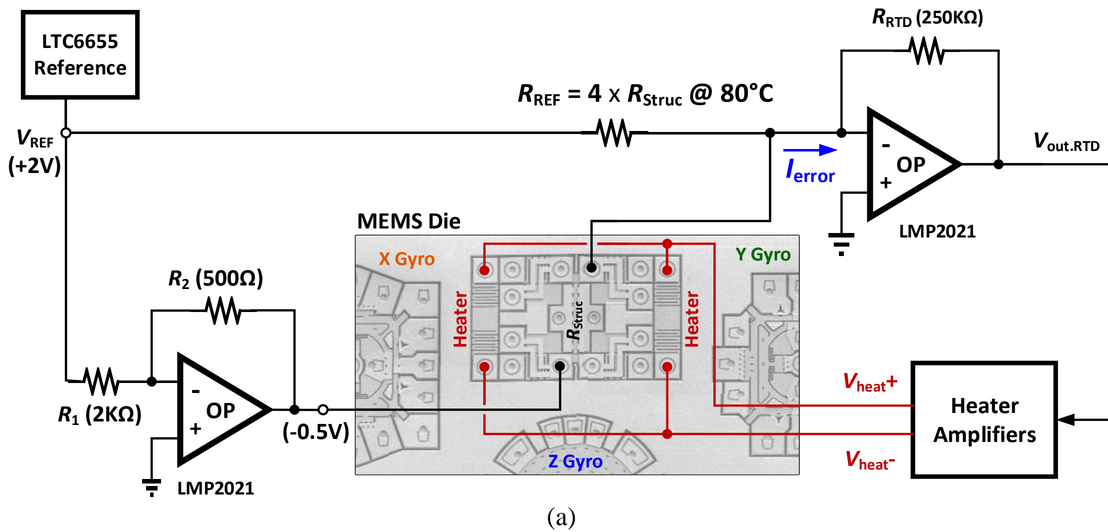


(a)

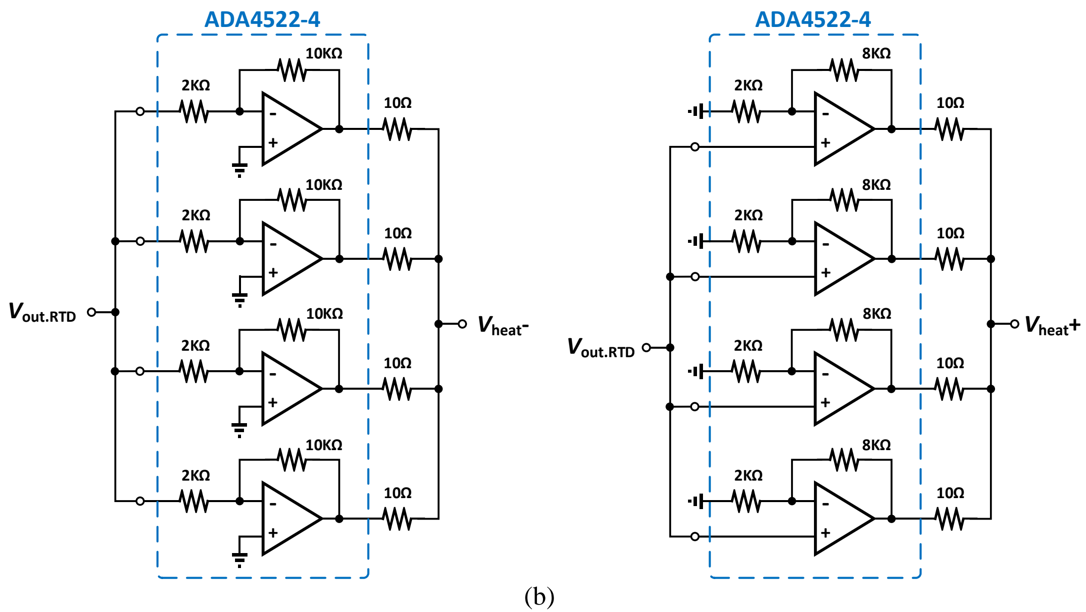


(b)

**Figure 5.12**: (a) The schematic of the oven control loop; (b) The proposed low-noise low-drift inverting (left) and non-inverting (right) heater amplifiers using ADA4522.

*5.2.6 PCB Layout Floor Plan*

In order to put all the interface circuits for six-degree-of-freedom IMU and the oven control circuit on a hand-held sized board, the layout must be carefully planned. Figure 5.13 shows the layout floor plan of the prototype TIMU board. On the top side, each axis of gyroscope occupies a quarter of the board area, which includes the four TIAs, the drive loop, and the demodulator. The three accelerometer interface ICs (AD7746 capacitance-to-digital converter), the heater amplifiers and the connection headers occupy the rest of the board. On the back side, there are the feedthrough cancellation amplifiers, $V_{REF}$ generator (1.25V) for the ALC, and the 3rd-order low-pass filter for each gyroscope. The $V_{REF}$ generator (2V), reference resistor ($R_{REF}$) and the resistance temperature detector (RTD) are put on the back side in order to shorten the parasitic resistance between the resonator $R_{Struc}$ and the RTD. MMCX connectors are used here instead of the SMA connectors for a much smaller footprint. The board dimension is 3.5 inches by 3.5 inches.

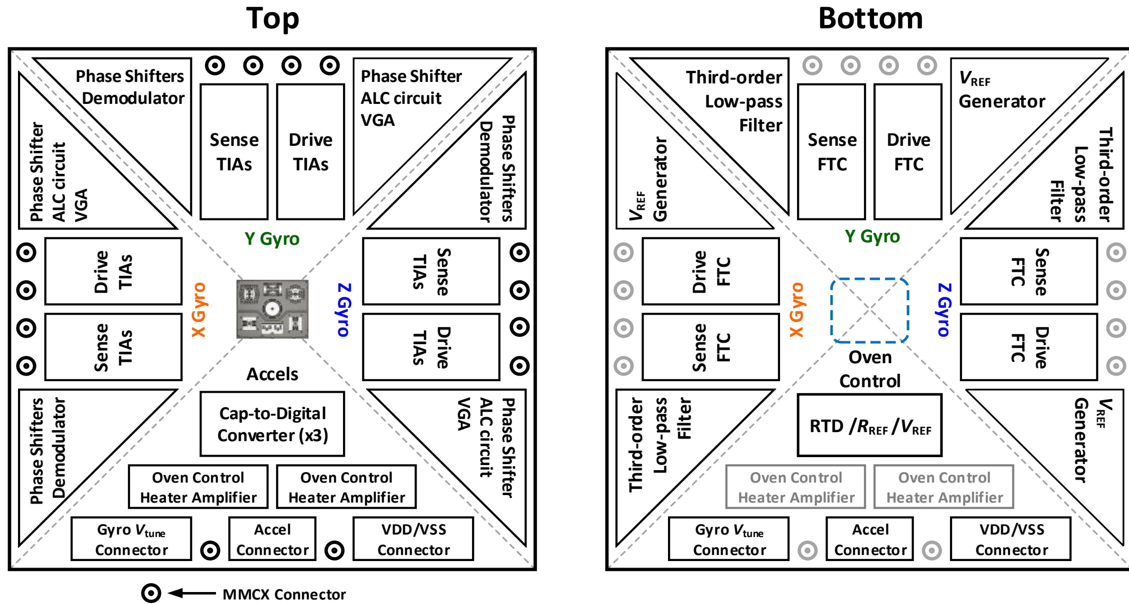


**Figure 5.13**: The layout floor plan of the 6-DoF TIMU prototype board. (Dimension = 3.5-inch x 3.5-inch)

Figure 5.14(a) shows the photograph of the TIMU prototype board. Because the MEMS die has so many pads that need to be wire bonded to the PCB, a transposer board is needed for the following purposes:

1) minimize the parasitic resistance in series with the structural resistor ($R_{\text{Struc}}$)
2) minimize the feedthrough capacitance of each gyroscope
3) enhance the isolation of ac signals between different gyroscopes
4) pre-route the signal traces to a proper location to simplify the signal/power traces routing on the main board

Figure 5.14(b) shows the picture of the interposer board. This small board is 0.031-inch-thick and has four layers.

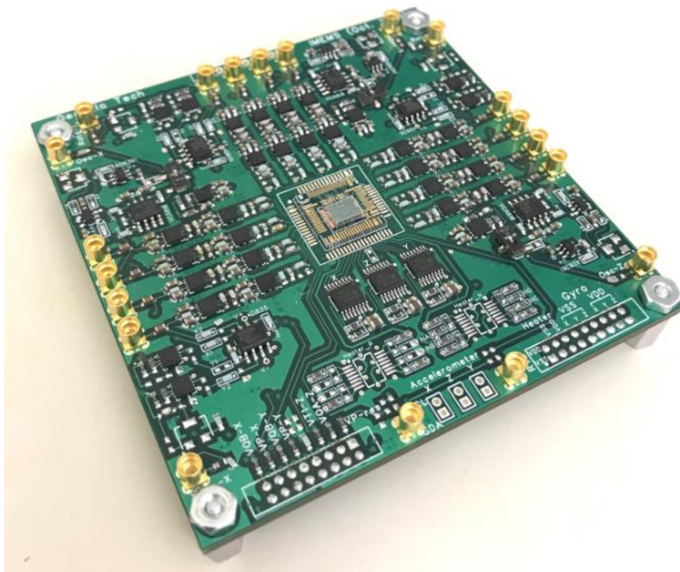

(a)

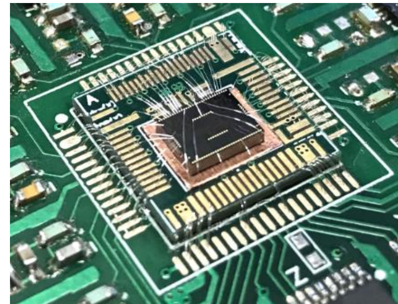

(b)

**Figure 5.14**: (a) The photograph of the prototype TIMU board, and (b) the zoomed in view for the interposer board and the TIMU die.

## 5.3 Gyroscopes Measurement Results

### *5.3.1 Scale Factor and Allan Deviation*

Figure 5.15 shows the transient rate output of all 3-axis gyroscopes operating simultaneously (rotated by hands). This is the first demonstration of three high-frequency mode-matched vibratory gyroscopes integrated on the same die. The scale factors of the x, y, and z gyroscopes are 440uV/°/s, 330uV/°/s, and 400uV/°/s, respectively. Although the sense mode quality factor $Q$ (4.5k) of the x/y is much lower than the $Q$ (180k) of z gyro, the proposed LP-HP TIA can compensate the lower device scale factor by providing a higher TIA gain, which makes the overall scale factors (device + electronics) of the all 3-axis gyros similar.

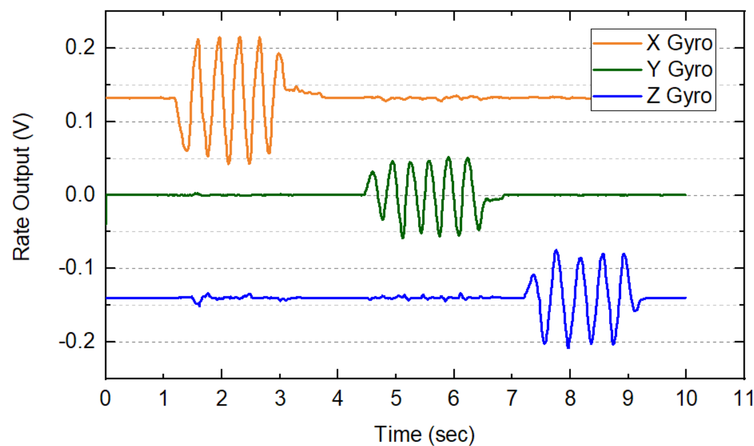


**Figure 5.15**: Transient waveform of the simultaneous operation of all 3-axis gyroscopes (rotated by hands)

Figure 5.16, 5.17 and 5.18 show the measured Allan deviation (ADEV) of all three axes gyroscopes. The blue line is the result of using the on-board drive loop and analog demodulator. The analog rate output was recorded by a National Instrument NI-9238 data acquisition system, which has a low input noise of 3.9uVrms and sampling rate up to 50kSa/sec. The orange line is the result of using a Zurich Instrument HF2LI lock-in amplifier to form the drive loop and to demodulate the rate signal in digital domain. When

the gyros were measured with the lock-in amplifier, the only analog components used are the four TIAs. The four TIA outputs are digitized by four ADCs in the lock-in amplifier. The lock-in amplifier fed back a drive signal through a digital-to-analog converter (DAC) to gyro's drive voltage buffer to form the drive loop. The demodulation process is all done in the digital domain of the lock-in amplifier. The lock-in amplifier ADEV result is better than the on-board demodulator ADEV result mainly because the analog multiplier (AD835) has larger temperature drift and noise while the demodulator in the lock-in amplifier is purely digital so didn't add any noise or temperature effect to the demodulation process. The performances of all three axes gyroscopes are summarized in Table 5-2.

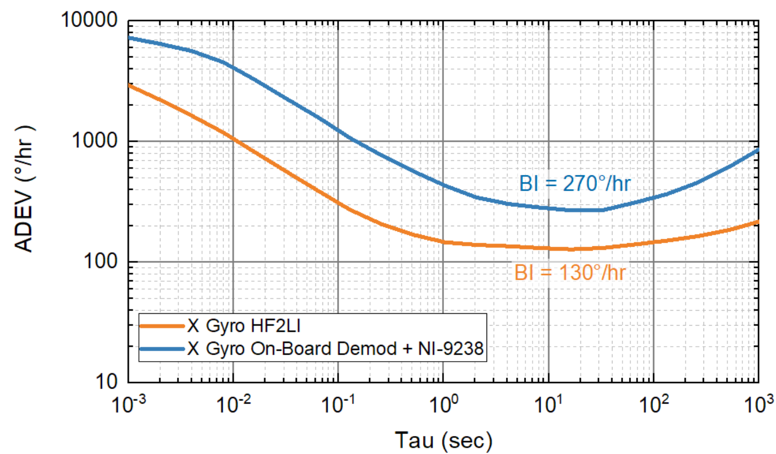


**Figure 5.16**: Measured Allan deviation of x-axis gyroscope without ovenization

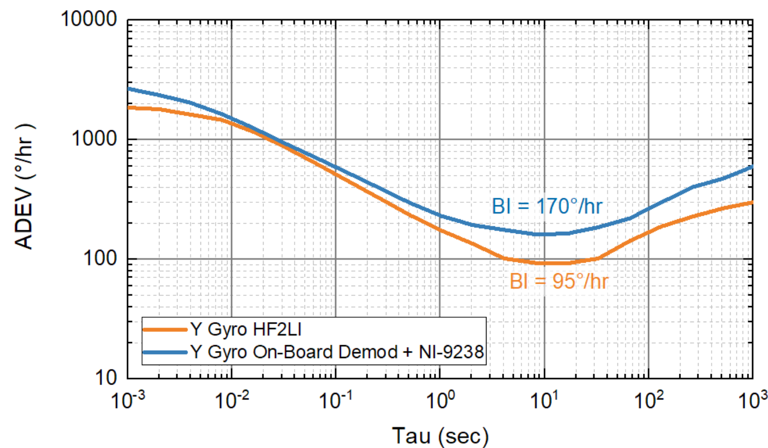


**Figure 5.17**: Measured Allan deviation of y-axis gyroscope without ovenization

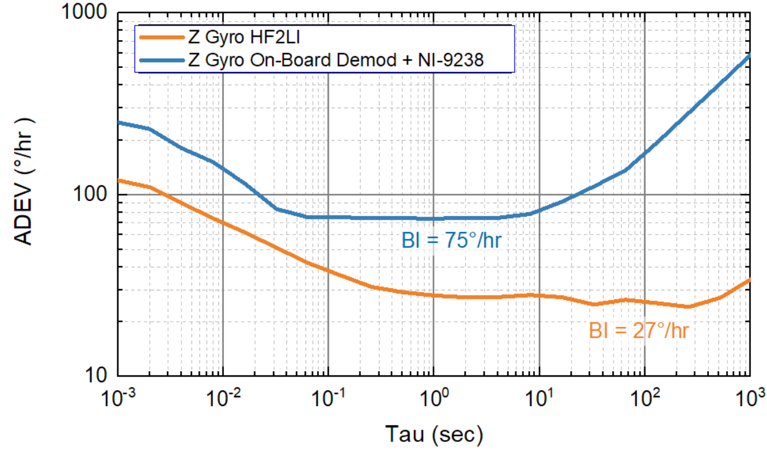

**Figure 5.18**: Measured Allan deviation of z-axis gyroscope without ovenization

Table 5-2
Performance Summary of All 3 Axes Gyroscopes

| | | X Gyro | Y Gyro | Z Gyro |
|---|---|---|---|---|
| Gyro op. frequency (MHz) | | 0.7 | 0.66 | 5.4 |
| Scale Factor (μV/°/s) | | 440 | 330 | 400 |
| ARW (°/$\sqrt{Hr}$) | HF2LI | 2.3 | 2.8 | 0.5 |
| | On-Board Demod. | 6.9 | 3.8 | 1.2 |
| Bias Instability (°/Hr) | HF2LI | 130 | 95 | 27 |
| | On-Board Demod. | 270 | 170 | 75 |

### *5.3.2 Cross-Axis Sensitivity*

One major advantage of integrating all 3-axis gyroscopes on the same die is the low cross-axis sensitivity. The cross-axis sensitivity is the detected rate (°/s) from one axis of gyro divided by the actual rotation rate about another (orthogonal) axis. The cross-axis sensitivity can be expressed as the following equation.

$$\text{Cross-Axis Sensitivity} = \frac{\Omega_{detecting-axis}}{\Omega_{rotating-axis}} = \frac{\left({}^{V_{out}}/_{SF}\right)_{detecting-axis}}{\Omega_{rotating-axis}} \qquad (5.7)$$

(detecting axis ⊥ rotating axis)

Where Ω is the rotation rate (°/s), $V_{out}$ (volt) is the output voltage of the demodulated rate signal, and SF is the scale factor of the gyro with a unit of V/°/s. The detecting axis is perpendicular (90°) to the rotating axis.

Unlike putting three identical but separated gyroscope dies orthogonally in the same package, which needs extremely accurate alignment, this integrated single-chip IMU naturally guarantees almost perfect orthogonal orientation between different axes. Figure 5.19 shows an example of cross-axis sensitivity measurement. Here we apply a 2Hz, 80°/s (pk-pk) sinusoidal rotation to the y axis and measure the rate output from the z gyroscope. The time domain rate output in Figure 5.19(a) is so small that it is buried by the random noise and can not be visually inspected. By doing an FFT analysis to the time domain waveform, now the cross-axis rotation signal can be extracted.

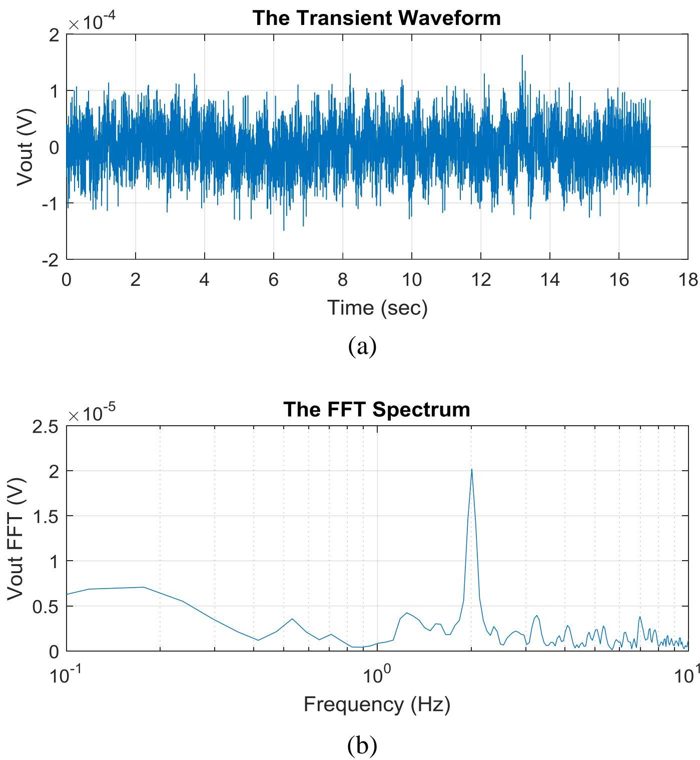


**Figure 5.19**: An example of cross-axis sensitivity measurement. The applied sinusoidal (2Hz) rotation has a rate amplitude of 40°/s. (a) The recorded gyro demodulator output in time domain. The cross-axis rotation signal cannot be visually inspected. (b) By doing an FFT analysis to the waveform in (a), the cross-axis rotation signal can be extracted.

Table 5-3 summarizes the complete gyro cross-axis sensitivity performance of this IMU. The worst-case cross-axis sensitivity is 1.3%. These results can potentially be improved by more accurate board orientation and alignment.

Table 5-3
Measured Cross-Axis Sensitivity of All Three Axes Gyroscopes

| Rotation Axis | Detecting Axis | Cross-Axis Sensitivity (%) |
|---|---|---|
| X | Y | 1.1 |
| X | Z | 0.3 |
| Y | X | 1.0 |
| Y | Z | 0.8 |
| Z | X | 1.3 |
| Z | Y | 0.9 |

### *5.3.3 Ovenization on Gyroscopes*

Figure 5.20 shows the frequency stability of the y-axis gyro, z-axis gyro, and the timing resonator when the ovenization function is turned on. The micro-oven temperature is set to 80°C and the ambient temperature changes from -10°C to 70°C. The ovenized frequency stability of the timing resonator is about ±2.5ppm. The y and z gyro show a larger frequency variation of ±20ppm from -10°C to 70°C. This is mainly because the heaters are not placed symmetrically around each gyro, which causes temperature gradient on the devices. Consider the measured TCF of -27ppm/°C, the frequency stabilities of resonator and gyros are improved by 432 times and 54 times, respectively.

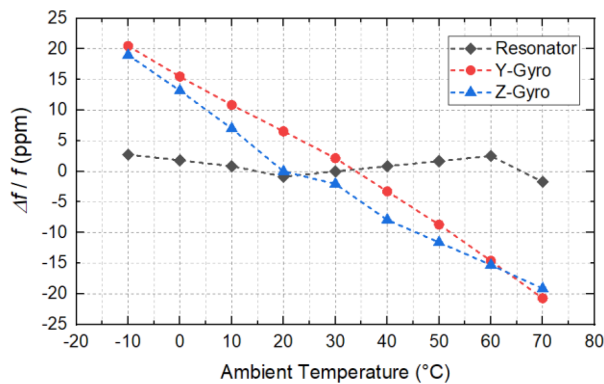


**Figure 5.20**: The ovenized frequency stabilities of the timing resonator, y-axis gyro and z-axis gyro

Figure 5.21 shows the y-axis gyro scale factor variation at different ambient temperatures (-10°C to 70°C). Here we use the scale factors measured at 70°C as the reference points and plotted the scale factor variation accordingly. Without the automatic oven control, the scale factor variation of y gyro is about 150%. When the oven control loop is enabled, the variation was reduced to only 6.5%. The scale factor stability was improved by 23 times. The factors that contribute to the scale factor variation are the *Qs* and frequency split (Δ*f*) variation with temperature. The *Q*s of sense mode and drive mode decrease by about 30% from -10°C to 70°C [52], which can reduce the scale factor by half. The frequency split variation can be caused by TCF mismatch because the drive and sense modes have different mode shapes. So that the Δ*f* can also change with temperature.

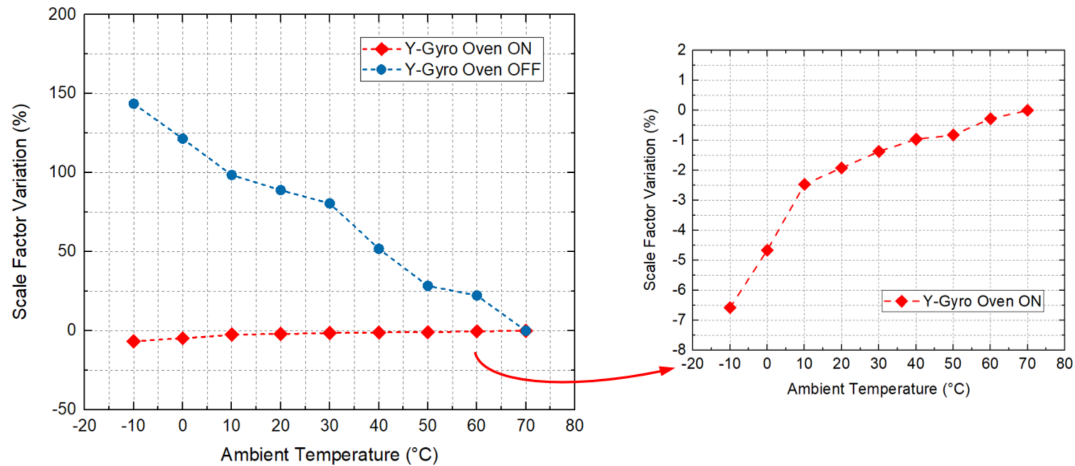


**Figure 5.21**: (Left) The scale factor variation of the y-axis gyroscope with and without ovenization, and (right) the zoomed-in view of the scale factor variation with ovenization.

Figure 5.22 shows the y-axis gyro output bias variation at different ambient temperatures (-10°C to 70°C). Without the automatic oven control, the bias variation of y gyro is about 50%. When the oven control loop is enabled, the variation was reduced to only 1%. The output bias stability was improved by 50 times. The factors that contribute to the bias variation are the feedthrough and frequency split variation with temperature.

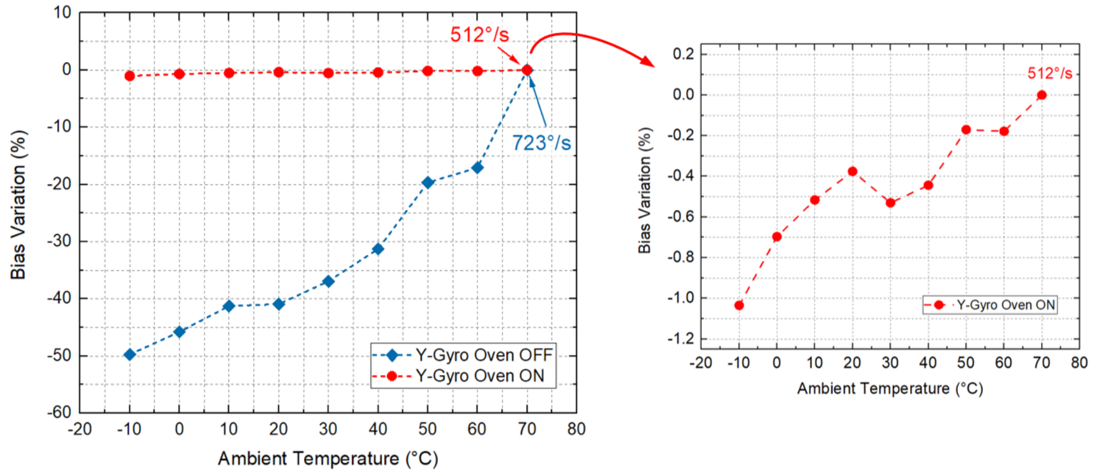


**Figure 5.22**: (Left) The bias variation of the y-axis gyroscope with and without ovenization, and (right) the zoomed-in view of the bias variation with ovenization.

The ADEV measurement comparison of the y gyro is plotted in Figure 5.23. The measured bias instabilities (BI) are 114°/hr and 140°/hr, respectively when the oven control was off (room temperature) and on. Note that the BI value (without ovenization) is slightly different from the previous result in Figure 5.16 because a different device on a different board was used. When the oven control is turned on, the entire ADEV curve goes up. One possible reason is because the scale factor is smaller when the device is ovenized at 80°C. The higher temperature also makes the device Brownian noise higher.

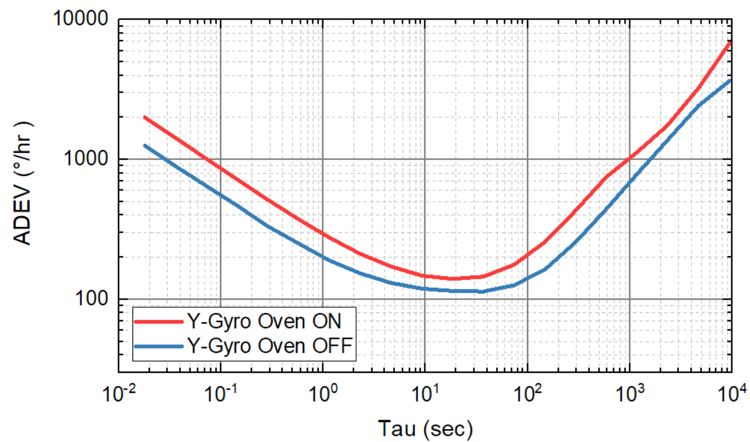


**Figure 5.23**: The ADEV of the y-axis gyroscope with and without ovenization (12 hours, $\tau_0$ = 0.018 sec). Without ovenization (room temperature), the bias instability is 114°/hour. With ovenization, the bias instability is 140°/hour.

Figure 5.24 shows the z-axis gyro scale factor variation at different ambient temperatures (-10°C to 70°C). The scale factors measured at 70°C are used as the reference points. Without the automatic oven control, the scale factor variation of z gyro is about 70%. When the oven control loop is enabled, the variation was reduced to only 0.3%. The scale factor stability was improved by 233 times. The factors that contribute to the scale factor variation are the *Qs* and frequency split variation with temperature. The measured *Q*s of the sense and drive modes decrease by about 24% from -10°C to 70°C, as shown in Figure 5.23. The frequency split can also change but was not characterized.

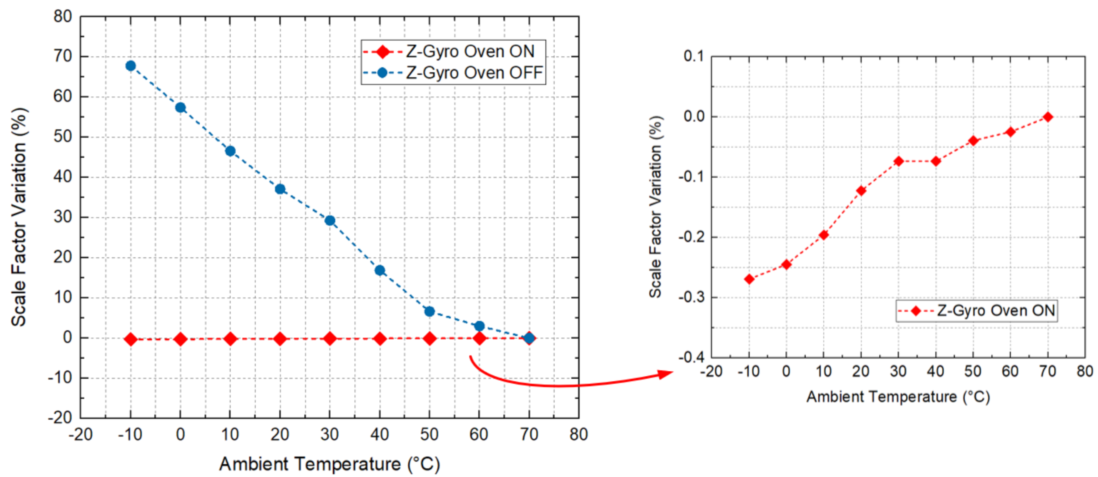


**Figure 5.24**: (Left) The scale factor variation of the z-axis gyroscope with and without ovenization, and (right) the zoomed-in view of the scale factor variation with ovenization.

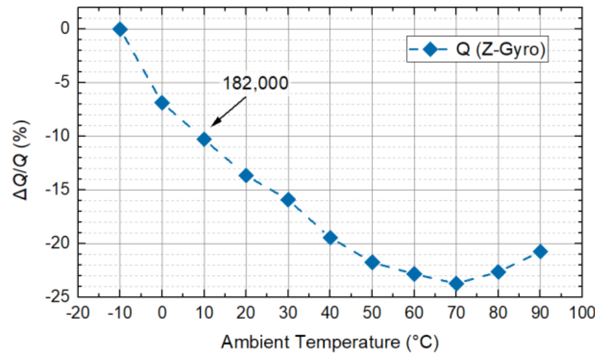


**Figure 5.25**: The measure z-axis gyro quality factor (*Q*) variation v.s. ambient temperature

Figure 5.26 shows the z-axis gyro output bias variation at different ambient temperatures (-10°C to 70°C). When the oven control is off, the bias variation of z gyro is about 170%. When the oven control loop is enabled, the variation decreases slightly to 110%. There is no significant improvement probably because the drive and sense mode shapes are the same so the TCF mismatch is minuscule, which makes the frequency split factor nondominant.

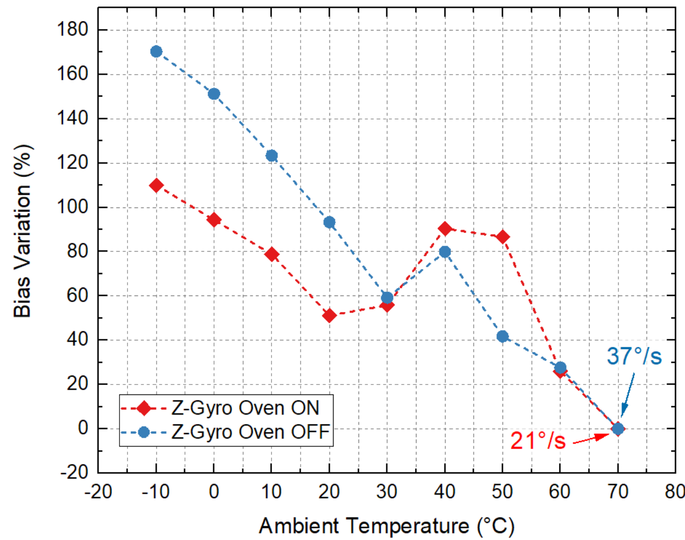


**Figure 5.26**: (Left) The bias variation of the z-axis gyroscope with and without ovenization, and (right) the zoomed-in view of the bias variation with ovenization.

The ADEV measurement comparison of the z gyro is plotted in Figure 5.25. The measured bias instabilities (BI) are 9°/hr and 12°/hr, respectively when the oven control was off (room temperature) and on. Note that the BI value (without ovenization) is different from the previous result in Figure 5.17 because a different device on a different board was used. When the oven control is on, the entire ADEV curve goes up. One possible reason is because the scale factor is smaller when the device is ovenized at 80°C. The higher temperature also makes the device Brownian noise higher.

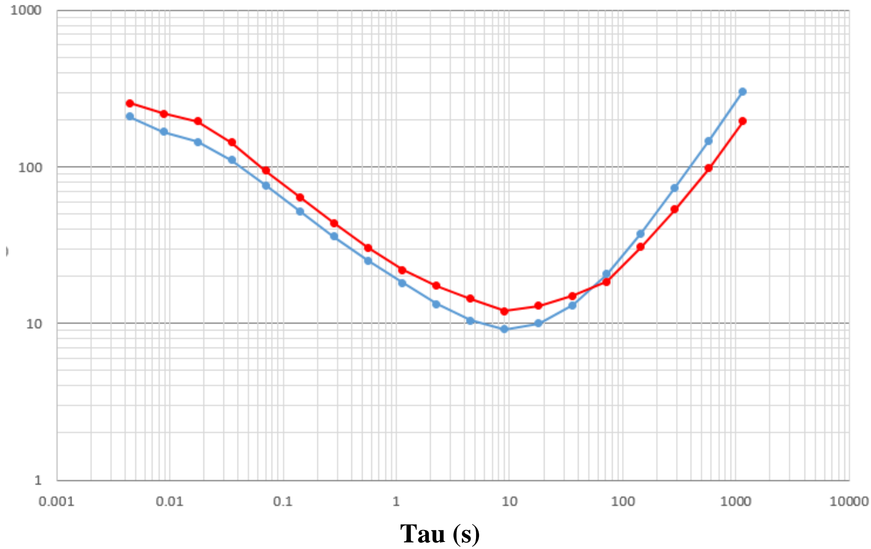


**Figure 5.27**: The ADEV of the z-axis gyroscope with and without ovenization (2 hours, $\tau_0$ = 0.018 sec). Without ovenization, the bias instability is 9°/hour. With ovenization, the bias instability is 12°/hour.

### *5.3.4 The TCR Measurement*

An interesting observation is that the measured TCR shows a turn-over point at about 35°C (Figure 5.28). Twelve devices were tested and all of them showed a turn-over point at the same temperature. This TCR turn-over point might be due to the bulk charge Coulombic scattering effect on silicon's mobility. The resistivity of silicon is inversely proportional to the carrier mobility and can be expressed as

$$\rho = \frac{1}{\sigma} = \frac{1}{q(\mu_n n + \mu_p p)} \tag{5.8}$$

where $\rho$ is the resistivity (Ω-cm), $q$ is the carrier charge, *n*/*p* represents the carrier concentration, $\mu_n/\mu_p$ is the mobility of the p-type and n-type carrier. The total equivalent mobility ($\mu_n$ or $\mu_p$) is a combined effect of phonon scattering, surface roughness scattering, bulk Coulombic scattering, interface charge Coulombic scattering and other scattering effects. The bulk Coulombic scattering causes mobility to decrease as temperature decreases ($\mu_{cb} \propto T$) because at low temperatures, electrons move slower, and lattice vibrations are

small as well. Thus, the ion impurity forces which have little impact on high-energy particles become the dominant limit to mobility. In this regime, decreasing temperature extends the amount of time electrons spend passing an impurity ion, causing mobility to decrease [53, 54].

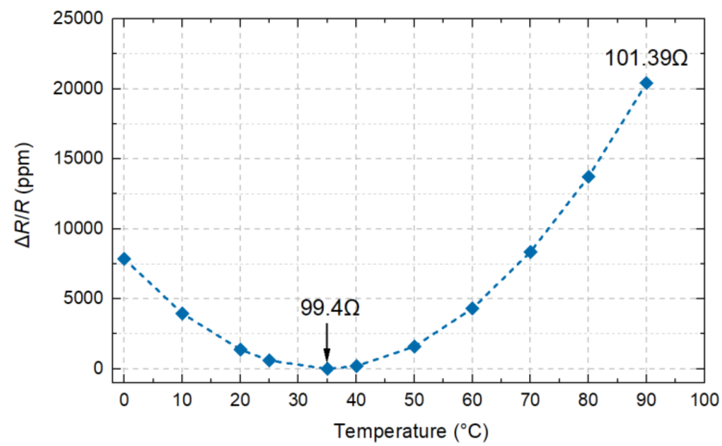


**Figure 5.28**: The measured TCR of the $R_{Struc}$ on this TIMU die. The TCR shows a turnover point at around 35°C. Twelve devices were tested and all of them showed a turn-over point at the same temperature.

# CHAPTER 6

# AC HEATING SCHEME FOR LOWER POWER $R_{Struc}$-BASED TEMPERATURE SENSING MEMS OCXO

This chapter introduces the design and implementation of a new AC heating scheme for a $R_{Struc}$-based temperature sensing MEMS OCXO. The first section will discuss the reason of high-power consumption of the MEMS OCXO in chapter 3. The second section will talk about the solution to reduce power consumption and its limitation. A new heating scheme using AC current will be introduced to resolve the limitation

## 6.1 The Power Consumption of MEMS OCXO

The MEMS OCXO demonstrated in chapter 3 consumes a power of 380mW at the lowest ambient temperature of -25°C. Figure 6.1a shows the thermal simulation result of the resonator heated up to 80°C. Figure 6.1b illustrates the main heat transfer path and the main heat dissipation path. The heat generated by the silicon heater passes through the thin $SiO_2$ layer (2µm), reaches the silicon substrate, penetrates the SiO2 layer under the resonator and then arrives at the resonator. A lot of thermal energy is dissipated through the substrate to the printed circuit board and then to the ambience. Although $SiO_2$ has a much higher thermal resistivity than silicon, the $SiO_2$ layer here is too thin (L, W, H = 120µm, 120um, 2um) to provide a large enough thermal resistance. The heating efficiency of this separated heater is 3.3mW/°C.

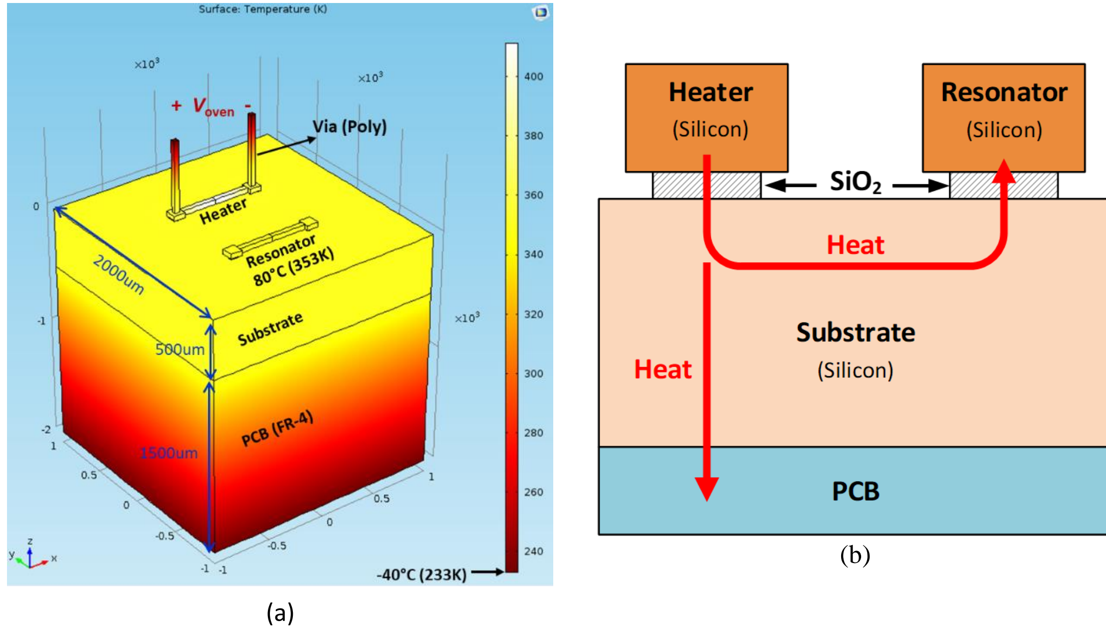


**Figure 6.1:** (a) The thermal simulation (Comsol) of the MEMS device used in chapter 3 with resonator heated up to 80°C. (b) The illustration of the main heat transfer path and the main heat dissipation path.

## 6.2 Reduce Heater Power Consumption

To reduce the micro-oven power consumption, two things need to be accomplished. The first thing is to minimize thermal resistance ($R_{\text{therm}}$) between the heater and the resonator. The second task is to maximize the thermal resistance between the resonator and the ambience. Figure 6.2 shows how to properly merge the heater with the resonator to minimize the $R_{\text{therm}}$ between them. The direction of heating currents must be perpendicular to the temperature sensing current ($V_{\text{REF}}/R_{\text{Struc}}$) to ensure a uniform temperature distribution for the resonator. Figure 6.2b shows the SEM of a MEMS device fabricated at Georgia Tech (by Anosh Daruwalla), the area of the $SiO_2$ layer under the resonator posts was also reduced by two times. This new design demonstrates a heating efficiency of 2mW/°C with the separated heater, and a heating efficiency of 1.1mW/°C with the merged heaters.

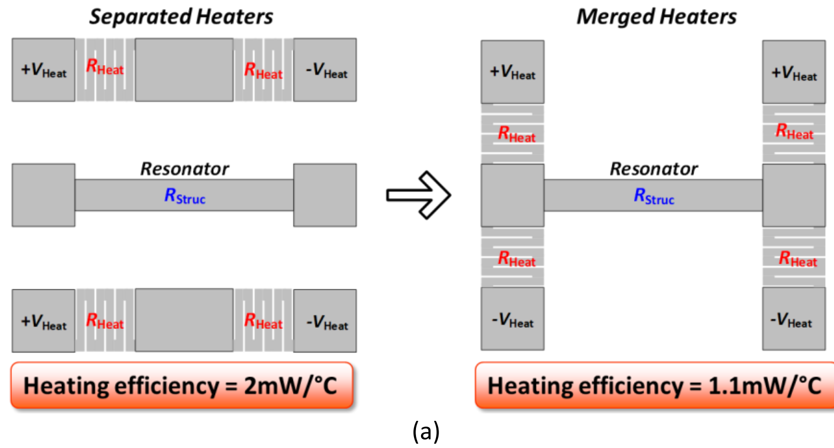


(a)

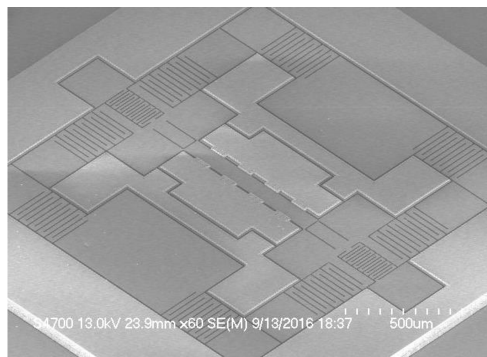


(b)

**Figure 6.2** (a) Merge the heater with the resonator (and the $R_{struc}$ temperature sensor). (b) The SEM of a MEMS device fabricated in Georgia Tech, which shows a heating efficiency of 2mW/°C with separated heater, and a heating efficiency of 1.1mW/°C with merged heaters. The MEMS device was fabricated by Anosh Daruwalla.

Although merging the heaters and resonator can reduce thermal resistance, the mismatch of the heater resistor can degrade the temperature sensor accuracy. Figure 6.3 shows the equivalent circuit schematic with only one branch of the heaters for simplicity. If there is no mismatch, the RTD output voltage equals to the wanted value $V_{REF}/R_{Struc}$, which represents the temperature information. If there exists a mismatch of $\Delta R$ between two heater resistors, an error term shows up. Unfortunately, both the temperature information term and mismatch error term are in the low frequency band, hence, cannot be separated by filtering. Just 1% of mismatch can degrade the temperature sensor accuracy significantly or even make the oven control loop fail.

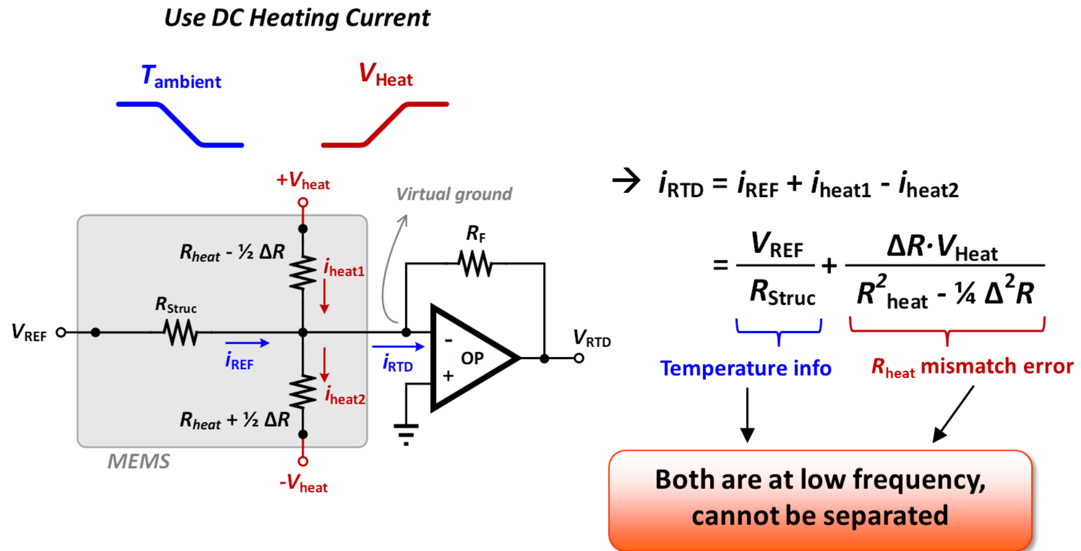


**Figure 6.3** Illustration of how the heater resistance mismatch can degrade the temperature sensor accuracy (only show one branch of the heaters for simplicity)

To eliminate this heater mismatch induced error, an AC heating method is proposed here. Figure 6.4 shows the concept of this AC heating scheme. The original DC heating voltage ($V_{heat}$) is now replaced by a sinusoidal signal with a rms amplitude equals to $V_{heat}$. The derivation in Figure 6.4 shows that the mismatch error term is modulated to the frequency $\omega$. If the modulation frequency is high enough, the mismatch error can be easily eliminated by low-pass filtering.

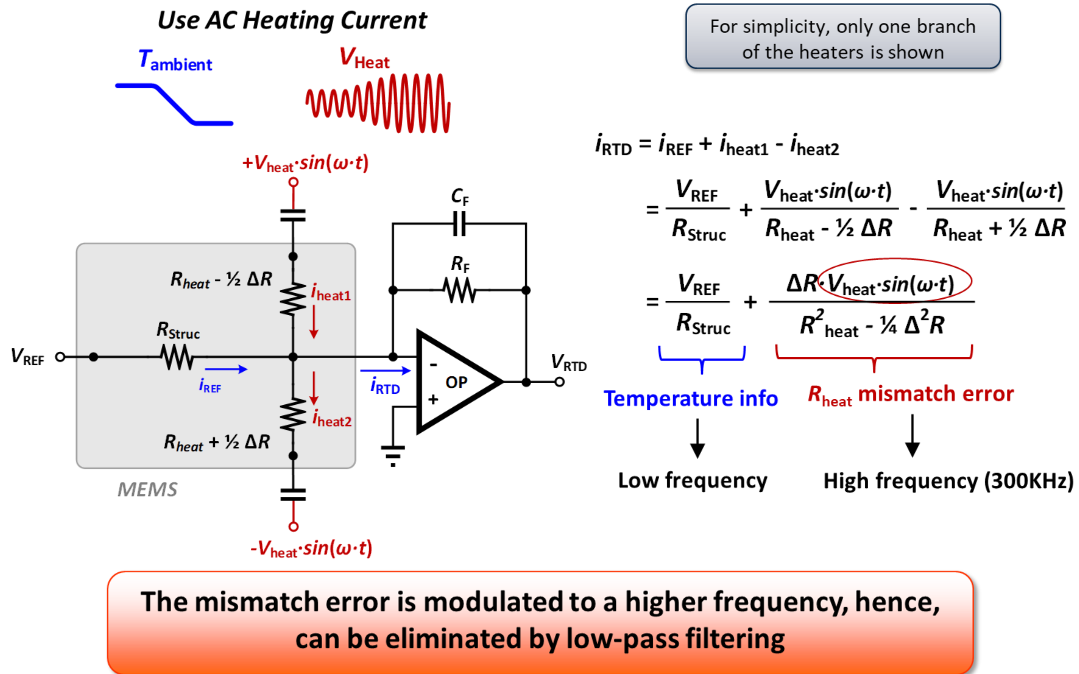


$$i_{RTD} = i_{REF} + i_{heat1} - i_{heat2} = \frac{V_{REF}}{R_{Struc}} + \frac{V_{heat} \cdot sin(\omega \cdot t)}{R_{heat} - \frac{1}{2}\Delta R} - \frac{V_{heat} \cdot sin(\omega \cdot t)}{R_{heat} + \frac{1}{2}\Delta R} = \frac{V_{REF}}{R_{Struc}} + \frac{\Delta R \cdot V_{heat} \cdot sin(\omega \cdot t)}{R^2_{heat} - \frac{1}{4}\Delta^2 R}$$

**Figure 6.4** The heater resistance mismatch is modulated to higher frequency by using AC heating voltages/currents. The modulated mismatch error can be low-pass filtered easily. (only show one branch of the heaters for simplicity)

Figure 6.5 shows the complete implementation of the AC heating oven control loop. Compared to the DC heating oven control loop in chapter 3, a second-order low-pass filter, a linear-in-magnitude variable gain amplifier, and an auxiliary oscillator are added to the loop. The second-order low-pass filter is to filter out the modulated heater mismatch error. The variable gain amplifier is to convert the filtered RTD output to a sinusoidal wave with an amplitude proportional to $V_{RTD}$. The frequency of the auxiliary oscillator doesn't need to be temperature stable. The frequency can vary by 100% without affecting the oven control loop performance. In this design, the auxiliary oscillator provides a sinusoidal signal at 300KHz with an amplitude of 600mVp-p.

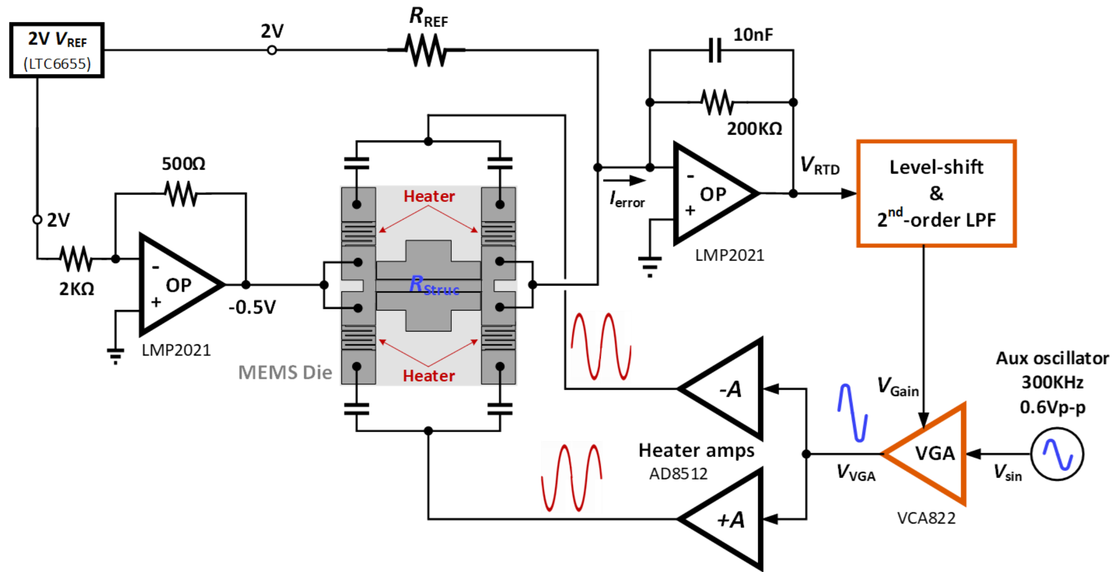


**Figure 6.5** The complete implementation of the AC heating oven control loop. The orange blocks convert the RTD output voltage into a sinusoidal wave with a rms amplitude equal to $V_{RTD}$.

Figure 6.6 show the measured resonance frequency stability (S21) of the ovenized resonator with the proposed AC heating scheme. The nominal frequency is about 118MHz. The total frequency variation is 45ppm from 0°C to 70°C ambient temperature.

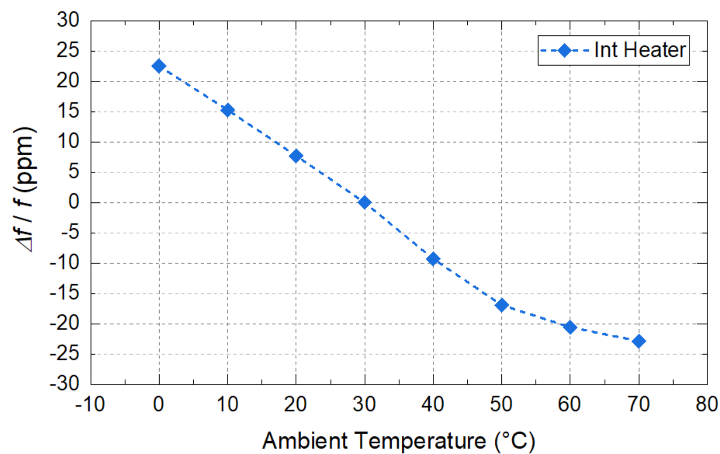


**Figure 6.6** Measured resonance frequency stability (S21) of the ovenized resonator with the proposed AC heating scheme. The result shows a total frequency variation of 45ppm from 0°C to 70°C.

This measured frequency stability is not as good as the result in chapter 3. One major reason is the parasitic resistance of the through hole via ($R_{via}$) between the resonator post and the bonding pad. In Figure 6.7, $R_{via}$ exists between the joint of $R_{Struc}$ and $R_{heat}$, and the RTD input. Even without $R_{heat}$ mismatch, the $R_{via}$ can still cause temperature sensing error. This can be explained by the $i_{RTD}$ equation below.

$$i_{RTD} = \frac{V_{REF}}{R_{Struc}} \times \frac{1}{1 + \left(\frac{2}{R_{heat}} + \frac{1}{R_{Struc}}\right) R_{via}} \tag{6.1}$$

Four-point resistance measurement method can be one possible solution to extract $R_{Struc}$ without the parasitic resistance effect. Further investigation is needed to identify other error sources.

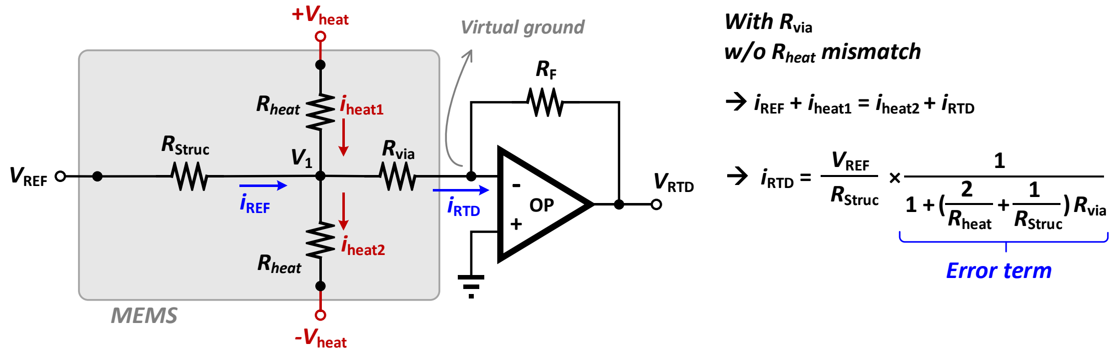


**Figure 6.7** The parasitic $R_{via}$ between the joint of $R_{Struc}$ and $R_{heat}$, and the RTD input is one major cause of the larger (45ppm) frequency variation.

In summary, the proposed AC heating scheme enables the integration of the resonator, temperature sensor ($R_{struc}$) and heaters. This technique not only minimizes the thermal resistance but also avoid the need to use composite material [30, 55] for the resistive temperature, which realized a single device using pure silicon.

# CHAPTER 7

# CONCLUSION AND FUTURE WORK

This dissertation presents a new system architecture for MEMS oven-controlled oscillator, which includes self-temperature sensing, automatic temperature control and digital calibration. The measurement results clearly show high frequency stability, high frequency stability improving factor, and low long-term drift. The same temperature stabilization technique was also applied to MEMS vibratory gyroscopes. The scale factor and ZRO variations were significantly reduced, which enables a high stability navigation system. This chapter presents a summary of the contributions of this research, followed by future directions towards part-per-billion stability MEMS OCXO and higher performance MEMS vibratory gyroscope interfaces.

## 7.1 Contributions

The major technical contributions of this work are summarized as follows:

1) For the first time, an automatic analog micro-oven control scheme for a MEMS OCXO using structural resistance-based temperature sensing was demonstrated. The analog feedback loop showed high efficiency in improving the frequency stability by ~600X.
2) In addition to the analog oven control scheme, a feedforward digital calibration was developed to further calibrate out the residue frequency error. This calibration scheme is simple and efficient that it improved the frequency stability by another 10X and worked well under dynamically varying temperature situation as well.

3) An AC heating scheme is proposed to integrate the heater into the resonator (and $R_{struc}$ temperature sensor). The first advantage is that this method can minimizes the thermal resistance between the resonator and the heaters to reduce oven power consumption. The second advantage is that there is no need to use composite material to implement the temperature sensor, which can realize a pure silicon device containing integrated resonator, temperature sensor, and heater.
4) A LP-HP transimpedance amplifier architecture is proposed, which can minimize the $R_F$-related noise and increase the TIA gain without any bandwidth penalty. The key feature of this architecture is that it greatly relaxes the direct tradeoff between the gain (i.e. $R_F$ noise) and the input-referred noise in the conventional single-stage TIA. This new TIA architecture is beneficial to gyro performance in two aspects.
    - It improves the phase noise in the drive loop.
    - It increases the overall scale factor by increasing the sense channel TIA gain, which is especially beneficial for high-frequency gyroscopes.
5) For the first time, the simultaneous operation of three axes MEMS vibratory gyroscopes and a timing resonator on a single chip was demonstrated. A six-degree-of-freedom TIMU interface prototype board was implemented with off-the-shelf electronic components. The micro-oven control loop was also included.
6) For the first time, an ovenized three axes gyro platform with integrated temperature sensor and heater (on the same die) was reported. It was also the first time that a mode-matched out-of-plane MEMS vibratory gyroscope was ovenized and characterized. The scale factor and ZRO showed much less variation across an 80°C ambient temperature when ovenized, which demonstrates the efficiency of the proposed ovenization scheme.

## 7.2 Future Work

For the $R_{struc}$-based MEMS OCXO, the frequency stability, phase noise, and power consumption are the three main aspects to improve. The suggested methods are listed below.

1) The TCF of MEMS resonator can be reduced by proper device engineering. The best scenario is to create a TCF turnover point at the target oven set-point. This turnover point provides a local zero-TCF region and can improve the overall OCXO frequency stability significantly.
2) We can use "4-point resistance measurement" to monitor the $R_{struc}$ value. It can eliminate the effect of parasitic resistance (from bonding wire and PCB trace) to improve the temperature sensing accuracy.
3) The low TCR reference resistor ($R_{REF}$) was implemented by a combination of discrete surface mount thin-film resisters. A better way to do so is to implement the $R_{REF}$ in an ASIC using a combination of resistors with opposite TCR polarities. So that the $R_{REF}$ occupies less board area and cost less.
4) The proposed digital calibration is based on tuning the phase of the sustaining amplifier. However, there is a drawback that if the oscillator doesn't lock at exact the resonance peak, the phase noise performance can degrade. It would be better to use a "resonance frequency tuning" mechanism for the digital calibration, like the dynamic frequency tuning method in [56].
5) The TIA used in this MEMS OCXO was designed for high frequency application, so the noise was not optimized. The close-in phase noise didn't show a comparable performance to those quartz OCXOs. The capacitor feedback TIA or the LP-HP TIA describe in chapter 4 can provide much lower thermal and flicker noise. An

ALC circuit should also be included to prevent the resonator from being driven into nonlinear region. It is better to implement the TIA, post-amplifier, and the ALC circuit all in an ASIC form than discrete electronics because it is easier to achieve a higher bandwidth due to less inter-stage parasitic capacitance.

6) Reducing the micro-oven power consumption is another important task. For the current device, the critical heat loss path starts from the resonator body, goes down through the 2μm-thick oxide (SiO2) layer underneath the resonator anchors, the silicon handle layer, then to the PCB. The major modification should focus on reducing the area of the oxide layer and shrinking the overall size of the MEMS die. This modification needs careful design and simulation to make sure reducing the power consumption doesn't compromise the resonator's performance.
7) Eventually, the grand goal is to implement all the circuits into an ASIC form and flip bonded with the MEMS device to achieve a minuscule form factor. A small form factor can also benefit the ovenization power consumption and the warm-up time. A short warm-up time can enable duty-cycling in a system as another option to reduce power consumption. And we want to ovenize the entire IC and MEMS package to eliminate any temperature-induced variation to achieve the best frequency stability.

For the TIMU interface circuit, the major problem is the large power consumption (700mA from ±3.6V). The large power consumption is mainly due to the high gyro operational frequency and the limited choices of high-speed commercial-off-the-shelf opamps. There are several things that we can do to mitigate this problem.

1) The ac signal traces on the device and on the PCB should be carefully planned and routed to minimize the capacitive feedthrough. If the feedthrough can be reduced

to a level that it doesn't affect the gyro performance, then the feedthrough cancellation circuits won't be needed. This can save about 15mA×12 = 180mA of current consumption for the entire TIMU.

2) The phase shifter of the drive loop can be merged into the second-stage of the TIA by adding a capacitor and a resistor to the positive input of the opamp. This can save about 15mA×3 = 45mA of current consumption.
3) The TIAs can be implemented in the ASIC form to save power because
    a. less parasitic capacitance presents in the main ac signal path so that less power is required to maintain a proper bandwidth
    b. there will be more design flexibility to use power efficient TIA architecture
    c. more advance technology node (shorter channel length) can be used to achieve the same bandwidth with less power consumption

The gyro performance (BI, ARW, and etc) using the on-board demodulator is not as good as using the HF2LI lock-in amplifier. There are two possible solutions.

4) The analog demodulator (AD835) is not temperature stable and not low noise, which limits the bias instability performance of the gyros. A possible better replacement could be a switch-based demodulator or a comparator-based (phase) demodulator [57].
5) Implementing high-speed and low-noise ADCs, digital demodulators, and digital low-pass filters all in an ASIC to avoid any circuit noise, temperature drift and nonlinearity in the demodulation process. A continuous-time band-pass sigma-delta ADC can be a low-power candidate.

To improve the ovenized performance of the gyros, two things can be done.

6) Use symmetric heater design for each gyro to minimize the temperature gradient problem to further improve the ovenized frequency stability.
7) Design integrated heater that connects to the gyro with very small thermal resistance to reduce power consumption.

The ultimate goal is to design an ASIC that includes all required functionality to interface the TIMU die with small form factor and low power consumption.

For the current TIMU board, one more thing can be done to make it more complete.

8) Implement a daughter board that has micro-controller, high-resolution digital-to-analog converters (DAC), and high-voltage buffers (ex: ADA4522-4) for all the gyro tuning voltages. The DC-DC converters (ex: LTM8045) and linear regulators (ex: TL1963A or LT3032) should also be included for the supply voltages. The suggested implementation is show in the figure below.

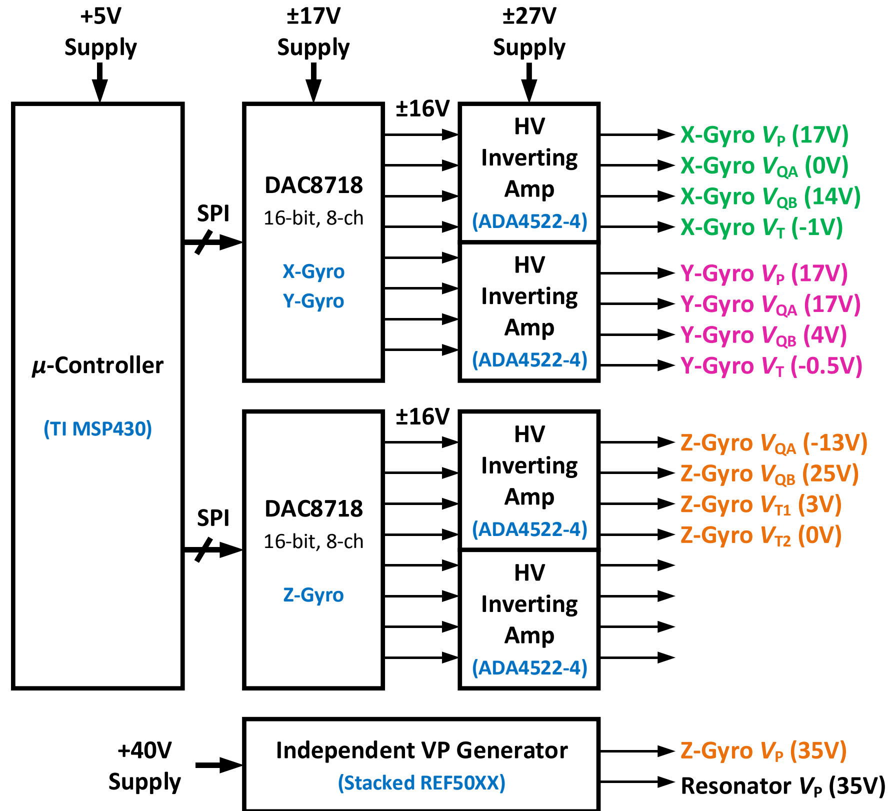


**Figure 7.1** The suggested TIMU daughter board implementation, which includes a micro-controller, high-resolution digital-to-analog converters (DAC), and high-voltage buffers for all the gyro tuning voltages. The DC-DC converters and linear regulators should also be included for the supply voltages.

# Appendix A. OSCILLATOR FREQUENCY DEVIATION

Unwanted phase shift from the sustaining amplifier can make the oscillator frequency deviates. For the same phase shift ($\Delta\Phi$), a higher $Q$ results in a smaller frequency deviation ($\Delta f$).

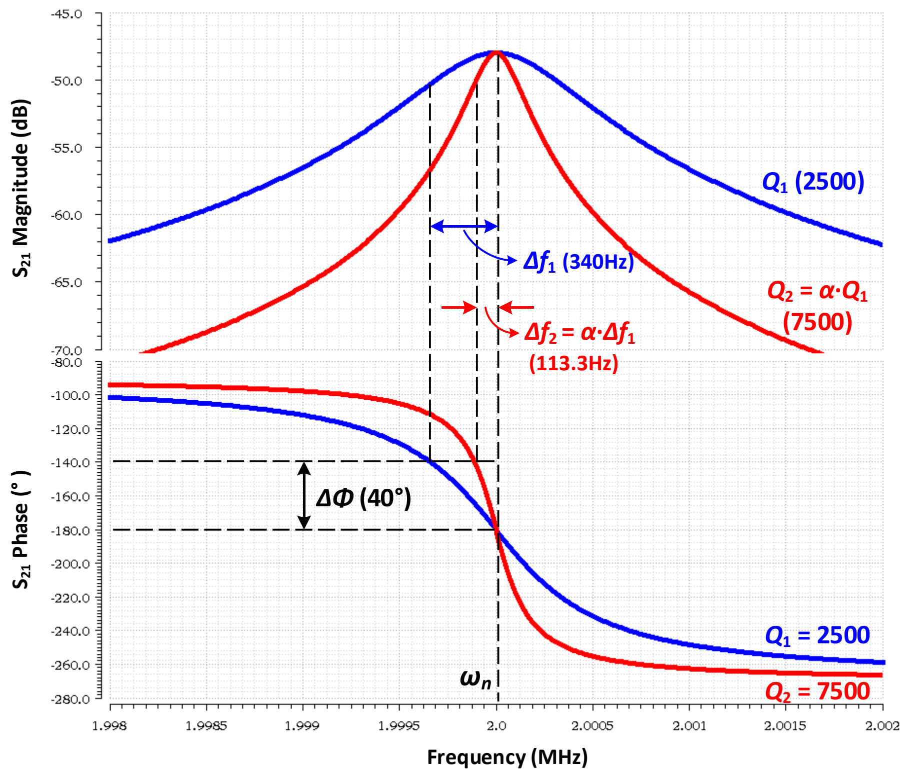


**Figure A.1** The oscillator frequency deviation due to unwanted sustaining amplifier phase shift. Two resonant peaks with quality factors of 2,500 and 7,500 are depicted here.

The phase slope at the resonance frequency can be derived as follow.

$$\left|H(j\omega)\right| = \frac{1}{k}\frac{1}{\sqrt{\left(1-\frac{\omega^2}{\omega_n^{\;2}}\right)^2 + \left(\frac{1}{Q}\frac{\omega}{\omega_n}\right)^2}} \tag{A.1}$$

$$\Phi = \angle H(j\omega) = \tan^{-1}\left(-\frac{1}{Q}\frac{\left(\frac{\omega}{\omega_n}\right)}{1-\left(\frac{\omega}{\omega_n}\right)^2}\right) \tag{A.2}$$

$$\frac{d\Phi(\omega)}{d\omega} = -\frac{\frac{\omega_n}{Q}\left(\omega^2 + \omega_n^{\;2}\right)}{\omega^4 + \omega_n^{\;4} + \omega_n^{\;2}\left(\frac{\omega^2}{Q^2} - 2\omega^2\right)} \tag{A.3}$$

$$\left.\frac{d\Phi(\omega)}{d\omega}\right|_{\omega=\omega_n} = -\frac{2Q}{\omega_n} \tag{A.4}$$

From the last equation (A.4), it can be observed that the phase slope near the resonance frequency $\omega_n$ is proportional to $Q$.

# Appendix B. PHASE SHIFT IMPACT ON THE PHASE NOISE PERFORMANCE

If the phase shift of the sustaining amplifier is not exactly 0° (or 180°), it makes the oscillation frequency ($f_{osc}$) to differ slightly from the resonance frequency ($f_{res}$) of the resonator. When $f_{osc} \neq f_{res}$, the effective filtering $Q$ is less than the resonator's $Q$. This appendix shows the comparison between the calculated and simulated PN results. To demonstrate this, a 100MHz MEMS oscillator (Figure B.1) is used as an example here. The sustaining amplifier consists of a TIA and a post-amplifier. All the circuit parameters are shown in Figure B.1.

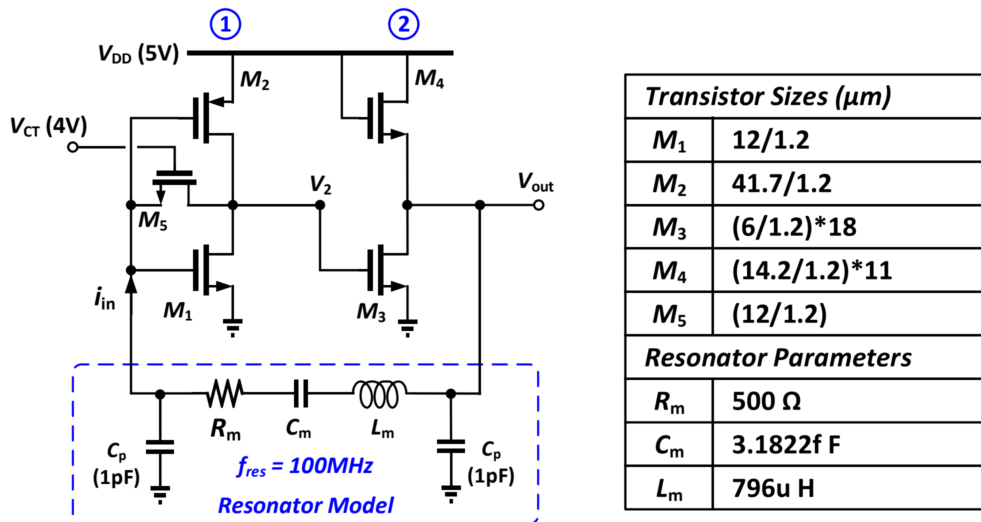


| Transistor Sizes (μm) | |
|---|---|
| $M_1$ | 12/1.2 |
| $M_2$ | 41.7/1.2 |
| $M_3$ | (6/1.2)*18 |
| $M_4$ | (14.2/1.2)*11 |
| $M_5$ | (12/1.2) |
| **Resonator Parameters** | |
| $R_m$ | 500 Ω |
| $C_m$ | 3.1822f F |
| $L_m$ | 796u H |

**Figure B.1** The example of a 100MHz MEMS oscillator.

The transient simulation setup steps are listed below.

1) Stop Time = 10μs (or longer)

2) Accuracy Defaults = conservative

3) Options → maxstep = 0.1ns

4) Give a VDD ramp 0V to 5V, 0-100ns to initiate oscillation

In Figure B.2, we insert an ideal phase shifter between the first and second stage to rectify the sustaining amplifier phase so that $f_{osc} = f_{res}$. In the phase shifter, the 500kΩ resistor and the 40pF capacitor are used for ac coupling. The replica load circuit is to make the load seen at node $V_1$ unaltered.

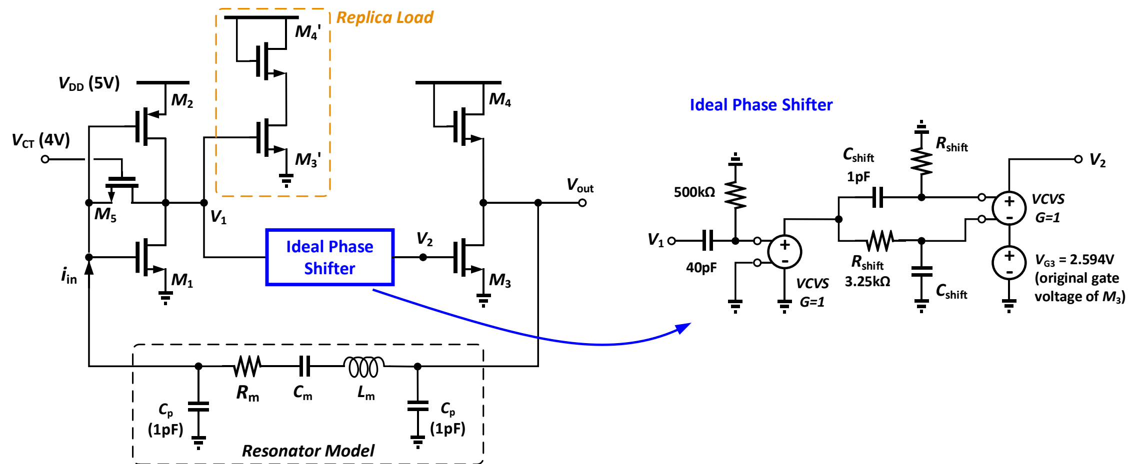


**Figure B.2** The exemplary 100MHz MEMS oscillator with an ideal phase shifter inserted.

To make sure the oscillator locks into the resonance frequency, we do a loop gain and phase simulation to check if the phase shift at the resonance frequency equals to 0° or 360° exactly, as shown in Figure B.3.

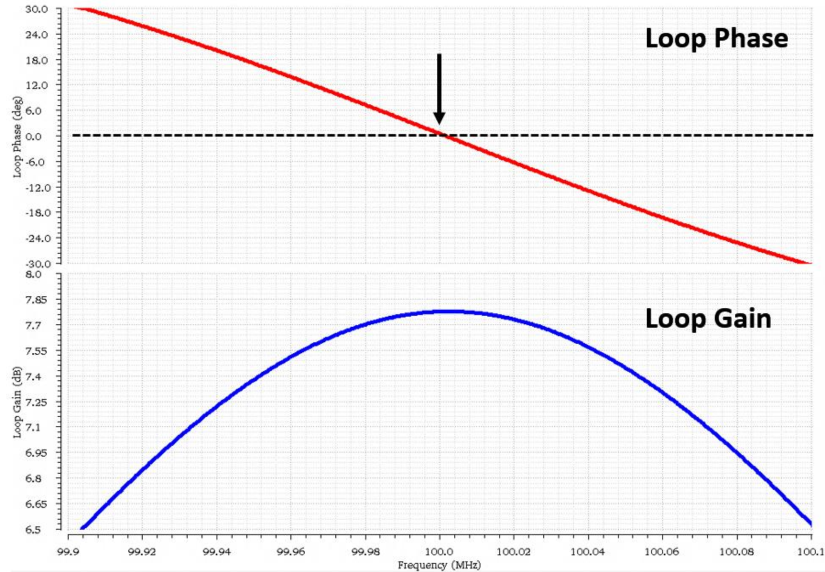


**Figure B.3** The oscillator loop gain and loop phase simulation.

The simulated oscillator noise figure (NF) and transient waveform are shown in Figure B.4. The oscillator output amplitude is about 0.83V, which translates to an output power = $0.5*(0.83^2)/957 = 360\mu W$. The exact oscillation frequency equals to 99.9969MHz according to the PSS simulation spectrum. The noise figure at 99.9969MHz equals to 15.1dB.

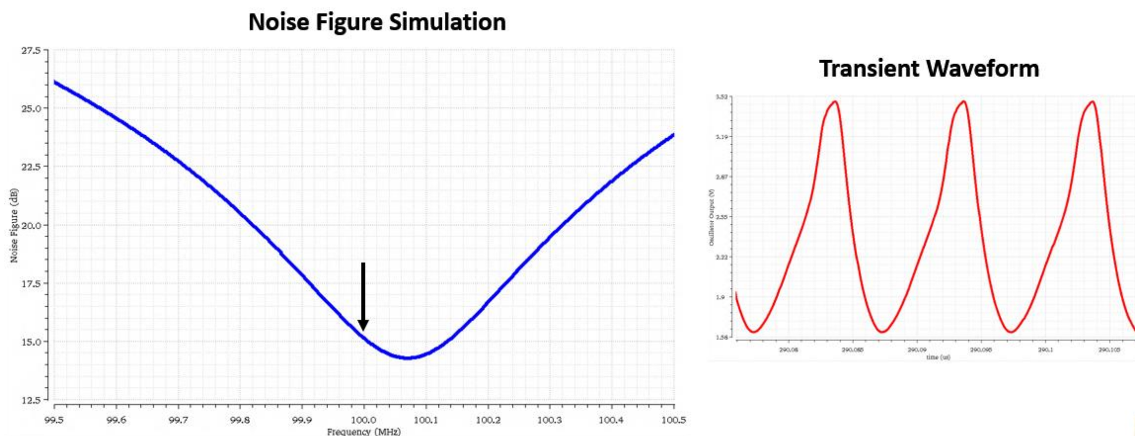


**Figure B.4** The noise figure and transient waveform of the oscillator.

Figure B.5 shows the simulated (with and without phase shifter) and calculated phase noise comparison. Without the ideal phase shifter, there is a significant difference between the simulated and calculated phase noise. With the ideal phase shifter, the difference between the simulated and calculated close-in PN is 2dBc. The difference of far-out PN estimation is about 4dBc. This result shows the importance of having $f_{osc} = f_{res}$ and demonstrates that rectifying the phase shift of the sustaining amplifier can improve the phase noise significantly.

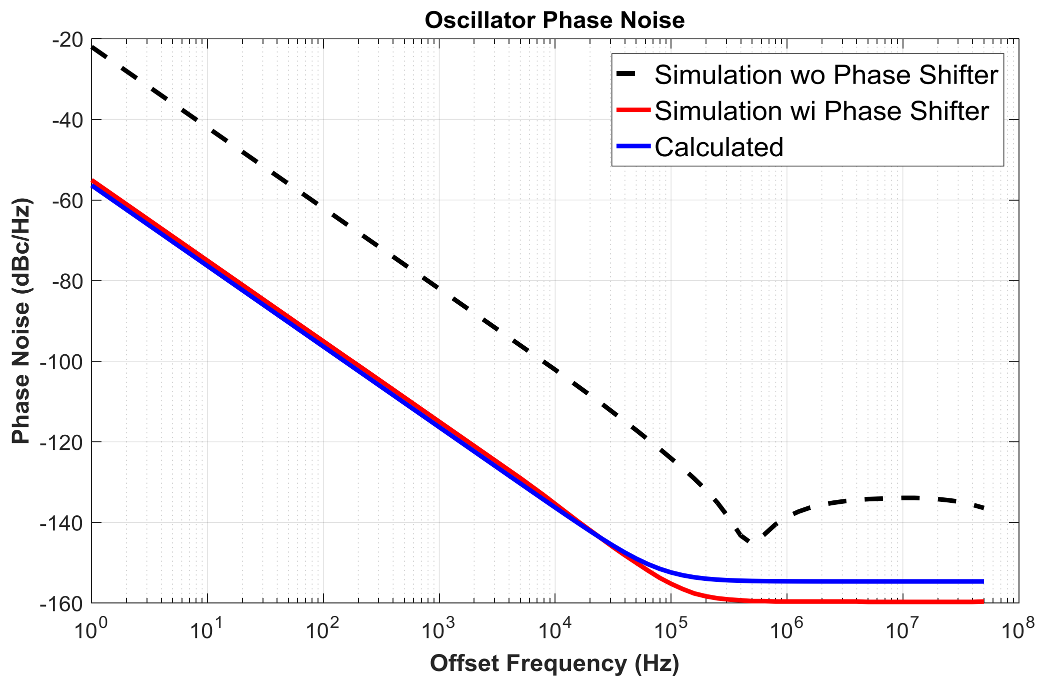


**Figure B.5** Comparison of the simulated and calculated phase noise.

# Appendix C. TIMU BOARD BONDING MAP

The TIMU die bonding map for version **A** (Cross-sectional Lame timing resonator)

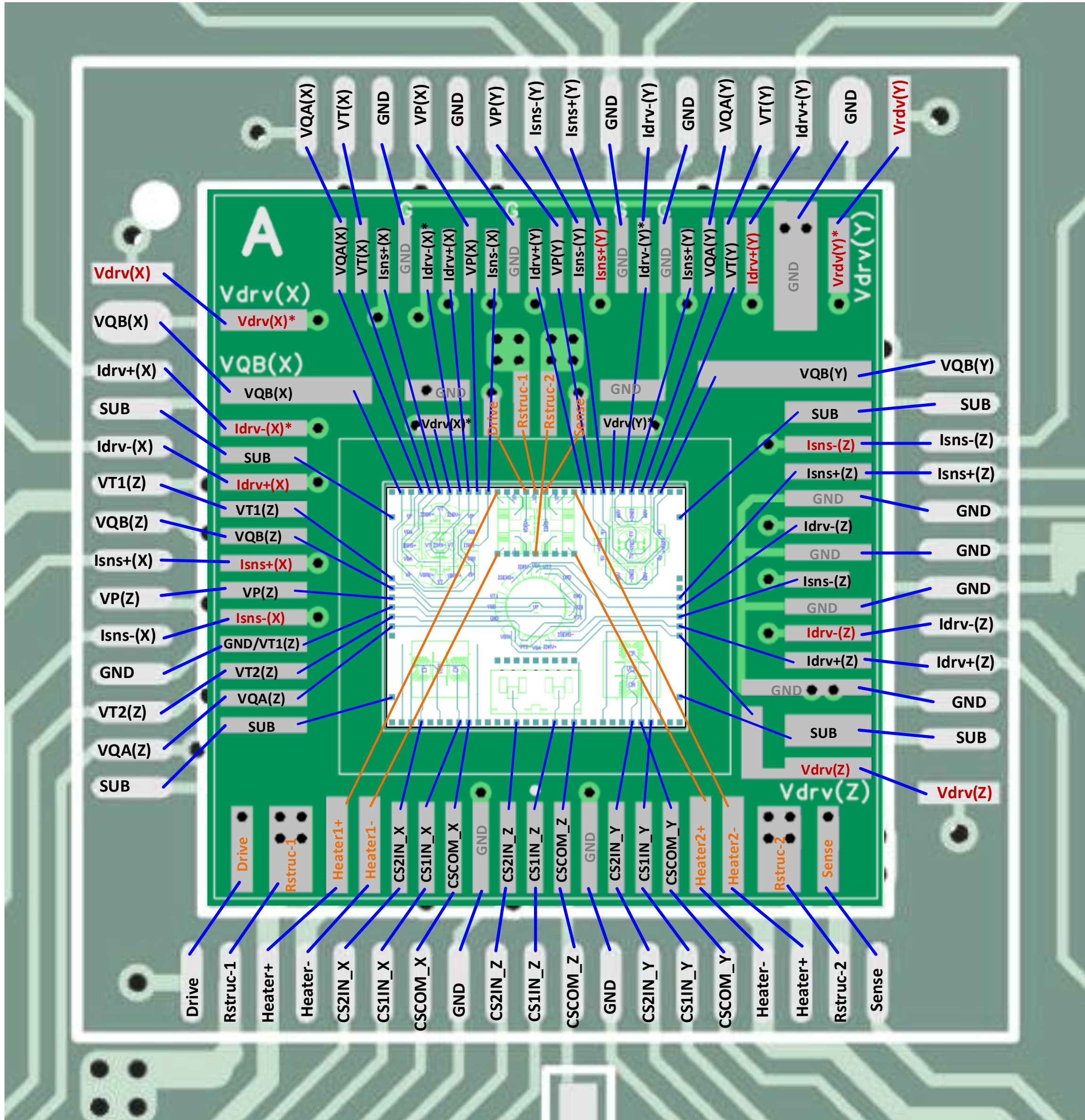

The TIMU die bonding map for version **B** (Distributed-Lame timing resonator)

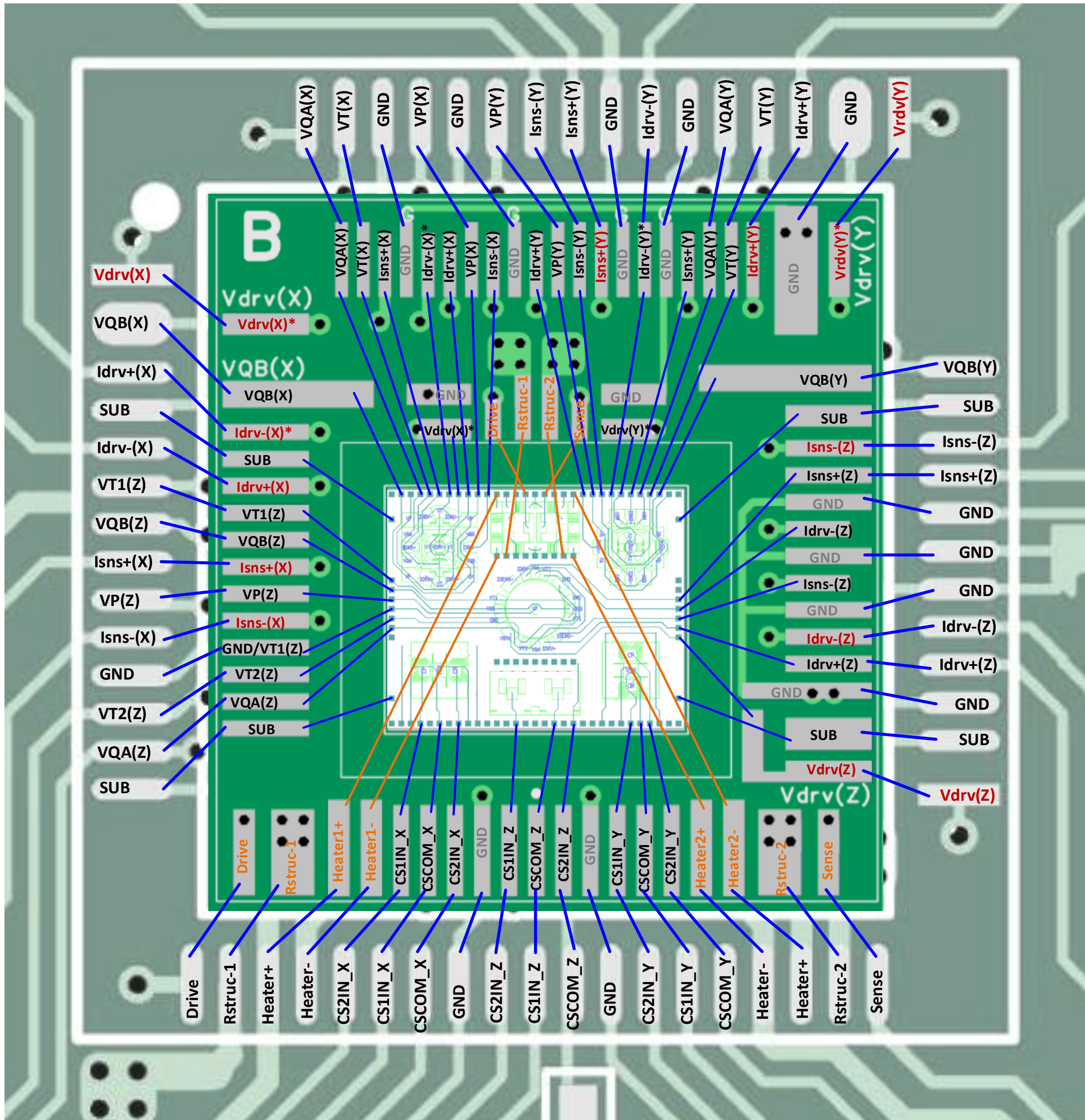

# REFERENCES


[1] R. T. Howe, "Resonant microsensors," in *Proc. 4th Int. Conf. Solid-State Sensors and Actuators (Transducers' 87)*, 1987.

[2] H. M. Lavasani, W. Pan, B. Harring, R. Abdolvand and F. Ayazi, "A 76dBOhm, 1.7 GHz, 0.18 um CMOS Tunable Transimpedance Amplfier Using Broadband Current Pre-Amplifier for High Frequency Lateral Micromechanical Oscillators," in *IEEE International Solid State Circuits Conference*, San Francisco, 2010.

[3] C. T.-C. Nguyen, "MEMS technology for timing and frequency control," in *Frequency Control Symposium and Exposition, 2005. Proceedings of the 2005 IEEE International*, Vancouver, 2005.

[4] SiTime, "Eight Reasons to Replace Crystals with MEMS Oscillators," July 2017. [Online].

[5] Abracon, "List of Top Benefits of MEMS Timing," Abracon, Oct 2018. [Online].

[6] J. R. Vig, "Quartz Crystal Resonators and Oscillators For Frequency Control and Timing Applications - A Tutorial," 2014.

[7] A. K. Samarao and F. Ayazi, "Temperature Compensation of Silicon Resonators via Degenerate Doping," *IEEE Transactions on Electron Devices,* vol. 59, no. 1, pp. 87-93, 2011.

[8] W. Pan and F. Ayazi, "Thin-film piezoelectric-on-substrate resonators with Q enhancement and TCF reduction," in *23rd IEEE MEMS*, Hong Kong, 2010.

[9] A. Hajjam, A. Rahafrooz and S. Pourkamali, "Sub-100ppb/°C temperature stability in thermally actuated high frequency silicon resonators via degenerate phosphorous doping and bias current optimization," in *Electron Devices Meeting (IEDM), 2010 IEEE International*, San Francisco, 2010.

[10] M. B. P. H. J. G. a. R. A. Shahmohammadi, "Temperature-compensated extensional-mode MEMS resonators on highly N-type doped silicon substrates," in *Proc. Solid-State Sensors, Actuat., Microsyst. Workshop*, 2012.

[11] A. K. Samarao and F. Ayazi, "Temperature compensation of silicon micromechanical resonators via degenerate doping," in *2009 IEEE International Electron Devices Meeting (IEDM)*, Baltimore, 2009.

[12] A. K. Samarao and F. Ayazi, "Intrinsic temperature compensation of highly resistive high-Q silicon microresonators via charge carrier depletion," in *2010 IEEE International Frequency Control Symposium*, Newport Beach, 2010.

[13] A. K. Samarao, G. Casinovi and F. Ayazi, "Passive TCF compensation in high Q silicon micromechanical resonators," in *Micro Electro Mechanical Systems (MEMS), 2010 IEEE 23rd International Conference on*, Hong Kong, 2010.

[14] R. Tabrizian, G. Casinovi and F. Ayazi, "Temperature-Stable Silicon Oxide (SilOx) Micromechanical Resonators," *IEEE Transactions on Electron Devices,* vol. 60, no. 8, pp. 2656-2663, 2013.

[15] R. Melamud, S. A. Chandorkar, B. Kim, H. K. Lee, J. C. Salvia, G. Bahl, M. A. Hopcroft and T. W. Kenny, "Temperature-Insensitive Composite Micromechanical Resonators," *Journal of Microelectromechanical Systems,* vol. 18, no. 6, pp. 1409-1419, 16 Oct 2009.

[16] R. Abdolvand, G. K. Ho, J. Butler and F. Ayazi, "ZnO-on-nanocrystalline diamond lateral bulk acoustic resonators," in *Micro Electro Mechanical Systems, 2007. MEMS. IEEE 20th International Conference on*, Hyogo, 2007.

[17] F. Ayazi and K. Najafi, "High Aspect-Ratio Combined Poly and Single-Crystal Silicon (HARPSS) MEMS Technology," *Journal of Microelectromechanical Systems,* vol. 9, no. 3, pp. 288-294, Sept. 2000.

[18] B. Razavi, "A 622Mb/s 4.5pA/sqrt-Hz CMOS Transimpedance Amplifier," in *IEEE International Solid-State Circuit Conference*, San Francisco, 2000.

[19] P.-C. Huang, "A 3.3-V CMOS wideband exponential control variable-gain-amplifier," in *ISCAS*, 1998.

[20] C.-H. Wu, C.-S. Liu and S.-I. Liu, "A 2 GHz CMOS variable-gain amplifier with 50 dB linear-in-magnitude controlled gain range for 10GBase-LX4 Ethernet," in *Internation Solid-State Circuit Conference*, San Francisco, CA, USA, 2004.

[21] C.-F. Liao and S.-I. Liu, "A 10Gb/s CMOS AGC Amplifier with 35dB Dynamic Range for 10Gb Ethernet," in *International Solid-State Circuit Conference*, San Francisco, CA, USA, 2006.

[22] K. Sundaresan, G. K. Ho, S. Pourkamali and F. Ayazi, "A Low Phase Noise 100MHz Silicon BAW Reference Oscillator," in *IEEE Custom Integrated Circuits Conference 2006*, San Jose, 2006.

[23] M. M. M. O. M. H. R. M. S. C. H. L. G. B. B. M. T. K. J. Salvia, "Exploring the limits and practicality of Q-based temperature compensation for silicon resonators," in *2008 IEEE International Electron Devices Meeting*, San Francisco, 2008.

[24] J. C. Salvia, R. Melamud, S. A. Chandorkar, S. F. Lord and T. W. Kenny, "Real-Time Temperature Compensation of MEMS Oscillators Using an Integrated Micro-Oven and a Phase-Locked Loop," *Journal of Microelectromechanical Systems,* vol. 19, no. 1, pp. 192 - 201, Feb. 2010.

[25] C.-C. Chen, H.-T. Yu, G.-H. Li and S.-S. Li, "Enhancement of temperature stability via constant-structural-resistance control for MEMS resonators," in *Micro Electro Mechanical Systems (MEMS), 2013 IEEE 26th International Conference on*, Taipei, 2013.

[26] Y. Chen, E. J. Ng, Y. Yang, C. H. Ahn, I. Flader and T. W. Kenny, "In-situ ovenization of Lamé-mode silicon resonators for temperature compensation," in *2015 28th IEEE International Conference on Micro Electro Mechanical Systems (MEMS)*, Estoril, 2015.

[27] R. Tabrizian, A. Daruwalla and F. Ayazi, "High-Q Energy Trapping of Temperature-Stable Shear Waves with Lame Cross-Sectional Polarization in a Single Crystal Silicon Waveguide," *Applied Physics Letter,* vol. 108, no. 11, 2016.

[28] S. Pourkamali, G. K. Ho and F. Ayazi, "Low-Impedance VHF and UHF Capacitive Silicon Bulk Acoustic Wave Resonators-Part I: Concept and Fabrication," *IEEE Transactions on Electron Devices,* vol. 54, no. 8, pp. 2017 - 2023, 2007.

[29] J. Lee and A. A. Seshia, "Parasitic Feedthrough Cancellation Techniques for Enhanced Electrical Characterization of Electrostatic Microresonators," *Sensors and Actuators A: Physical,* vol. 156, no. 1, pp. 36-42, 2009.

[30] C. Xu, J. Segovia-Fernandez and G. Piazza, "Sub-milliwatt integrated oven for temperature stable laterally vibrating piezoelectric MEMS resonators," in *2015 18th International Conference on Solid-State Sensors, Actuators and Microsystems (TRANSDUCERS)*, Anchorage, USA, 2015.

[31] N. Yazdi, F. Ayazi and K. Najafi, "Micromachined Inertial Sensors," *Proceedings of the IEEE,* vol. 86, no. 8, pp. 1640 - 1659, 1998.

[32] M. Weinberg and A. Kourepenis, "Error Sources in In-Plane Silicon Tuning Fork MEMS Gyroscopes," *Journal of Microelectromechanical Systems,* vol. 15, pp. 479-491, 2006.

[33] IEEE, "IEEE Standard Specification Format Guide and Test Procedure for Single-Axis Interferometric Fiber Optic Gyros," IEEE, 1998.

[34] F. Ayazi, High Aspect-ratio High Performance Polysilicon Vibrating Ring Gyroscope, University of Michigan: Ph.D. dissertation, 2000.

[35] M. Zaman, A. Sharma, Z. Hao and F. Ayazi, "A Mode-matched Silicon Yaw Tuning-Fork Gyroscope with Subdegree-per-hour Allan Deviation Bias Instability," *Journal of Microelectromechanical Systems,* vol. 17, pp. 1526-1536, 2008.

[36] F. Ayazi, "Multi-DOF Inertial MEMS: From Gaming to Dead Reckoning," in *16th International Solid-State Sensors, Actuators and Microsystems Conference (TRANSDUCERS)*, 2011.

[37] S. Sung, W. T. Sung, C. Kim, S. Yun and Y. J. Lee, "On the Mode-Matched Control of MEMS Vibratory Gyroscope via Phase-Domain Analysis and Design," *IEEE/ASME Transactions on Mechatronics,* vol. 14, pp. 446-455, 2009.

[38] M. Saukoski, L. Aaltonen and K. Halonen, "Zero-Rate Output and Quadrature Compensation in Vibratory MEMS Gyroscopes," *IEEE Sensors Journal,* vol. 7, pp. 1639-1652, 2007.

[39] A. Norouzpour-Shirazi, "Advanced Interface Systems for Readout, Control, and Self-Calibration of MEMS Resonant Gyroscopes," Georgia Institute of Technology, Atlanta, 2016.

[40] M. Zaman, "Degree-per-hour Mode-Matched Micromachined Silicon Vibratory Gyroscopes," Georgia Institute of Technology, 2008.

[41] A. Sharma, M. Zaman and F. Ayazi, "A Sub-0.2 °/hr Bias Drift Micromechanical Gyroscope with Automatic CMOS Mode-Matching," *EEE Journal of Solid-State Circuits,* vol. 33, pp. 1593-1608, 2009.

[42] A. N. Shirazi, M. Zaman and F. Ayazi, "A Digital Phase Demodulation Technique for Resonant MEMS Gyroscopes," *IEEE Sensors Journal,* vol. 14, no. 9, pp. 3260-3266, 2014.

[43] D. Allan, "Statistics of Atomic Frequency Standards," *Proceedings of the IEEE,* vol. 54, no. 2, pp. 221-230, 1966.

[44] IEEE, "IEEE Standard for Inertial Sensor Terminology," IEEE, 2001.

[45] L. Ng, "On the Application of Allan Variance Method for Ring Laser Gyroscope Performance Characterization," 1993.

[46] B. Gallacher, J. Hedley, J. Burdess, A. Harris, A. Rickard and D. King, "Electrostatic Correction of Structural Imperfections Present in a Microring Gyroscope," *Journal of Microelectromechanical Systems,* vol. 14, pp. 221-234, April 2005.

[47] H. Wen, A. Daruwalla, Y. Jeong, P. Gupta, J. Choi, C.-s. Liu and F. Ayazi, "A High-Performance Single-Chip Timing and Inertial Measurement Unit With Robust Mode-Matched Gyroscopes," in *2018 IEEE Micro Electro Mechanical Systems (MEMS)*, 2018.

[48] H. Wen, "Toward Inertial-Navigation-on-Chip: The Physics and Performance Scaling of Multi-Degree-of-Freedom Resonant MEMS Gyroscopes," *Ph.D. dissertation,* 2018.

[49] Y. Jeong, "Integrated Three-Axis Accelerometers with Nanometer Scale Capacitive Gaps and Signal Conditioning Interface IC," *Ph.D. dissertation,* 2017.

[50] R. Tabrizian, A. Daruwalla and F. Ayazi, "High-Q energy trapping of temperature-stable shear waves with Lamé cross-sectional polarization in a single crystal silicon waveguide," *Applied Physics Letters,* vol. 108, p. 113503, 2016.

[51] C.-S. Liu, R. Tabrizian and F. Ayazi, "A ±0.3 ppm Oven-Controlled MEMS Oscillator Using Structural Resistance-Based Temperature Sensing," *IEEE Transactions on Ultrasonics, Ferroelectrics, and Frequency Control,* vol. 65, no. 8, pp. 1492 - 1499, 4 June 2018.

[52] H. Wen, A. Daruwalla, C.-S. Liu and F. Ayazi, "A High-Frequency Resonant Framed-Annulus Pitch or Roll Gyroscope for Robust High-Performance Single-Chip Inertial Measurement Units," *Journal of Microelectromechanical Systems,* vol. 27, no. 6, pp. 995 - 1008, Dec 2018.

[53] A. G. Sabnis and J. T. Clemens, "Characterization of the electron mobility in the inverter <100> Si surface," in *IEEE International Electron Devices Meeting*, 1979.

[54] S. M. Sze, Physics of semiconductor devices, 2nd ed., New York: John Wiley and Sons, 1981.

[55] S. Donnay, X. Rottenberg, J. Borremans, H. Tilmans, G. v. d. Plas and M. Pertijs, "Oven Controlled MEMS Oscillator Device". USA Patent US 2012/0305542 A1, 6th Dec 2012.

[56] A. Norouzpour-Shirazi, M. Hodjat-Shamami, R. Tabrizian and F. Ayazi, "Dynamic tuning of MEMS resonators via electromechanical feedback," *IEEE Transactions on Ultrasonics, Ferroelectrics, and Frequency Control,* vol. 62, no. 1, pp. 129 - 137, 2015.

[57] A. Norouzpour-Shirazi, M. F. Zaman and F. Ayazi, "A Digital Phase Demodulation Technique for Resonant MEMS Gyroscopes," *IEEE Sensors Journal,* vol. 14, no. 9, pp. 3260 - 3266, May 2014.

[58] K. Sundaresan, G. K. Ho, S. Pourkamali and F. Ayazi, "Electronically Temperature Compensated Silicon Bulk Acoustic Resonator Reference Oscillators," *IEEE Journal of Solid-State Circuits,* vol. 42, no. 6, pp. 1425 - 1434, June 2007.

[59] H. M. Lavasani, W. Pan, B. P. Harrington, R. Abdolvand and F. Ayazi, "Electronic Temperature Compensation of Lateral Bulk Acoustic Resonator Reference Oscillators Using Enhanced Series Tuning Technique," *IEEE Journal of Solid-State Circuits,* vol. 47, no. 6, pp. 1381 - 1393, May 2012.

[60] R. Tabrizian, M. Pardo and F. Ayazi, "A 27 MHz temperature compensated MEMS oscillator with sub-ppm instability," in *Micro Electro Mechanical Systems (MEMS), 2012 IEEE 25th International Conference on*, Paris, 2012.

[61] M.-D. Tsai, C.-W. Yeh, Y.-H. Cho, L.-W. Ke, P.-W. Chen and G.-K. Dehng, "A temperature-compensated low-noise digitally-controlled crystal oscillator for multi-standard applications," in *2008 IEEE Radio Frequency Integrated Circuits Symposium*, Atlanta, 2008.

[62] S. Rai, Y. Su, W. Pang, R. Ruby and B. Otis, "A digitally compensated 1.5 GHz CMOS/FBAR frequency reference," *IEEE Transactions on Ultrasonics, Ferroelectrics, and Frequency Control,* vol. 57, no. 3, pp. 552 - 561, March 2010.

[63] M. H. Perrott, J. C. Salvia, F. S. Lee, A. Partridge, S. Mukherjee, C. Arft, J. Kim, N. Arumugam, P. Gupta, S. Tabatabaei, S. Pamarti, H. Lee and F. Assaderaghi, "A temperature-to-digital converter for a MEMS-based programmable oscillator with <+-0.5

frequency stability and 1-ps integrated jitter," *IEEE Journal of Solid-State Circuits,* vol. 48, no. 1, pp. 276 - 291, Oct. 2012.

[64] Z. Wu, A. Peczalski and M. Rais-Zadeh, "Low-power ovenization of fused silica resonators for temperature-stable oscillators," in *2014 IEEE International Frequency Control Symposium (FCS)*, Taipei, 2014.

[65] Y. Chen, E. J. Ng, D. D. Shin, C. H. Ahn, Y. Yang, I. B. Flader, V. A. Hong and T. W. Kenny, "Ovenized dual-mode clock (ODMC) based on highly doped single crystal silicon resonators," in *2016 IEEE 29th International Conference on Micro Electro Mechanical Systems (MEMS)*, Shanghai, 2016.

[66] A. Tazzoli, G. Piazza and M. Rinaldi, "Ultra-high-frequency temperature-compensated oscillators based on ovenized AlN contour-mode MEMS resonators," in *2012 IEEE International Frequency Control Symposium Proceedings*, Baltimore, 2012.

[67] M.-H. Li, C.-Y. Chen, C.-S. Li, C.-H. Chin and S.-S. Li, "A Monolithic CMOS-MEMS Oscillator Based on an Ultra-Low-Power Ovenized Micromechanical Resonator," *Journal of Microelectromechanical Systems,* vol. 24, no. 2, pp. 360 - 372, March 2015.

[68] Z. Wu and M. Rais-Zadeh, "A temperature-stable mems oscillator on an ovenized micro-platform using a PLL-based heater control system," in *2015 28th IEEE International Conference on Micro Electro Mechanical Systems (MEMS)*, Estoril, 2015.

[69] T. V. Roszhart, H. Jerman, J. Drake and C. d. Cotiis, "An inertial-grade, micromachined vibrating beam accelerometer," in *Solid-State Sensors and Actuators, 1995 and Eurosensors IX.. Transducers' 95. The 8th International Conference on*, 1995.

[70] E. W. Bums, R. D. Homing, W. R. Herb, J. D. Zook and H. Guckel., "Resonant microbeam accelerometers," in *Solid-State Sensors and Actuators, 1995 and Eurosensors IX.. Transducers' 95. The 8th International Conference on*, 1995.

[71] A. A. Seshia, M. Palaniapan, T. A. Roessig, R. T. Howe, R. W. Gooch, T. R. Schimert and S. Montague, "A vacuum packaged surface micromachined resonant accelerometer," *Journal of Microelectromechanical Systems,* vol. 11, no. 6, pp. 784 - 793, Dec 2002.

[72] X. Zou, P. Thiruvenkatanathan and A. A. Seshia, "A Seismic-Grade Resonant MEMS Accelerometer," *Journal of Microelectromechanical Systems,* vol. 23, no. 4, pp. 768-770, July 2014.

[73] X. Zou and A. A. Seshia, "A high-resolution resonant MEMS accelerometer," in *2015 Transducers - 2015 18th International Conference on Solid-State Sensors, Actuators and Microsystems (TRANSDUCERS)*, Anchorage, 2015.

[74] X. Wang, J. Zhao, Y. Zhao, G. M. Xia, A. P. Qiu, Y. Su and Y. P. Xu, "A 1.2µg/√Hz-resolution 0.4µg-bias-instability MEMS silicon oscillating accelerometer with CMOS readout circuit," in *2015 IEEE International Solid-State Circuits Conference - (ISSCC) Digest of Technical Papers*, San Francisco, 2015.

[75] L. He, Y. P. Xu and M. Palaniapan, "A CMOS Readout Circuit for SOI Resonant Accelerometer With 4-µg Bias Stability and 20-µg/√Hz Resolution," *IEEE Journal of Solid-State Circuits,* vol. 43, no. 6, pp. 1480-1490, May 2008.

[76] S. A. Zotov, B. R. Simon, A. A. Trusov and A. M. Shkel, "High Quality Factor Resonant MEMS Accelerometer With Continuous Thermal Compensation," *IEEE Sensors Journal,* vol. 15, no. 9, pp. 5045-5052, July 2015.

[77] B.-L. Lee, C.-H. Oh, S. Lee, Y.-S. Oh and K.-J. Chun, "A vacuum packaged differential resonant accelerometer using gap sensitive electrostatic stiffness changing effect," in *Micro Electro Mechanical Systems, 2000. MEMS 2000. The Thirteenth Annual International Conference on*, Miyazaki, 2000.

[78] S. Sung, J. G. Lee and T. Kang, "Development and test of MEMS accelerometer with self-sustatined oscillation loop," *Sensors and Actuators A: Physical,* vol. 109, no. 1-2, pp. 1-8, Dec 2003.

[79] C. Comi and A. G. S. Z. Alberto Corigliano, "A resonant micro accelerometer based on electrostatic stiffness variation," *Meccanica,* vol. 48, no. 8, pp. 1893-1900, June 2013.

[80] H. M. Zhang, W. Z. Yuan, B. Y. Li, Y. C. Hao, M. Kraft and H. L. Chang, "A novel resonant accelerometer based on mode localization of weakly coupled resonators," in *2015 Transducers - 2015 18th International Conference on Solid-State Sensors, Actuators and Microsystems (TRANSDUCERS)*, Anchorage, 2015.

[81] H. K. Lee, J. Salvia, G. Bahl, R. Melamud, S. Yoneoka, Y. Q. Qu, S. Chandorkar, M. A. Hopcroft, B. Kim and T. W. Kenny, "Influence of the temperature dependent A-f effect on the design and performance of oscillators," in *Micro Electro Mechanical Systems (MEMS), 2010 IEEE 23rd International Conference on*, Hong Kong, 2010.

[82] F. Ayazi, "Bulk acoustic wave accelerometers". U.S. Patent 20140102197 A1, 17 April 2014.

[83] C. T.-C. Nguyen and R. T. Howe, "Microresonator frequency control and stabilization using an integrated micro oven," in *The 7th International Conference on Solid-State Sensors and Actuators (Transducers'93)*, Yokohama, Japan, 1993.

[84] H. C. Kim, S. Seok, I. Kim, S.-D. Choi and K. Chun, "Inertial-grade out-of-plane and in-plane differential resonant silicon accelerometers (DRXLs)," in *The 13th International Conference on Solid-State Sensors, Actuators and Microsystems, 2005. Digest of Technical Papers. TRANSDUCERS '05*, Seoul, South Korea, 2005.

[85] C. Xu, J. Segovia-Fernandez and G. Piazza, "Sub-milliwatt integrated oven for temperature stable laterally vibrating piezoelectric MEMS resonators," in *2015 18th International Conference on Solid-State Sensors, Actuators and Microsystems (TRANSDUCERS)*, Anchorage, USA, 2015.